DISSERTATION

THE IMPACTS OF MINERAL DUST ON ORGANIZED MESOSCALE DEEP CONVECTION

Submitted by

Robert Brian Seigel

Department of Atmospheric Science

In partial fulfillment of the requirements

For the Degree of Doctor of Philosophy

Colorado State University

Fort Collins, Colorado

Fall 2012

Doctoral Committee:

Advisor: Susan C. van den Heever

Sonia M. Kreidenweis
Wayne H. Schubert
Jeffrey D. Niemann

ABSTRACT

THE IMPACTS OF MINERAL DUST ON ORGANIZED MESOSCALE DEEP CONVECTION

The world leader in heavy-precipitation production is deep moist convection (DMC) that is organized on the mesoscale. While various environmental factors such as instability and vertical wind shear are crucial in the development and sustenance of organized DMC, aerosols have recently received much attention because of their impact on cloud processes that lead to changes in DMC organization. The presence of aerosols directly modifies the radiative budget through absorption and scattering of both shortwave and longwave radiation, an impact referred to as the aerosol direct effect (ADE). This can alter environmental stability that can lead to a modulation of organization. Additionally, by acting as a source of nucleation for cloud droplets and ice crystals, aerosols alter precipitation processes and the microstructure of clouds, thereby further impacting energy budgets that lead to what are referred to as aerosol indirect effects (AIEs). As mineral dust is arguably the most abundant aerosol species in the world and has been found to act as cloud condensation nuclei (CCN) and ice nuclei (IN), it is important to better understand the forcing of dust on the global energy budget via microphysical process. Therefore, the overarching goal of this research is to investigate how mineral dust can impact organized deep moist convection using numerical modeling. This is achieved through four modeling studies that each address a different aspect of organized mesoscale DMC.

The first study uses the Regional Atmospheric Modeling System (RAMS) to simulate a supercell storm in order to examine the pathways in which mineral dust is entrained into DMC. This is achieved by simulating a supercell within three commonly observed dust regimes. First, a

supercell is simulated within an already dusty environment (EXP-BACKGROUND) to investigate ingestion purely from a background dust source. Second, the supercell is simulated within a clean background environment but lofts its own dust via the use of a fully interactive dust model (EXP-STORM), to investigate the regime in which the only source of dust in the atmosphere is due to the storm itself. Finally, the supercell is simulated with a low-level convergence boundary introduced ahead of the supercell to investigate dust lofting by outflow boundary interactions (EXP-BOUNDARY). Results indicate that the supercell in EXP-BACKGROUND ingests large dust concentrations ahead of the rear-flank downdraft (RFD) cold pool. Conversely, dust lofted by the cold pool in EXP-STORM is ingested by the supercell in relatively small amounts via a narrow corridor generated by turbulent mixing between the RFD cold pool and ambient air. The addition of a convergence boundary in EXP-BOUNDARY is found to act as an additional source of dust for the supercell and represents the case between EXP-BACKGROUND and EXP-STORM. Results demonstrate the importance of using an appropriate dust parameterization when modeling DMC, especially within more arid regions.

The second study utilizes an idealized simulation of a nocturnal squall line to assess and isolate the individual responses in a squall line that arise (1) from radiation, (2) from dust altering the microphysics, as well as (3) from the synergistic effects between (1) and (2). To accomplish these tasks, we again use RAMS set up as a cloud-resolving model (CRM). The CRM contains aerosol and microphysical schemes that allow radiatively active mineral dust particles to nucleate as cloud drops and ice crystals, replenish upon evaporation and sublimation, be tracked throughout hydrometeor transition, and be scavenged by precipitation and dry sedimentation. Factor separation is used on four simulations of the squall line in order to isolate the individual roles of radiation (RADIATION), microphysically active dust (DUST MICRO),

and the nonlinear interactions between these two factors (SYNERGY). Results indicate that RADIATION acts to increase precipitation, intensify the cold pool, and enhance the mesoscale organization of the squall line due to radiation-induced changes in the microphysics that appear to initiate from cloud top cooling. Conversely, DUST MICRO decreases precipitation, weakens the cold pool, and weakens the mesoscale organization of the squall line due to an enhancement of the warm rain process. SYNERGY shows little impact on the squall line, except near the freezing level, where an increase in mesoscale organization takes place.

A third study is conducted in order to isolate a microphysical hydrometeor recirculation mechanism that was evident in the squall line simulations described above. This third study examines four numerically simulated idealized squall lines also using RAMS, and includes a control simulation that uses full two-moment microphysics and three sensitivity experiments that vary the mean diameter of the hail hydrometeor size distribution within a single-moment framework. Results suggest that a circulation centered at the freezing level supports mid-level convective updraft invigoration through increased latent heating. The circulation begins with hail hydrometeors that initiate within the convective updraft above the freezing level, and are then ejected upshear due to the front-to-rear flow of the squall line. As the hail falls below the freezing level, the rear-inflow jet (RIJ) advects the hail hydrometeors downshear and into the upshear flank of the mid-level convective updraft. Because the advection occurs below the freezing level, some of the hail melts and sheds rain drops. The addition of this excess hail and rain into the updraft enhances latent heating due both to an enhancement in riming and vapor deposition onto the increased total surface area of hail and rain. The increase in latent heating enhances buoyancy within the updraft, which leads to an increase in precipitation and cold pool intensity that promotes a positive feedback on squall line strength. The upshear-tilted simulated

squall lines in this study indicate that as hail size is decreased, squall lines are invigorated through the recirculation mechanism.

Finally, as mineral dust has been shown to impact atmospheric stability through ADEs, and cold pools have been found to be sensitive to low-level stability, a fourth study was conducted to investigate the impacts of a stably stratified layer embedded within a neutrally stratified environment on the behavior of density currents. This study extends the environmental regimes examined by Liu and Moncrieff (2000) (LM2000). Such environments frequently support severe weather events.

To accomplish this goal, nonhydrostatic numerical model experiments are performed in which the strength and height of the embedded stably stratified layer within a neutrally stratified environment are varied. The 1 km deep stable layer base is varied between 1, 2, and 3 km above ground level (AGL). Additionally, the strength of the stable layer is systematically varied between Brunt Väisälä frequencies of 0.006 s^{-1}, 0.012 s^{-1}, and 0.018 s^{-1}, following the methodology of LM2000. The model, which I developed within a numerical modeling class at Colorado State University (ATS730), and grid setup are also similar to that of LM2000, utilizing the Arakawa-C grid, leapfrog advection, a Robert-Asselin filter, and grid spacing of 100 m and 50 m in the horizontal and vertical directions, respectively. Results show that the height of the density current decreases and the propagation speed increases with stronger and lower stable layers, providing that the stable layer is sufficiently thin so as to not act as a gravity wave ducting layer. As the strength of the stable layer increases and the height of this layer decreases, the horizontal pressure gradient driving the density current increases, resulting in faster propagation speeds. Such results have implications for cold pool propagation into more stable environments, and hence as a nocturnal squall line approaches a low-level dust layer that is

radiatively cooling, creating stability, its cold pool may slow down, thereby altering its organization.

The collective results of these studies show that mineral dust can play a large role in various aspects of organized mesoscale deep moist convection.

ACKNOWLEDGEMENTS

I would like to express my sincerest gratitude and appreciation to Dr. Susan van den Heever, my advisor, for giving me a wonderful opportunity to work on this project. Her extreme patience and care helped me to become a better writer and interpreter of good science. Perhaps more importantly, during the past three years Dr. van den Heever went above and beyond to ensure that I learned more than just science alone. Dr. van den Heever instilled in me many invaluable ethical, social, and advisory values from our many one-on-one conversations, as well as by simply being a good role model. I will strive to provide the same assiduousness and values to my students and colleagues as I continue to develop my career. I could not have imagined having a better advisor – thank you.

I would also like to acknowledge and thank my committee members – Dr. Sonia Kreidenweis, Dr. Wayne Schubert, and Dr. Jeffrey Niemann – for their informative and thoughtful comments as well as their great time investment, all of which contributed to the success of this dissertation.

Many thanks to the students and scientists in the van den Heever Group. Our numerous discussions were instrumental in the completion of this dissertation. I thank Steve Saleeby, Steve Herbener, Rachel Storer, Leah Grant, Adele Igel, Clayton McGee, Matt Igel, Amanda Sheffield, Josh King, and Michal Clavner for not only their insight into my research, but also for providing additional avenues of stress relief through humorous conversations, weather discussions, and support.

Finally, I would like to thank the most important person in my life, my wife – I could not have accomplished this without you. Thank you for being so patient and supportive while I

completed my degrees at CSU. You are truly inspirational and knowing that you will be by my side throughout my career is extremely comforting.

This work was jointly funded by the National Aeronautics and Space Administration under grant NNX07AT11G, the National Science Foundation under grant ATM-0820556, and the Department of Defense Center for Geosciences/Atmospheric Research at Colorado State University under Cooperative Agreement W911NF-06-2-0015 with the Army Research Laboratory.

TABLE OF CONTENTS

CHAPTER I: INTRODUCTION TO THE DISSERTATION

Mineral dust is arguably the most abundant aerosol species in the world (IPCC 2007). Its lifecycle begins with strong surface winds that mobilize large soil particles, causing a tumbling (known as saltation) that can bombard other smaller particles and lead to a surface emission of dust (known as suspension) (Fecan et al. 1999). Around the globe, the surface emission of dust is greatest near the desert regions of the world, with North Africa contributing 50-70% and Asia contributing 10-20% to the global dust load (Tegen and Schepanski 2009). Once mobilized, mineral dust can be lofted high into the atmosphere where it can then be transported vast distances (Prospero 1996, 1999; Perry et al. 1997; Sassen et al., 2003). While the process by which mineral dust is emitted from the surface is fairly well understood from laboratory experiments (e.g. Saleh and Fryrear 1995; Chen et al. 1996; Fecan et al. 1999), mineral dust interactions with atmospheric processes, such as clouds, precipitation, and radiative transfer, are more complex and not as well understood.

There are two primary pathways through which mineral dust impacts the atmosphere. First, through absorption and scattering of both solar and infrared radiation, mineral dust can impact the thermodynamics of the atmosphere and the energy balance of the Earth. This is often referred to as the aerosol direct effect (ADE; Quijiano et al., 2000; Hansell et al., 2010). Second, the suspended particles have been found to serve as nuclei for both cloud droplets (Twohy et al. 2009) and ice crystals (DeMott et al. 2003), which can help to change the microstructure and processes of all cloud types. This is often referred to as the aerosol indirect effect (AIE) because it indirectly impacts the energy budget of the Earth through changes to cloud microphysical properties (Twomey, 1974; Albrecht, 1989). While the AIE has been studied extensively (e.g.

Borys et al. 1998; Ferek et al. 2000; Kaufman and Nakajima 1993; Rosenfeld 2000; Heymsfield and McFarquhar 2001; Khain et al. 2005; van den Heever et al. 2006, 2011; van den Heever and Cotton 2007; Lee et al. 2008; Storer et al. 2010; Solomos et al. 2011; Igel et al. 2012; Morrison 2012; Storer and van den Heever 2012), it remains as one of the largest uncertainties in climate forcing (Forster et al. 2007) due to its dependence on aerosol characteristics and composition (Twomey 1974, Albrecht 1989, Petters and Kreidenweis 2007, DeMott et al. 2010) and aerosol's highly complex interactions with clouds and precipitation processes (Tao et al. 2012). This is the primary motivation for the research presented in this document.

As precipitation is a major uncertainty in climate change (IPCC 2007), it is important to understand how deep moist convection (DMC) is impacted by mineral dust, especially as mineral dust is forecast to increase in the future (Prospero 2003). DMC can be classified into two separate categories: unorganized or organized. The organization of DMC can occur on a range of scales. On the synoptic scale (e.g. length scales greater than 1,000 km), DMC is organized by synoptic-scale circulations that force large-scale convergence, leading to expansive areas of DMC (Riehl and Malkus 1958). On the mesoscale (e.g. length scales of 10-1,000 km), DMC generally organizes through a balance between buoyancy and environmental shear (Klemp and Wilhelmson 1978; Thorpe et al. 1982; Rotunno et al. 1988). Based on the governing dynamics and convective characteristics, organized mesoscale DMC has been classified into a variety of categories. For example, in a high vertical wind shear and convectively unstable environment, thunderstorm cells can develop rotating updrafts that are referred to as supercells (Klemp and Wilhelmson 1978). Additionally, when the shear is confined to mainly the low-levels of the atmosphere, the individual thunderstorms can remain closely connected in space, leading to an expansive region of thunderstorms greater than 100 km wide that are often referred to as

mesoscale convective systems (MCS; Houze 1993). As MCSs have been found to be the leading heavy-rain producer in the world (Nesbitt et al. 2006), it is therefore important to understand how mineral dust impacts their strength and longevity.

Before an investigation of mineral dust impacts on organized DMC can ensue, the manner in which mineral dust is ingested into the convective storms must first be understood. This problem is not simple as there are numerous types of dust events in our atmosphere that impact DMC. For example, dust may behave as a well-mixed background aerosol due to large-scale dust lofting mechanisms, such as synoptic cyclones over deserts (Knippertz et al. 2007; Lewis et al. 2010). Additionally, the cold pools of MCS and other organized mesoscale DMC events can loft large concentrations of dust that act as highly localized sources of dust. Furthermore, a third dust regime occurs when several discrete thunderstorms in a region produce their own cold pool lofted dust sources that all interact (Droegemeier and Wilhelmson 1985), thereby providing a source of dust that may have complex pathways into DMC.

As a detailed investigation regarding mineral dust ingestion by storms was not conducted prior to this dissertation, this was the first step in better understanding mineral dust impacts on organized DMC. Using the Regional Atmospheric Modeling System (RAMS), simulations of an idealized supercell storm were performed in order to investigate the mineral dust pathways into organized DMC. The methodology and results of this study, titled "Dust Lofting and Ingestion by Supercell Storms," are presented in Chapter 2 and have been published in the *Journal of the Atmospheric Sciences*. The primary finding from this study is that in order for supercells to experience significant dust ingestion, mineral dust needs to be in high concentration in the background environment. The dust that becomes lofted by the cold pools of deep convection has

a challenging pathway to become ingested by the parent convection due to the negatively buoyant air within the cold pool (Takemi 2005; Seigel and van den Heever 2012a).

With dust ingestion pathways quantified and better understood, the ways in which mineral dust impacts organized DMC can then be explored. Because the AIE impacts microphysical processes that lead to changes in condensate (Albrecht 1989), thereby altering radiative heating/cooling, the individual roles that dust plays in the microphysics and radiation of DMC must be isolated from one another in order to aid our understanding of the AIE. To accomplish this, a suite of idealized cloud resolving simulations of an MCS using RAMS was performed that utilize the technique of factor separation (Stein and Alpert, 1993; Alpert et al., 1995; Homar et al., 2003; van den Heever et al., 2006). From this study, the individual contributions of radiation, dust changing the microphysics, and the synergistic interactions between those two effects were quantified. The major findings from the study were: (1) the inclusion of radiative transfer invigorates the squall line, which was consistent with other previous studies (Tao et al. 1991,1993; Dharssi et al. 1997); (2) the AIE of mineral dust on the MCS caused a weakening, including less precipitation and a weaker cold pool; and (3) the synergy between microphysically active dust and radiation was small in magnitude, but helped slightly to better organize the squall line. The AIE findings of increased warm rain production match well with studies of AIEs that investigate the role of GCCN (Feingold et al., 1999; Cheng et al., 2009). More details on the motivation, methodology, and results of the study, titled "Assessing the Mineral Dust Indirect Effects and Radiation Impacts on a Simulated Idealized Nocturnal Squall Line," are presented in Chapter 3 of this dissertation, which has been submitted for publication in the journal *Atmospheric Chemistry and Physics*.

A specific type of MCS, the squall line (Houze and Hobbs 1982), was simulated in Seigel and van den Heever (2012b). Squall line characteristics typically consist of a leading convective line slightly trailing a strong surface cold pool, front-to-rear flow (FRF) aloft and above the surface cold pool, and a rear inflow jet (RIJ) upshear of the main convective line (Houze 2004). Numerous studies have shown the sensitivity of simulated squall lines to microphysics (Morrison et al. 2009; Bryan and Morrison 2012; Morrison et al. 2012; van Weverberg et al. 2012) and the importance of ice phase feedbacks onto squall line dynamics (Nicholls 1987; Fovell and Ogura 1988; McCumber et al. 1991; Tao et al. 1995; Liu et al. 1997; Adams-Selin et al. 2012a,b; Bryan and Morrison 2012). While investigating the simulated squall lines in Seigel and van den Heever (2012b), a previously unidentified microphysical mechanism was identified that could be modulated by AIEs and impact squall line dynamics.

It was found that for an upshear-tilted squall line the RIJ can play an integral role in recycling hail and rain hydrometeors that fall out from the updraft, back into the main convective updraft, thereby locally enhancing latent heating and generating greater positive buoyancy. In order to assess the significance of this *recirculation mechanism*, sensitivity experiments using RAMS were performed that varied the mean diameter of the hail hydrometeor size distribution, which can occur in reality via AIEs (e.g. van den Heever et al. 2006, 2011; Storer et al. 2010; Lebo and Seinfeld 2011). The primary finding from this study indicated that the recirculation mechanism helps to both sustain and invigorate squall lines, partly due to an increase in cold pool intensity. More details on the motivation, methodology, and results of the study, titled "Squall Line Intensification via Hydrometeor Recirculation," are presented in Chapter 4 of this dissertation, which is currently in review with the *Journal of the Atmospheric Sciences*.

A number of studies have shown that the cold pool plays a key role in the lifecycle and dynamics of squall lines (Thorpe et al. 1982; Rotunno et al. 1988, 1990; Weisman et al. 1988; Weisman 1992, 1993; Weisman and Rotunno 2004, 2005, 2005; Bryan et al. 2006; Adams-Selin et al. 2012a,b) and other organized mesoscale DMC (Gilmore et al. 2004; van den Heever and Cotton 2004; Dawson et al. 2010; Del Genio et al. 2012). Furthermore, it has been shown that stability of the ambient environment, which can be altered in association with the direct forcing by mineral dust (Tegen et al. 1996; Durant et al. 2009), plays a large role in the propagation and structure of cold pools (Thorpe et al. 1980; Droegemeier and Wilhelmson 1985; Bischoff-Gauss and Gross 1989; Raymond and Rotunno 1989; Hasse and Smith 1989; Jin et al. 1996; Liu and Moncrieff 1996a, 1996b, 2000). Therefore, another forcing mechanism from mineral dust on organized mesoscale DMC is through the direct effect leading to increased stability that modifies the cold pool.

In order to assess this potential forcing mechanism, a two-dimensional, non-hydrostatic model containing dry physics was developed and employed to best isolate the role that stable layers play in cold pool propagation and structure. Results showed that the height of the density current decreases and the propagation speed increases with stronger and lower stable layers, providing that the stable layer is sufficiently thin so as to not act as a gravity wave ducting layer. This finding complemented past studies of stability impacts on cold pool propagation that only examined the impacts of deep stable layers, and did not consider the role of vertically-thin stable layers, a scenario often encountered in the atmosphere (Thorpe et al. 1980; Liu and Moncrieff 2000). The motivation, methodology, and results of the study, titled "Simulated Density Currents Beneath Embedded Stratified Layers," are described and presented in detail in Chapter 5 and have also been published in the *Journal of the Atmospheric Sciences.*

The overarching goal of the research presented in this dissertation is therefore to better understand how mineral dust impacts various aspects of organized mesoscale deep moist convection. As described above, Chapter 2 explores various dust lofting regimes that result in dust ingestion by an organized supercell thunderstorm, which lays the foundation for studies of mineral dust AIEs. The research presented in Chapter 3 utilizes a squall line to quantify the roles that radiation and mineral dust microphysical interactions play in storm intensity and precipitation. Following the results from the study in Chapter 3, additional squall line simulations were performed in order to isolate a recirculation mechanism that is important for squall line maintenance, and which can be impacted by mineral dust ingestion. This analysis is presented in Chapter 4. In Chapter 5, the impact of vertically thin stable layers on cold pools is presented, and highlights the role that mineral dust ADEs can play on organized mesoscale DMC. Finally, Chapter 6 provides a summary and conclusions reached from this research.

CHAPTER 2: DUST LOFTING AND INGESTION BY SUPERCELL STORMS[1]

2.1. Introduction

Dust is likely the most abundant aerosol species in the atmosphere with global emission estimates ranging from 1,000 – 3,000 Tg yr^{-1} (IPCC 2001). It can alter the atmosphere in a variety of complex manners. Climatologically, dust directly impacts the radiative budget through the absorption and scattering of both shortwave and longwave radiation (Quijiano et al. 2000; Hansell et al. 2010). Additionally, dust indirectly affects the climate through aerosol indirect forcing that alters cloud properties and subsequent cloud radiative feedback effects (Twomey 1977; Albrecht 1989). On smaller scales, mineral dust can result in significant changes to the microphysical processes and associated precipitation rates of deep convective clouds by acting as cloud condensation nuclei (Levin et al. 1996; Rosenfeld and Nirel 1996; Feingold et al. 1999; Ramanathan et al. 2001; DeMott et al. 2003; Rosenfeld et al., 2001; Yin et al. 2002; van den Heever et al. 2006, 2011; Khain et al. 2005; 2008; Twohy et al. 2009; Storer et al. 2010) and ice nuclei (IN) (Isono et al. 1959; Roberts and Hallett, 1968; Zuberi et al. 2002; DeMott et al. 2003; Sassen et al. 2003; Field et al. 2006; Mohler et al. 2006; van den Heever et al., 2006). While it is well known that mineral dust impacts cloud microphysics by acting as nuclei, our understanding of the manner in which mineral dust is ingested into deep convective storms is not well understood. This is due in part to the numerous types of dust events in our atmosphere and the poor representation of these different events in modeling experiments that investigate dust impacts on atmospheric processes.

[1] ©American Meteorological Society. Used with permission.

While all mineral dust in the atmosphere initially comes from surface lofting by strong winds (Tegen and Fung 1994; Liu et al. 2007), the vertical distribution and concentrations of dust are different within specific meteorological events. First, the most prolific dust events occur due to large-scale dust lofting mechanisms, such as synoptic cyclones over deserts (Knippertz et al. 2007; Lewis et al. 2010), when mineral dust can be lofted higher than the boundary layer and transported over large distances. This mechanism can allow dust to behave as a well-mixed background aerosol. One example of this is the Saharan Air Layer (SAL), whereby a layer of Saharan dust has been found to affect convection as far west as the eastern United States (Prospero 1996,1999; Perry et al. 1997; Sassen et al. 2003). The numerical representation of this dust regime, where dust is treated as a well-mixed background aerosol, is commonly used when studying dust impacts on convection (e.g. van den Heever et al. 2006, 2011; Zubler et al. 2011). A second commonly occurring dust regime occurs when convectively generated cold pools loft large concentrations of dust that are localized, being contained behind the gust front (Figure 2.1). These mesoscale dust storms, by which we mean the wall of dust within a cold pool (Figure 2.2), are commonly referred to as haboobs (Sutton 1925; Lawson 1971) and occur within and beyond the reaches of the largest desert regions in the world. Within arid regions it has been found that these mesoscale dust storms can account for up to 30% of the regional dust mass budget (Miller et al. 2008). However, few dust studies truly represent the lofting of dust by the cold pool in order to understand its impacts on parent convection (Tulet et al. 2010). A third dust regime occurs when several discrete thunderstorms in a region produce their own boundaries and dust storms that all interact (Droegemeier and Wilhelmson 1985). In this regime, developing or mature convection could have access to multiple localized sources of dust. However, the pathways and the extent of dust ingestion by storms within this regime have not yet been

examined. These various dust regimes demonstrate the complexities involved with correctly representing dust transport and ingestion in a numerical model.

Observational studies have found large concentrations of dust within convection (Levin et al. 1996; DeMott et al. 2003; Jensen et al. 2004; Twohy et al. 2009), however collecting in situ dust ingestion data for these various regimes is extremely difficult and dangerous as high concentrations of dust damage plane engine turbines and clog air filtration systems (Miller et al. 2008). As a result, the method of obtaining a quantitative assessment of these data has typically been through numerical analyses (Takemi 2005; Tulet et al. 2010) using dust emission parameterizations that are shown to be accurate on the global scale (Kang et al. 2011). However, the grid-spacings used in global simulations make it difficult to resolve the small-scale circulations and sharp gradients associated with the cold pool that aid in dust lofting, transport, and subsequent ingestion by convection (Marsham et al. 2008; Reinfried et al. 2009). Therefore, precise ingestion pathways into the updraft of deep convective storms are still largely unknown.

The goal of this paper is therefore to gain a better understanding of the pathways by which dust is ingested by mesoscale storms within commonly observed dust regimes through the use of a high-resolution cloud-resolving model. To accomplish this goal, the Regional Atmospheric Modeling System (RAMS) (Pielke et al. 1992; Cotton et al. 2003; Saleeby and Cotton, 2004) coupled with an interactive dust model (Smith 2007) is used to simulate a supercell thunderstorm within three commonly observed dust regimes. First, we simulate an idealized supercell within a horizontally homogeneous background dust profile to represent the ingestion of dust by a storm initiating within an already dusty atmosphere (e.g. the SAL, referred to as EXP-BACKGROUND). Second, we simulate the contribution and ingestion of mineral dust produced purely by the mechanics of the supercell itself (e.g. the haboob, referred to as

EXP-STORM) by utilizing a surface dust emission scheme and an initially dust-free background environment. Third, an independent surface convergence boundary is added to the domain ahead of the supercell to investigate dust ingestion resulting directly from the interaction between the supercell-produced gust front and the imposed convergence boundary (e.g. haboob interactions, referred to as EXP-BOUNDARY). These three model experiments represent a range of possible dust pathways into convection for commonly occurring dust regimes. The results of these experiments will aid future investigations into dust impacts on precipitation processes by demonstrating the sensitivity that differing dust sources has on ingested dust concentrations and locations.

The following section briefly describes the model used for these simulations with emphasis placed on pertinent schemes and the numerical setup for each experiment. Section 3 presents results from all three experiments and Section 4 provides discussion and conclusions of the results from each experiment. This paper is the first in a series of experiments dedicated to the understanding of mineral dust ingestion and its impact on the parent convection. The goal of this first paper is solely to understand the ingestion pathway of mineral dust into the lower region of a supercell within common dust regimes. Therefore, mineral dust in this experiment is not microphysically active.

2.2. Methods

2.2.1. Model description

The numerical model that was used for this study is the non-hydrostatic RAMS model (Pielke et al. 1992; Cotton et al. 2003; Saleeby and Cotton, 2004), which uses a staggered Arakawa-C grid. RAMS is appropriate for this numerical study because of its sophisticated microphysical, surface and mineral dust parameterization schemes. The two-moment microphysical scheme (Meyers et al. 1997) predicts both mass mixing ratio and number concentrations of the hydrometeor species. The water species are categorized in eight forms: vapor, cloud droplets, rain, pristine ice, snow, aggregates, graupel and hail (Walko et al. 1995). Within each category, the hydrometeors are assumed to conform to a generalized gamma distribution (Flatau et al. 1989; Verlinde et al. 1990). The bulk microphysical schemes within RAMS contain added sophistication by accessing previously generated lookup tables for the nucleation of aerosol species such as CCN, giant cloud condensation nuclei (GCCN), and IN. The reader is referred to Saleeby and Cotton (2004) for a detailed description regarding the activation of CCN and GCCN, and Meyers et al. (1997) regarding IN.

At the surface, RAMS divides each grid cell into a patchwork of water, bare soil, and vegetation over shaded soil that interacts with an online surface model, LEAF3 (Walko et al. 1995). For these experiments bare soil was chosen to represent 100% of each grid cell as we are examining dust storm development in arid regions.

Surface and soil studies have provided the information necessary to construct a model containing reliable surface dust emission, deposition and transport within RAMS that

communicates online with LEAF3 (Smith 2007). Dust emission is diagnosed only when a surface wind velocity threshold value is reached and is a function of surface wind speed, soil type, and soil moisture (Marticorena and Bergametti 1995; Fecan et al. 1999). The wind threshold velocity for dust lofting is strongly dependent on particle diameter, therefore the user must choose a soil size distribution to represent bare soil. For this experiment the soil distribution is based on Tegen and Fung (1994) and contains only silt and clay. The dust particle size distribution is partitioned into seven size increments, where sizes 1-4 represent clay and sizes 5-7 represent silt (Table 2.1). With respect to mass, silt constitutes 90% of the erodible materials, while clay is responsible for the remaining 10%. The partitioning of dust into multiple sizes allows for a more accurate representation of surface dust lofting.

If the wind speed at 10 m is greater than the computed wind threshold over moist soil (U_{twet}) and soil volumetric moisture content is less than 50% of saturation, then dust is allowed to be lofted from the surface. The amount of dust mass emitted from the surface is parameterized as a mass flux that is a function of 10m wind speed and wind threshold velocty (Gillette and Passy 1988; Ginoux et al. 2001). From the mass flux, number concentrations for each particle size are computed using an assumed density of 2500 kg m^{-3} for clay and 2650 kg m^{-3} for silt (Tegen and Fung 1994). Finally, the number concentrations for each clay size are summed up and added to the existing concentrations for clay species (referred to as the small dust mode), while the same procedure is performed for the silt species (referred to as the large dust mode). This summation results in a single concentration for both the small and large dust mode. After lofting, the subsequent dust removal and transport schemes perform calculations with respect to these two modes. This results in a two bin representation of dust within RAMS.

The removal mechanisms of each dust mode within the model include gravitational

settling (Baron and Willeke 2001) and below-cloud scavenging by precipitation for all model levels below cloud base (Slinn 1981). The reader is referred to Smith (2007) for a more detailed summary of these parameterizations. Research is currently underway to develop parameterization schemes representing the scavenging and nucleation of mineral dust to form cloud droplets and ice crystals within cloud. As such, mineral dust in this experiment is not microphysically active and is simply used as an active tracer to investigate ingestion by supercell storms. As the goal of this paper is to investigate mineral dust ingestion into supercells this should not significantly impact the results.

2.2.2. Experimental design

In this study, three idealized simulations are performed of a supercell to understand how mineral dust becomes entrained into such storms. To best resolve the cold pool and turbulent eddies responsible for dust lofting and transport, RAMS is configured as a high-resolution cloud resolving model (CRM). Table 2.2 summarizes the model configuration for all simulations. The horizontal grid has a spacing of 300 m and the vertical grid spacing closest to the surface is 25 m and increases by 10% for each higher model level until a maximum of 300 m is reached, above which it stays at 300 m.

To initiate convection, a 10 km wide, 2km deep warm bubble containing a uniform thermal perturbation of 2 K (Table 2.2) is used within a convective environment following Weismann and Klemp (1982) (Figure 2.3). In addition to the thermodynamic profile, the veering wind profile favors the development of a right moving supercell (Weismann and Klemp 1984). Supercell evolution within each experiment is identical. The following subsections briefly

describe the dust regime used for each model experiment, the details of which are summarized in Table 2.3. For cloud and ice nucleation within all experiments, background concentrations of 1600 cm^{-3} and 10,000 kg^{-1} are used for aerosol species that can be activated as CCN and IN, respectively (Table 2.2). These aerosols are independent of the dust species.

2.2.2.1. EXP-BACKGROUND

For this experiment, the surface dust emission parameterization is turned off and an initial horizontally homogeneous environmental profile of dust (Figure 2.4) is used to represent the development of supercells within an already dusty environment. The vertical profile used to initialize the model consists of a surface concentration of 1000 cm^{-3} that linearly decreases to 20 cm^{-3} by 4 km AGL and is then held fixed at 20 cm^{-3} within the remainder of the domain. This vertical profile was chosen following observations documented by Chen and Fryrear (2002) of a mid-latitude haboob in Big Spring, Texas. They measured a maximum concentration within 15 m of the surface of 1.3 x 10^3 μg m^{-3} which, when using a mean particle diameter of 0.8μm and a density of 2500 kg m^{-3} (small dust mode) produces a particle number concentration of ~ 1250 cm^{-3}. Surface dust emission is absent in this experiment, however the remaining schemes within the dust model are still active, including dry deposition and below-cloud scavenging by precipitation.

2.2.2.2. EXP-STORM

In order to examine the contribution of ingested dust following lofting purely by the supercell itself, this simulation initially contains no background dust. The surface dust emission within the dust model is enabled. With no initial background dust (unlike EXP-BACKGROUND), all dust produced in this experiment originates from the surface. This provides a means to assess dust ingestion pathways into a supercell of that dust produced purely by the storm's own kinematics.

2.2.2.3. EXP-BOUNDARY

The aim of this experiment is to further our understanding of mineral dust ingestion as a direct result of outflow boundary interactions. The numerical setup of this experiment is identical to EXP-STORM (full dust model and no initial background dust), except that 95 minutes after initialization, an independent surface convergence boundary is introduced ahead of the supercell outflow boundary. The addition of the surface convergence boundary at this time allows for (1) sufficient time for numerical stabilization of the boundary, and (2) the interaction with the supercell outflow boundary during the analysis times of the other two experiments, thus facilitating experiment comparisons. This additional convergence boundary will also contribute to lofted dust within the environment, thus making it potentially available for ingestion by the supercell, similar to what might be seen in reality in an environment populated by numerous discrete storms. The convergence boundary is initialized by instantaneously inserting a north-south oriented -5K thermal perturbation that is 1 km deep (surface to 1 km AGL) and positioned

20 km ahead of the approaching right moving supercell. The cold, dense air generates two horizontally propagating outflow boundaries – one to the east and one to the west. The depth and temperature perturbation were chosen through trial-and-error in order to produce surface wind speeds and lofted dust concentrations similar to that produced by the supercell itself in EXP-STORM, thereby allowing for appropriate comparisons between experiments. The western outflow boundary of the convergence zone interacts with the supercell gust front and will be the focus of analysis. The following section first presents results pertaining to the supercell evolution for all three experiments and is followed by specific results from the three experiments just described

2.3. Results

2.3.1. Supercell evolution and analysis

As mentioned in the previous section, a warm bubble is used to initiate convection. After 45 minutes, the main updraft shows signs of splitting into a right and left mover (Klemp and Wilhelmson 1978b) due to the strong vertical wind shear of the environment (Weisman and Klemp 1982). To demonstrate the evolution of the split, Figure 2.5 shows convection after 55, 85, 115, and 145 minutes into the simulation. The filled contours are model emulated radar reflectivity at the lowest model level (~ 12 m AGL) to emphasize surface characteristics, and which has been calculated following the methodology of Matrosov (1999). After 85 minutes the split can be seen in the surface reflectivity field with a clear separation in maximum dBZ. By 115 minutes, the right moving supercell has taken on the appearance of a classic cyclonically

rotating supercell (Weismann and Klemp 1984), where a hook is evident in both the reflectivity field and cold pool boundary on the southern flank of the storm. Thirty minutes later, the right mover is still well organized and is the dominant supercell due to the veering wind profile imposed (Weismann and Klemp 1984). The path of the supercells can be seen via the accumulated surface precipitation (Figure 2.5), where a right turn is evident in the southernmost cell. The cold pool boundary has been calculated following the methodology of Tompkins (2001) where the cold pool is defined by air with -0.04 m^2 s^{-1} buoyancy relative to the domain averaged buoyancy at the desired model level. Because the right moving supercell is the dominant cell simulated and the structure remained stable throughout the simulations, all analysis in this section is in regard to the right moving supercell.

During analysis of the right moving supercell, a 15-minute period demonstrated strong cold pool forcing that generated a hook feature in the precipitation fields. Figure 2.6a-d shows the cold pool (thick black contour) shape and characteristics during this time period after 105, 110, 115, and 120 minutes, respectively. It can be seen in Figure 2.6 a-d that after 120 minutes the southern portion of the cold pool pushes farther east than the cold pool region to the north as a result of being driven by a surge of air from the rear flank downdraft (RFD) (Markowski 2002). This surge has reached the gust front and can be seen in the surface wind field (thin solid contours), whereby a small portion of >12 m s^{-1} winds have been pushed ahead of the main surface wind maximum. This local wind maximum along the RFD gust front is also associated with a tongue of colder air (shaded contours) that is aiding in forcing the RFD gust front through baroclinic generation of horizontal vorticity (Markowski 2003). The RFD surge seen in this 15-minute period produces the hook shape in both cold pool and surface reflectivity that is a typical characteristic of a supercell. It is hypothesized that when a hook signature is present, this is the

most likely time period that tornadogenesis can take place as RFD-produced vorticity can be coupled with the supercell low-level mesocyclone (Markowski et al. 2008). This coupling aids in the collocation of the surface and cloud-base updrafts, which in turn would assist with dust ingestion. Thus, the time period from 105 to 120 minutes, which encompasses the development of the hook echo, will serve as the focus of this analysis.

Additionally, it is important to mention that dust analysis presented herein is with respect to the small dust mode. This mode has been chosen as analysis showed dust ingestion pathways between the small and large dust modes to be virtually the same. As the focus of this paper is on the ingestion pathways into the storm, presentation of both dust modes is redundant.

2.3.2. EXP-BACKGROUND

This experiment examines supercell development in a dusty environment with no contribution from surface lofting. To illustrate the three-dimensional nature of dust ingestion, Figures 2.7 and 2.8 show various two-dimensional cross sections (at 105min and 120 min, respectively). Unless otherwise stated, all dust concentrations are shown as concentrations relative to background levels (i.e. the initial dust profile imposed), which provides a more representative assessment of ingestion.

Beginning at the surface, Figure 2.7a shows a plan-view of the mineral dust distribution, cold pool boundary, and wind flow associated with the right moving supercell. It can be seen that within the RFD cold pool, the dust concentrations are significantly lower than the low-level ambient concentrations of dust. This is due to the advection of less dusty air from aloft to the surface by the storm downdraft. As the RFD transports less dusty air, the surface wind spreads

this “cleaner” air mass throughout the cold pool, while the remainder of the surface air contains near background levels of dust.

Moving higher aloft towards cloud base, which is located around 1800 m AGL, Figure 2.7b shows a plan-view at 2 km AGL illustrating the dust distribution and upward and downward fluxes associated with the updraft and downdraft of the supercell, respectively. The dust concentration and dust flux fields together demonstrate dust ingestion near cloud base. The positive flux values in conjunction with elevated dust concentrations illustrate the region of maximum dust ingestion, whereby updraft air is advecting higher concentrations of dust from below cloud base into the storm. Conversely, regions of large negative fluxes depict the region of the storm that is transporting dust from within the storm to lower levels. It can be seen that the area of largest positive vertical flux at 2 km AGL occurs ahead of the maximum dust concentration at this level, while the largest negative vertical flux occurs behind the maximum concentration. This signature shows the motion and ingestion of the supercell – as the supercell propagates towards the east, the updraft atop the surface cold pool raises the dust concentration (shown by large fluxes) and shifts the dust distribution and concentration maximum farther east.

To further illustrate the flow regime and ingestion within the region of largest dust concentrations, Figure 2.7c shows an east-west vertical cross section through the 2 km AGL maximum dust concentration. From this figure it can be seen that a large region of elevated dust concentrations exists, however the largest elevated dust concentrations at any vertical level still remain within the updraft while the lowest elevated concentrations are confined to the downdraft. The upward vertical motion ahead of the cold pool and just below cloud base (i.e. the main updraft) is occurring where large elevated dust concentrations are present. This indicates that the

transport of dust into the parent storm in this case occurs due to the updraft within the top of the boundary layer, where vertical motion and high dust concentrations are co-located.

To isolate the contributions of dust ingestion due to the horizontal and vertical components of the wind, Figure 2.7d shows upward dust flux in the shaded contours and horizontal dust flux in vector form, where the length of the vector indicates the magnitude of the horizontal dust flux (maximum value is ~ 14 cm^{-2} s^{-1}) and the vector direction indicates flux direction in the x-y plane through the cross-sectional surface. To best isolate dust ingestion into the storm, which is the primary focus of this experiment, the flux values within the cold pool and associated with the downdraft are removed from the figure for this analysis. The vertical cross-section location, cold pool boundary, and condensate boundary in 7d are the same region as in Figure 2.7c. Within the main updraft, dust is fluxed both vertically and towards the northwest. Conversely, within the backside of the updraft and the downdraft dust is being advected from the east and northeast, respectively. This cyclonic turning of the advective motion is in agreement with the typical cyclonic circulation of right moving supercells (Weismann and Klemp 1982). As previously mentioned, the majority of the dust ingestion in this experiment after 105 minutes occurs out ahead of the cold pool from the upper portion of the boundary layer into the updraft. This is reinforced quantitatively in Figure 2.7d by the relative values of upward dust flux and horizontal dust flux. The large spatial coverage of upward dust flux into cloud base is co-located with the updraft of the storm, similar to 7c, and has values on the order of 1000 x 10^3 cm^{-2} s^{-1}. Conversely, horizontal dust flux, which can be related to lateral entrainment, has maximum values on the order of 10 x 10^3 cm^{-2} s^{-1} near the center of the updraft and decreases toward cloud boundary. The two orders of magnitude difference between the vertical and horizontal dust flux shows that dust ingestion is mainly driven by the vertical component of the wind, i.e. the updraft.

Figure 2.8 is identical to Figure 2.7, except for 120 minutes into the simulation, which is the time at which the RFD gust front has strongly pushed ahead of the northern gust front in a hook shape, as described earlier. When comparing the two figures, the magnitudes and characteristics of the quantities plotted are virtually the same, indicating that even after strong cold pool forcing has occurred, dust ingestion into the updraft remains virtually the same. While the storm updraft strength within the boundary layer may be dependent on the cold pool, this 15-minute period indicates ingestion of background dust by the supercell is somewhat independent of the cold pool forcing, as long as the updraft has access to the dusty environmental air near the top of the boundary layer out ahead of the storm.

To more precisely identify dust ingestion into supercells from a dusty atmosphere, Figure 2.9 shows parcel trajectories into the supercell during this 15-minute period. These offline parcel trajectories are calculated using model data with a temporal resolution of one minute that are spatially and temporally interpolated to 10 m and 1 second, respectively, to allow for more precise trajectories. The trajectory calculations are performed following the resolved flow fields and do not include the effects of dust sedimentation, which is a reasonable assumption for vertical speeds associated with supercells. Figures 2.9a and 2.9b show parcel initialization at 105 minutes relative to the surface and the dashed vertical plane (depicted in 9a), respectively. Among hundreds of parcel releases, twenty parcels most representative of both cold pool and environmental air at different heights AGL are shown in their respective horizontal and vertical locations (Figures 2.9a and 2.9b). After 15 minutes of trajectory analysis, the final locations of the twenty parcels are shown in 9c and 9d relative to the horizontal and vertical planes, respectively. The parcels that were ingested deep into the updraft were initially located ahead of the cold pool and well above the surface, therefore confirming the dust ingestion pathway of

environmental dust by the supercell from the top of the boundary layer ahead of the cold pool and into the updraft.

2.3.3. EXP-STORM

The purpose of the second experiment is to examine the ingestion of dust lofted purely by the supercell itself. This is achieved by modeling the storm within an initially dust free environment and making use of the dust emission scheme to allow for the lofting of dust by the winds within the cold pool. Figures 2.10 and 2.11 show the same plots (at 105min and 120 min, respectively) as Figures 2.7 and 2.8.

At 105 minutes into the simulation, the surface distribution of dust (Figure 2.10a) is closely linked to that of the surface winds (maximum plotted vector is ~ 21 m s^{-1}), as dust lofting is strongly dependent on the 10 m wind speed. The strong surface winds that are generated by the RFD loft and transport the mineral dust within the RFD cold pool, distributing the dust both horizontally (Figure 2.10a) and vertically (Figure 2.10c). As shown in Figure 2.10a, the range of maximum lofted dust concentrations are ~ 1100-1700 cm^{-3}, which are relatively consistent with haboob observations from Chen and Fryrear (2002) who measured 15 m AGL dust concentrations of ~ 1250 cm^{-3}. Although the maximum simulated surface dust concentrations are larger than the haboob observations, it is to be expected given that the supercell simulated in this experiment produced surface winds in excess of 20 m s^{-1} while the haboob only produced a maximum surface wind of 14 m s^{-1}.

As the dusty cold pool propagates within the ambient air, turbulent mixing at the leading edge of the RFD cold pool allows the dusty air to become mixed with the unstable environmental

air (Figure 2.1) and associated low-level updraft (as will be seen later in this section). The dusty air at the leading edge of the RFD cold pool is detrained from the cold pool and forced into the rearward portion of the main updraft of the supercell. This produces a 2 km AGL maximum dust concentration of ~ 30 cm^{-3} (Figure 2.10b) from a pathway closely tied to the RFD gust front (Figure 2.10d). Even though the cold pool in EXP-STORM produces surface dust concentrations larger than the maximum background concentration in EXP-BACKGROUND, significantly lower concentrations are ingested into the updraft of EXP-STORM (~ 30 cm^{-3}) compared with that in EXP-BACKGROUND (~ 500 cm^{-3}). Additionally, the horizontal spatial extent of the vertical dust flux (Figure 2.10d) is very narrow in comparison with EXP-BACKGROUND (Figures 2.7d and 2.8d). The large differences in both magnitude and spatial extent of ingested dust between EXP-STORM and EXP-BACKGROUND demonstrates how difficult it is for a supercell to ingest dust produced by its own cold pool as opposed to dust that is available from the ambient environment. While haboobs are associated with large concentrations of dust kicked up within the cold pool, the majority of this dust may not make it into the parent storm's updraft.

After 120 minutes of simulation time (Figure 2.11), the dust ingestion pathway has shifted further north as a result of the RFD surge that generated the hook echo. As the RFD winds surged further east relative to the forward-flank downdraft (FFD), the low-level winds formed a vertically stacked circulation (note the more upright distribution of upward dust flux in Figure 2.11d versus Figure 2.10d) beneath the 2 km AGL maximum dust concentration that closely resembles the location of classical supercell tornadogenesis (Lemon and Doswell 1979; Markowski 2002; Lerach et al. 2008; Snook and Xue 2008). This new region, which is still closely tied to the gust front (Figure 2.11d), advects approximately two times more dust into the updraft as compared with 15 minutes earlier (Figure 2.10) and contains much larger vertical

fluxes. Similar to EXP-BACKGROUND, the relative contributions of horizontal (values near cloud base are ~ 1 x 10^3 cm^{-2} s^{-1}) and vertical dust fluxes (values near cloud base are ~ 30 x 10^3 cm^{-2} s^{-1}) to dust ingestion shows that dust ingestion is dominated by the vertical wind. While the horizontal location of maximum dust ingestion changes between 105 and 120 minutes, the dependency on the RFD cold pool boundary remains consistent, and ingestion into the rearward portion of the updraft occurs at the cold pool and ambient air interface. Although the dust concentrations ingested by the supercell have doubled by this time, they remain an order of magnitude smaller than the dust concentrations ingested by EXP-BACKGROUND thus further demonstrating the difficulty for cold pool-produced dust to become ingested by the parent supercell.

To more precisely identify dust ingestion pathways into supercells from dust originating at the surface within the cold pool, Figure 2.12 shows parcel trajectories into the supercell during this 15-minute period. Similar to Figure 2.9, Figures 2.12a and 2.12b show twenty parcels that best represent the transport processes occurring in the cold pool and at the gust front where dust is present. The parcels are initialized at 105 minutes relative to the horizontal and the vertical plane using the same methodology for EXP-BACKGROUND trajectory analysis. The final locations of the twenty parcels are shown in 12c and 12d relative to the horizontal and vertical planes, respectively.

Results from this trajectory analysis coincide with results shown in Figures 2.10 and 2.11. The only parcel to be ingested by the supercell and transported higher than 4 km AGL originated from within the cold pool, as shown by the 300 m AGL darkest blue parcel, confirming the cold pool origin of ingested dust by the supercell. At the start of the 15-minute trajectory analysis, the ingested parcel was located near the RFD surge (shown by large wind vectors within cold pool of

Figure 2.12a and 2.12b) where increased convergence was occurring. The increased convergence (not shown) enhanced the turbulent mixing along its pathway thereby allowing detrainment of this parcel from the cold pool into the updraft where it is subsequently ingested by the supercell. For EXP-STORM, these trajectories confirm the aforementioned results that dust ingested by the supercell originates within the RFD cold pool winds and is detrained at the gust front surface, resulting in entrainment within the rearward portion of the updraft.

2.3.4. EXP-BOUNDARY

To further study the ingestion of dust by supercell storms within common dust regimes, the third experiment aims to investigate the influence of an additional surface convergence boundary on dust ingestion. This is an important experiment because several supercells or deep convective storms commonly form within the same environment, resulting in numerous boundary collisions (Bluestein and Weismann 2000). Figures 2.13, 2.14 and 2.15 show similar plots as Figures 2.10 and 2.11, but because the boundary interaction takes place relatively quickly, the times presented are at 105, 107, and 109 minutes into the simulation, respectively.

Ten minutes after the boundary initialization (Figure 2.13) the surface boundary can be seen to the east of the supercell cold pool. The convergence boundary has surface dust lofting (Figures 2.13a,c) comparable to the leading edge of the RFD gust front, with maximum values of ~ 700 cm^{-3}. Additionally, the convergence boundary is advecting dust into the boundary layer air ahead of the supercell, both horizontally and vertically (Figure 2.13d). As the boundary collides with the supercell gust front at 107 minutes (Figure 2.14), interaction can be seen first near the surface, where the distribution of dust within the supercell cold pool and the convergence

boundary cold pool appear to merge (Figure 2.14c). While dust is being ingested in a similar fashion to EXP-STORM via the supercell RFD cold pool, dust can also be seen beginning to enter the supercell near cloud base farther ahead of the RFD cold pool (Figure 2.14 b and d), providing an additional dust ingestion pathway into the supercell at this time. As the convergence boundary lofts dust into the boundary layer air ahead of the supercell, the supercell updraft begins to ingest the dusty environmental air through a similar pathway as EXP-BACKGROUND. Two minutes later (Figure 2.15), full boundary interaction has taken place and the 2 km AGL concentration values have doubled due to the combination of boundary- and supercell-forced ingestion. Vertical advection of dust has also increased both in magnitude and height AGL because of (1) increased concentrations of dust due to the combination of RFD and convergence boundary produced dust, and (2) the enhanced updraft as a result of the boundary collision (Droegemeier and Wilhelmson 1985). The plume of mineral dust that has been ingested into the main updraft of the supercell as a result of the boundary interaction can be seen in Figure 2.15c, where a "tower" of >50 cm^{-3} is present. After this time (109 minutes), the supercell propagates over the cooler and more stable air in the wake of the convergence boundary and this leads to weakening and eventual dissipation of the supercell.

Using the same analysis as previously, parcel trajectories for this simulation are shown in Figure 2.16. In general, the parcels that were ingested into the main updraft of the supercell as a result of the boundary collision originated primarily from the ambient air (dark red and dark blue parcels in Figures 2.16c,d). As shown with Figures 2.13-2.15, dust lofted by the imposed convergence boundary is advected into the ambient air through westward and vertical advection at the gust front. This advected dust is then ingested into the supercell updraft prior to the arrival of the supercell cold pool. These trajectories (Figure 2.16) confirm the aforementioned results of

this experiment that for this environmental regime dust ingested into the supercell is enhanced by dust within the ambient air ahead of the supercell cold pool that is generated by the convergence boundary.

2.4. Discussion and conclusions

The overall goal of this experiment is to gain a better understanding of mineral dust ingestion pathways into severe convective storms. The three simulations performed in this experiment were designed to emulate some of the more common environmental regimes that provide a source of dust for ingestion by supercell storms. The first simulation, EXP-BACKGROUND, investigated a regime in which a supercell develops in an already dusty atmosphere in order to examine dust ingestion by the supercell solely from the environment. Conversely, EXP-STORM explored the regime in which a supercell develops in a dust free environment and the only dust available for ingestion is generated by the supercell itself. Lastly, EXP-BOUNDARY investigated dust ingestion pathways within the regime of a convergence boundary interacting with a supercell whereby both phenomena loft their own dust within an initially clean environment. The three dust regimes simulated in this experiment provide a range of possible dust pathways into convective storms and represent common dust environments observed in reality and utilized in numerical investigations.

The results of the three simulations demonstrate substantial differences in the location and quantity of dust ingested by the supercell. If the only source of dust is within the environmental air (i.e. EXP-BACKGROUND) then relatively large amounts of dust originating from upper region of the boundary layer ahead of the cold pool is ingested predominantly by the

vertical component of the supercell updraft. Conversely, if the atmosphere is originally void of mineral dust and the only dust lofted into the atmosphere is due to the kinematics of the supercell cold pool (i.e. EXP-STORM), then relatively small concentrations of are ingested by the supercell via a very narrow region at the edge of the RFD cold pool. Dusty cold pool air is detrained at the interface between the cold pool and the ambient air and then entrained into the rearward portion of the updraft just ahead of the gust front. When investigating the influence of a convergence boundary on dust ingestion (i.e. EXP-BOUNDARY), it is seen that boundary interactions with supercells can enhance mineral dust ingestion in an initially clean environment by (1) acting as a source of background dust out ahead of the cold pool beneath the updraft, and (2) by enhancing the strength of the updraft and hence vertical advection as a result of the collision. These experiments show that large differences can arise in the manner in which dust is ingested by supercell storms, as well as in the concentrations of the ingested dust. This also demonstrates the necessity of an appropriate dust representation for numerical investigations.

While this study is not the first to our knowledge to directly simulate a mesoscale dust storm using a dust emission scheme, it is the first experiment that directly investigates and compares dust ingestion contributions from different production sources. Takemi (2005) simulated an idealized squall line in the Gobi Desert with 2 km grid spacing in order to study mineral dust transport from dust produced by the cold pool. He concluded that strong cold pool wind is the source of mineral dust lofting, and that turbulence at the leading edge of the cold pool acts to detrain dust out of the cold pool and into the updraft at the cold pool edge. Additionally, Tulet et al. (2010) simulated mesoscale convective systems (MCS) with a finest grid spacing of 3 km over Niger and found a similar mechanism for dust entrainment into the parent convection. The dust lofting and ingestion process found in these studies are in agreement with the EXP-

STORM results shown in this paper. The amount of dust ingested relative to dust lofted in Takemi (2005) and Tulet et al. (2010) is approximately 10%, which is also exhibited here in EXP-STORM. This provides increased confidence in the kinematic mechanism of dust ingestion by storms from cold pool lofting within a clean atmosphere. However as previously mentioned, the dust regime simulated by Takemi (2005) and Tulet et al. (2010) of a convective complex lofting and ingesting dust within an initially clean environment is only one common regime.

As shown in this paper, deep convection propagating within an initially dusty atmosphere can dramatically enhance ingested dust concentrations, whereby the ratio of dust ingested to the largest background concentration is close to 1. In EXP-BACKGROUND the environment initially contained 1000 cm^{-3} of dust near the surface and the supercell contained ~ 1000 cm^{-3} in the updraft at 4 km AGL. This contribution to the storm is significantly larger than exhibited in EXP-STORM and the experiments of Takemi (2005) and Tulet et al. (2010). Such variations in the dust concentrations can significantly impact the microphysical responses of precipitation processes (van den Heever et al. 2006). Additionally, this paper has shown that nearby convergence boundaries can further complicate the method of dust ingestion by a supercell storm by providing an additional source of environmental dust.

The large differences in ingested dust concentrations between the three simulations presented in this paper demonstrate (1) how efficiently a supercell propagating within a dusty atmosphere ingests mineral dust; (2) the relative difficulty of a supercell being able to ingest its own lofted dust; (3) the role additional surface boundaries play in enhancing dust ingestion by the parent storm, and (4) the importance of choosing an appropriate dust initialization method when simulating dust storms.

Although it is known that mineral dust acts effectively as CCN and IN (Twohy et al.,

2009), the mineral dust simulated in this experiment is not microphysically active. As such, the analysis presented in this paper only pertains to the ingestion pathway of dust into supercell storms and the relative amounts of dust ingested depending on the dust source. Research is currently in progress to allow dust to nucleate to form cloud droplets and ice. This will permit analysis of the microphysical implications of mineral dust ingestion within common dust regimes, along with analysis pertaining to vertical dust redistribution and radiative effects.

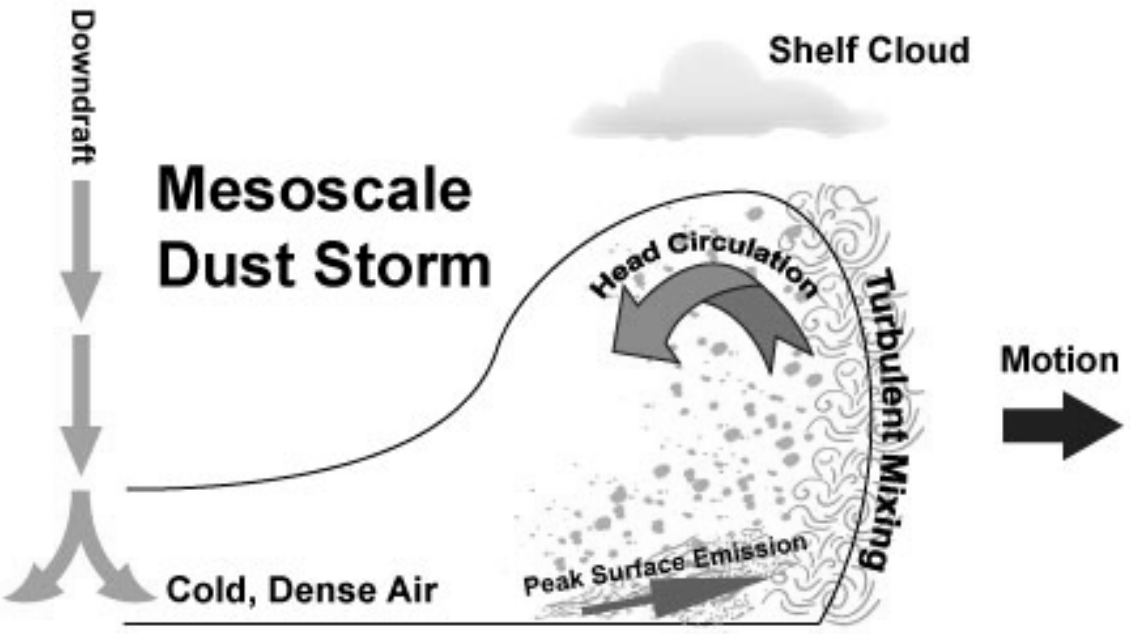

Figure 2.1. Idealized schematic of a mesoscale convective dust storm. As negatively buoyant air from the downdraft collides with the surface, it spreads laterally and generates a density current. The strongest surface winds reside just behind the gust front where large concentrations of dust are present, providing the "dust wall" appearance seen in Figure 2.2, Strong turbulent mixing at the gust front acts to detrain small amounts of dust from the cold pool air mass.

Figure 2.2. Image of strong dust storm that impacted Phoenix, AZ on 6 July 2011. This photo was taken from the National Weather Service (NWS) Phoenix office in Tempe, AZ at 19:45 MDT. Source: http://www.wrh.noaa.gov/psr/pns/2011/July/DustStorm.php

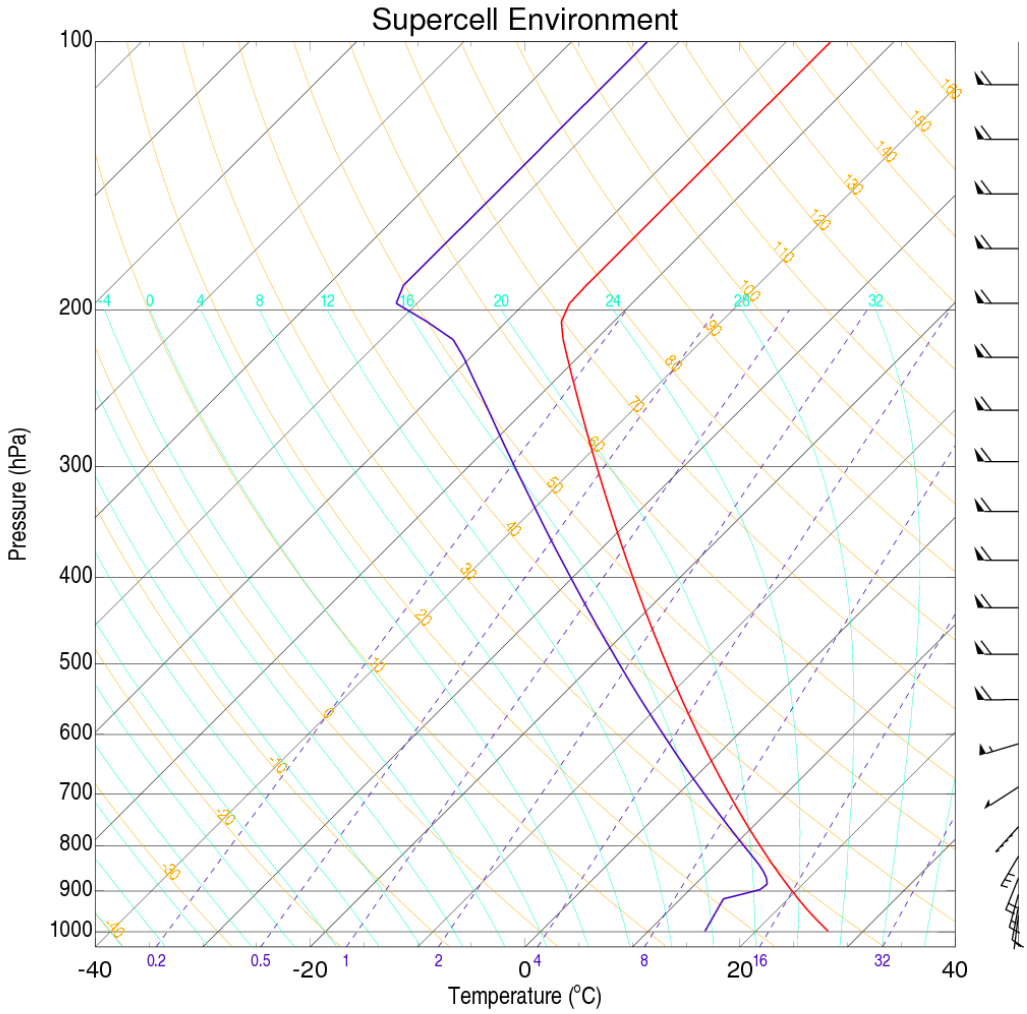

Figure 2.3. Horizontally homogeneous environmental conditions initialized for all simulations. Red is the temperature profile and blue is the dew point profile. Following Weismann and Klemp (1982).

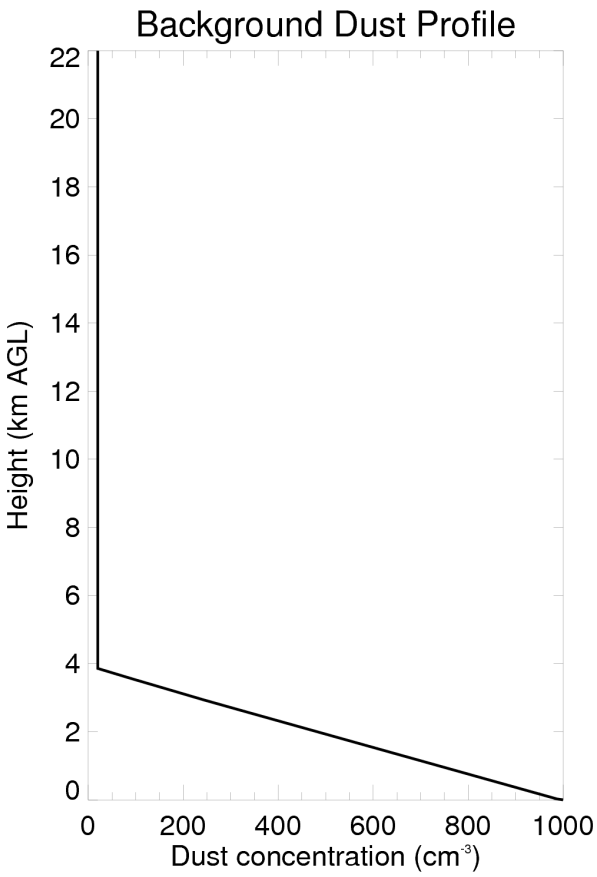

Figure 2.4. Horizontally homogeneous dust profile (cm^{-3}) used for initialization of the EXP-BACKGROUND.

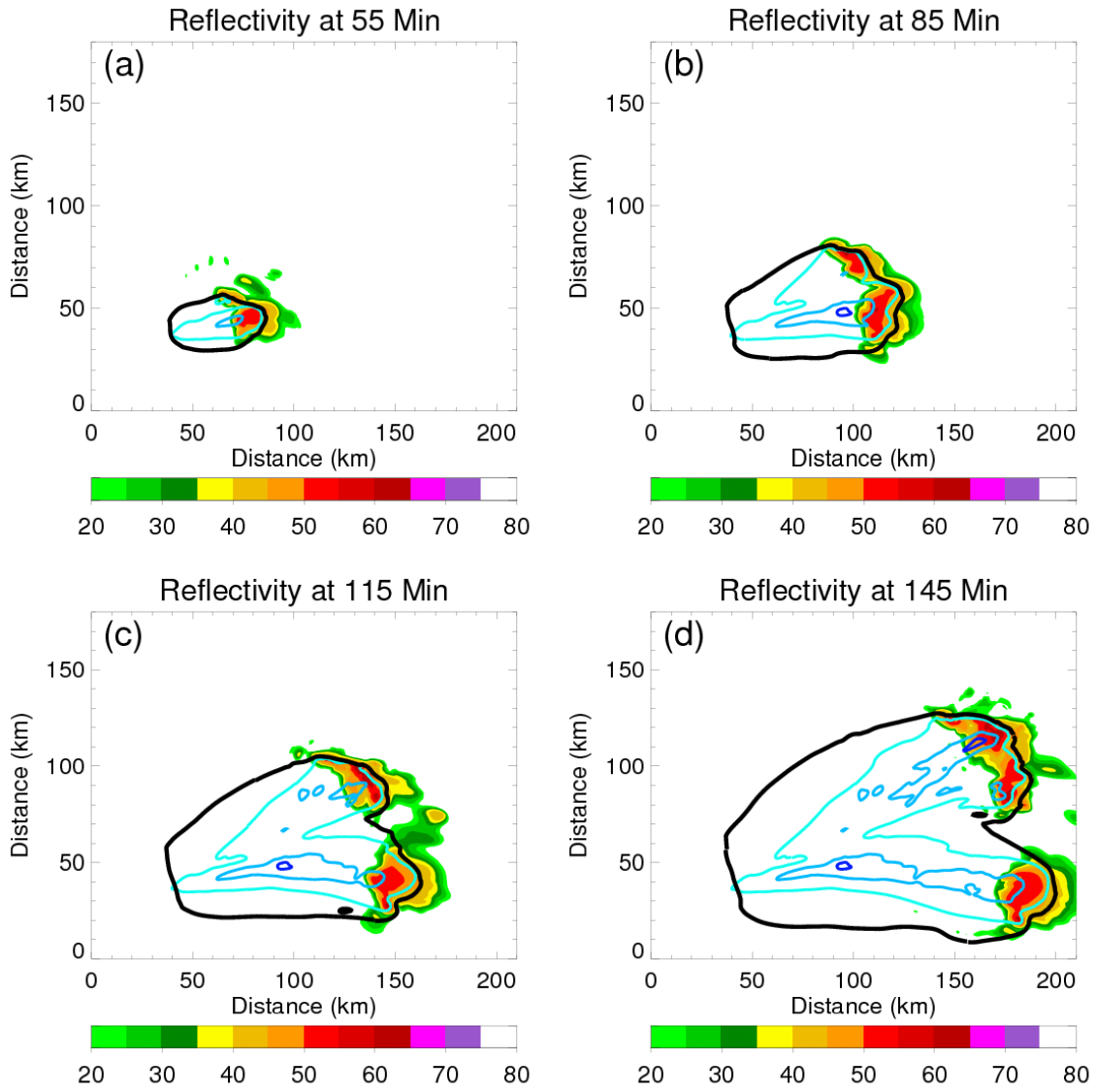

Figure 2.5. Evolution of the splitting supercell. Model derived reflectivity at 12 m AGL [shaded contours; following methodology of Matrosov (1999)], cold pool boundary [solid black contour; defined by -0.04 m^2 s^{-1} buoyancy following Tompkins (2001)], and total accumulated precipitation [1 mm (light blue), 10 mm (blue), and 20 mm (dark blue)] are shown at (a) 55 minutes, (b) 85 minutes, (c) 115 minutes, and (d) 145 minutes.

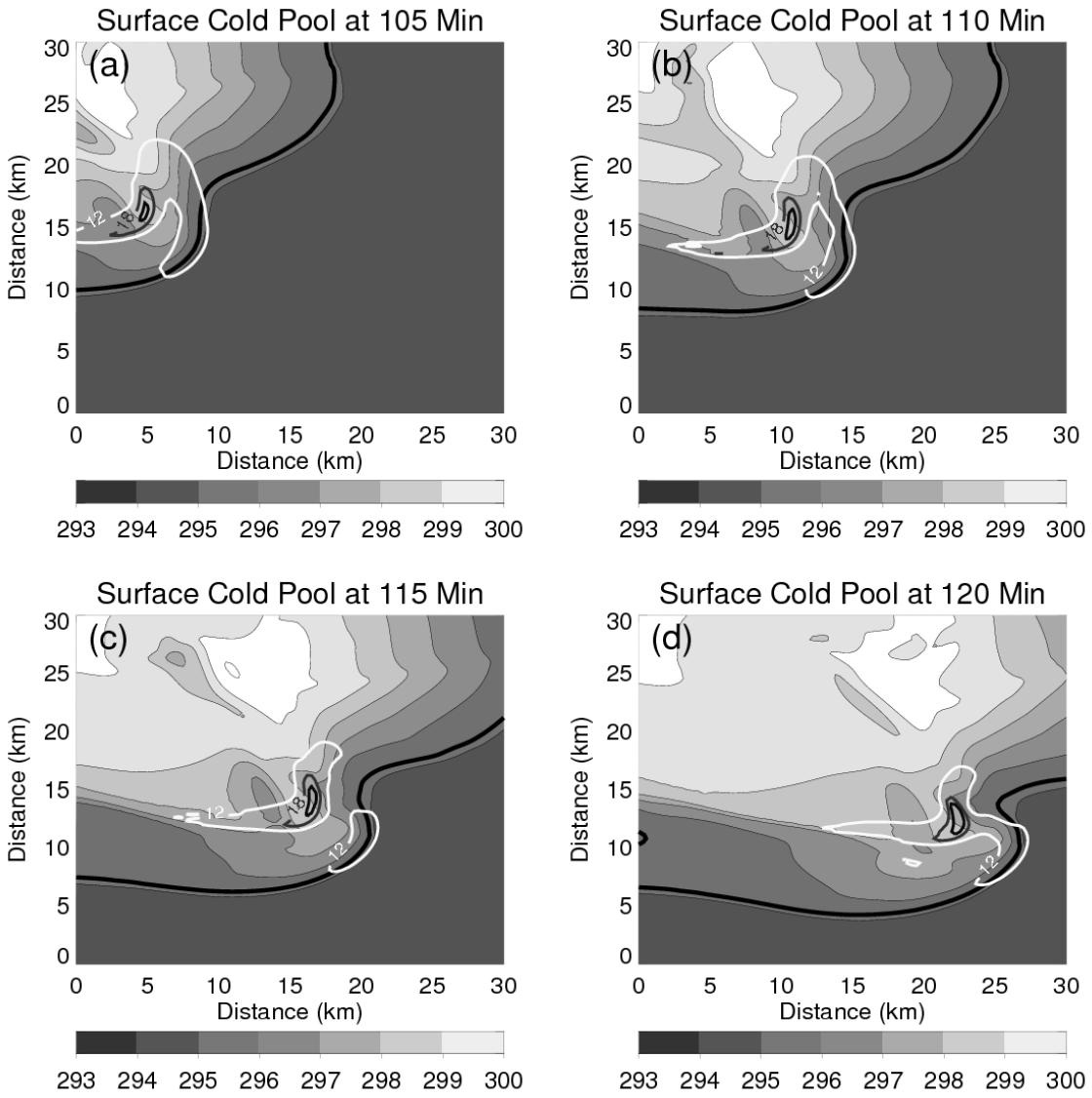

Figure 2.6. Cold pool evolution of the right moving supercell. Surface potential temperature (shaded contours), surface wind speed (12 m s^{-1} [white contour], 18 m s^{-1} [grey contour], 22 m s^{-1} [dark grey contour]), and cold pool boundary (thick black contour) are shown at (a) 105 minutes, (b) 110 minutes, (c) 115 minutes, and (d) 120 minutes.

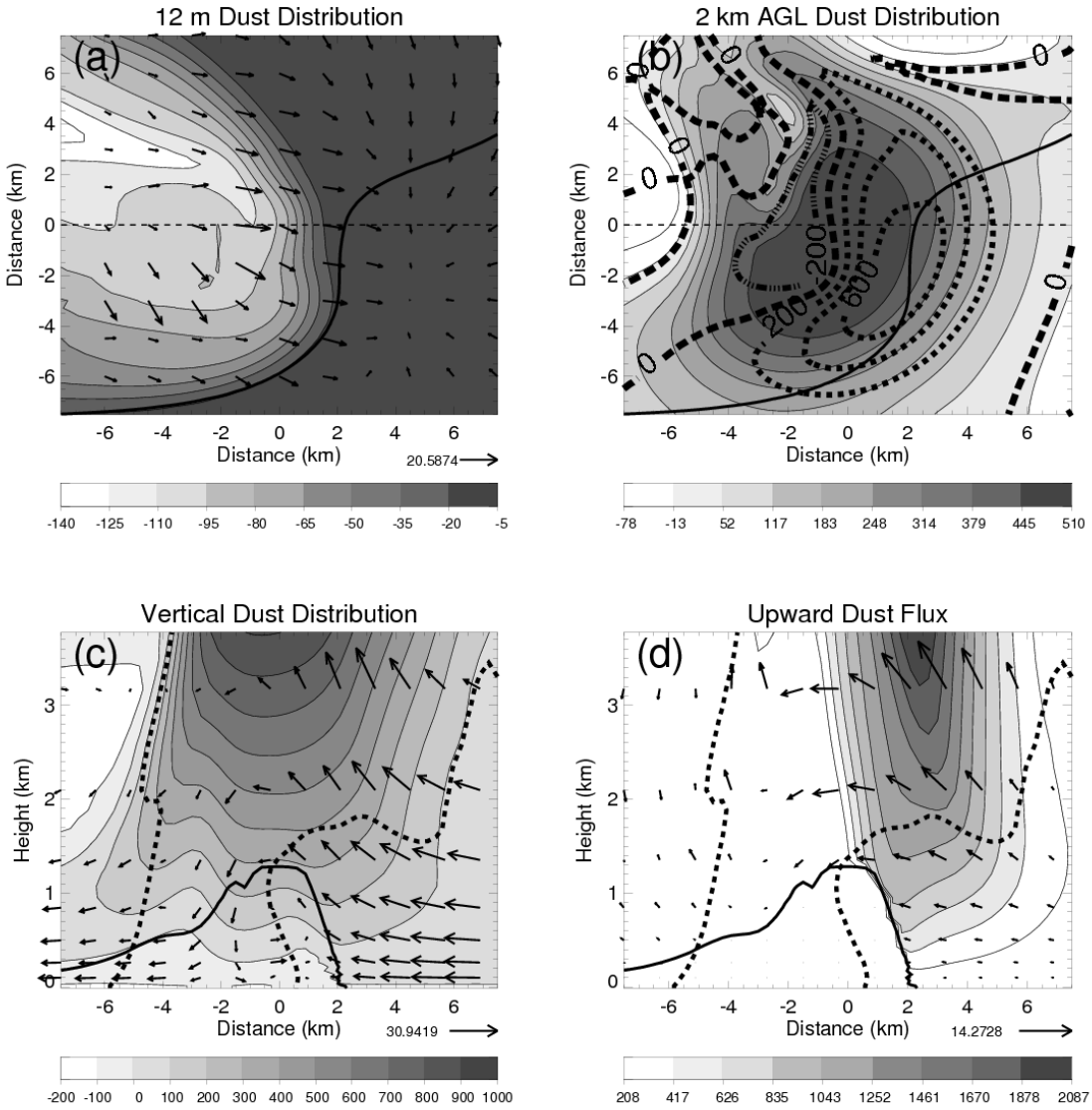

Figure 2.7. EXP-BACKGROUND at 105 minutes. (a): Surface dust concentration (cm^{-3}) relative to the initialized background profile (shaded contours), surface cold pool boundary (solid black contour), surface wind vectors, and cross section location (thin dashed black line) in (c). (b): 2 km AGL dust concentration (cm^{-3}) relative to the initialized background profile (shaded contours), surface cold pool boundary (solid black contour), vertical dust flux through the 2 km AGL surface (thick dashed line denotes the zero line; thin dashed lines denote positive fluxes; dash-dot lines denote negative fluxes in 10^3 cm^{-2} s^{-1} intervals), and cross section location (thin dashed black line) in (d). (c): vertical cross section at the location shown in panel (a) with dust concentration (cm^{-3}) relative to the initialized background profile (shaded contours), cold pool boundary (solid black contour), 0.5 g kg^{-1} total condensate (dotted contour), and storm-relative winds parallel to cross section plane. (d): same vertical cross section as (c) with upward dust flux (shaded contours in 10^3 cm^{-2} s^{-1}; downward dust flux not depicted), cold pool boundary (solid black contour), 0.5 g kg^{-1} total condensate (dotted contour), and horizontal dust flux through cross section plane (vectors in 10^3 cm^{-2} s^{-1}).

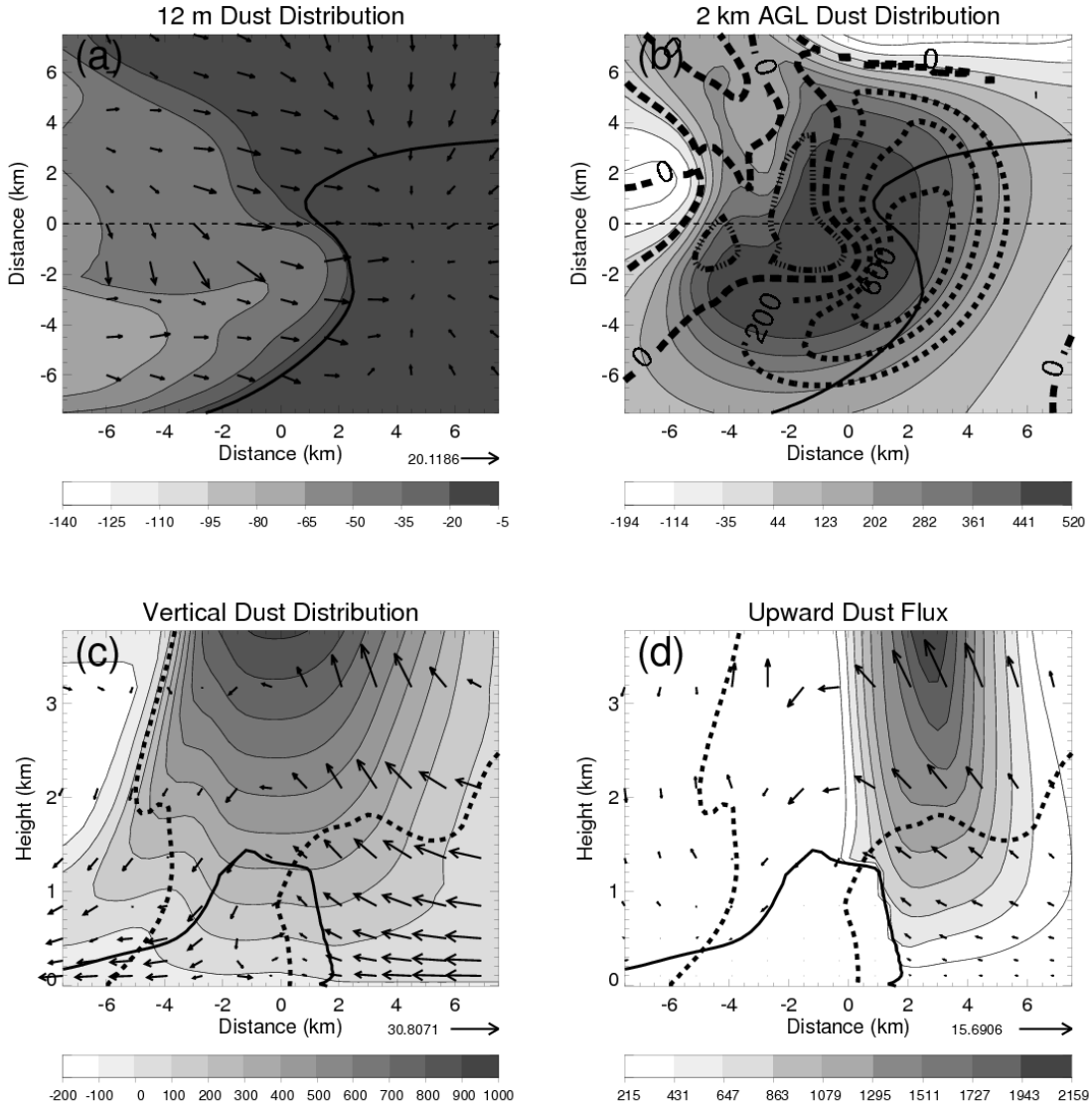

Figure 2.8. Same as Figure 2.7 except at 120 minutes.

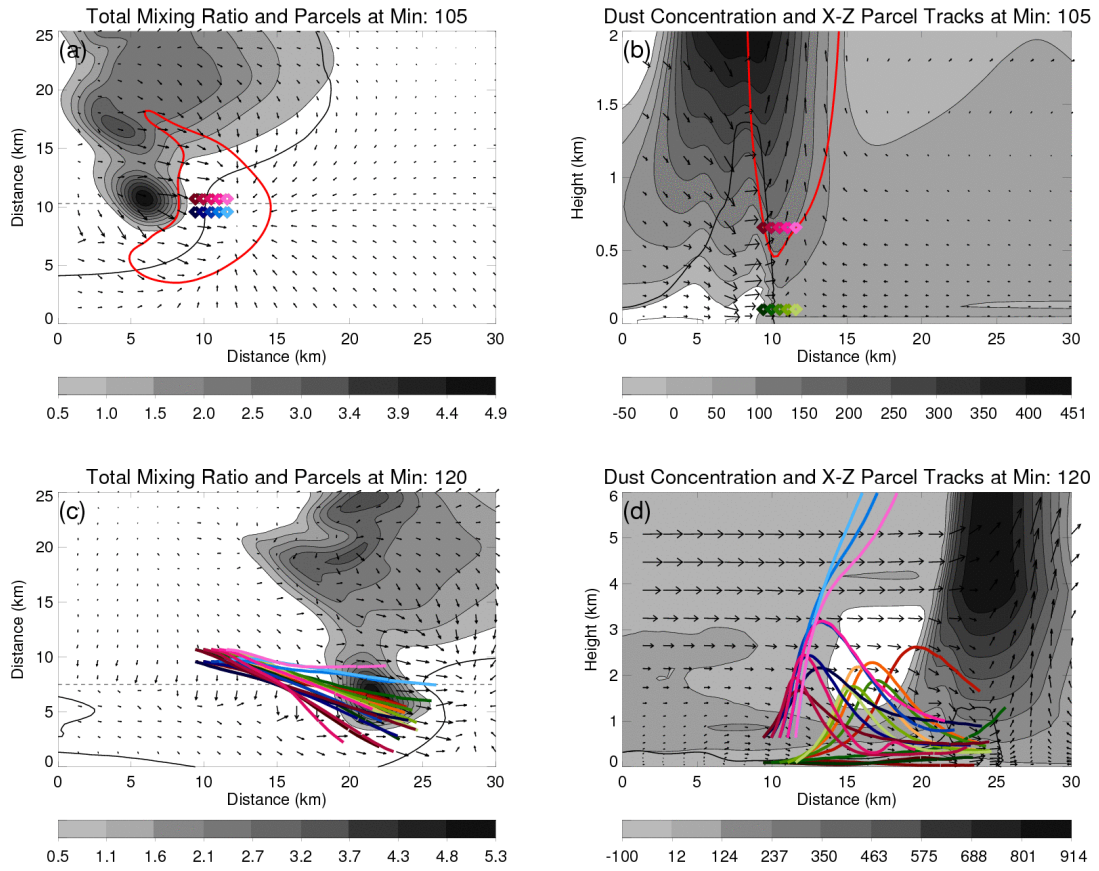

Figure 2.9. EXP-BACKGROUND parcel trajectories during the 15 minute period from 105-120 minutes. (a): At 105 minutes, total mixing ratio (shaded contours), surface cold pool boundary (solid black contour), surface wind vectors, 2 km AGL 5 m s^{-1} (red solid contour), and initialized parcel locations in the horizontal plane. Although hidden, 5 additional green parcels lie beneath the pink parcels and 5 additional orange parcels lie beneath the blue parcels. (b): At 105 minutes, dust concentration (cm^{-3}) relative to the initialized background profile (shaded contours), cold pool boundary (solid black contour), wind vectors parallel to vertical plane, 5 m s^{-1} updraft (solid red contour), and initialized parcel locations in the vertical plane. (c): At 120 minutes, total mixing ratio (shaded contours), surface cold pool boundary (solid black contour), surface wind vectors, and final parcel locations in the horizontal plane. (d): At 120 minutes, dust concentration (cm^{-3}) relative to the initialized background profile (shaded contours), cold pool boundary (solid black contour), wind vectors parallel to vertical plane, and final parcel locations in the vertical plane. For (c) and (d), parcel motions are from left to right.

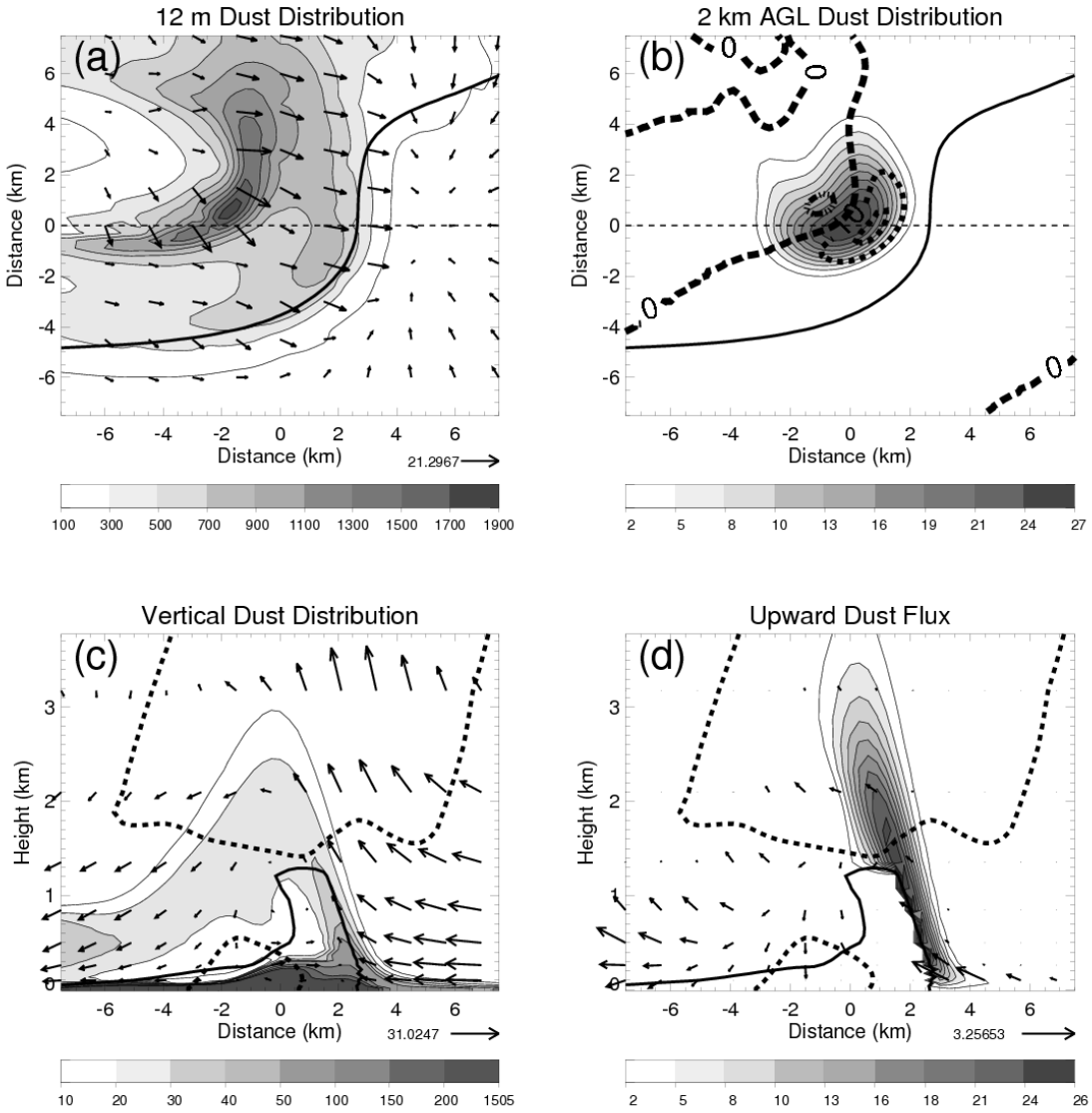

Figure 2.10. EXP-STORM at 105 minutes. All plots are identical to Figure 2.7, except dust concentrations are not relative to the background dust because no background dust was used in this simulation. Note: the last contour interval of dust concentration in (c) is from 200 cm^{-3} through the maximum value, as a small number of grid cells exhibit concentrations of this magnitude.

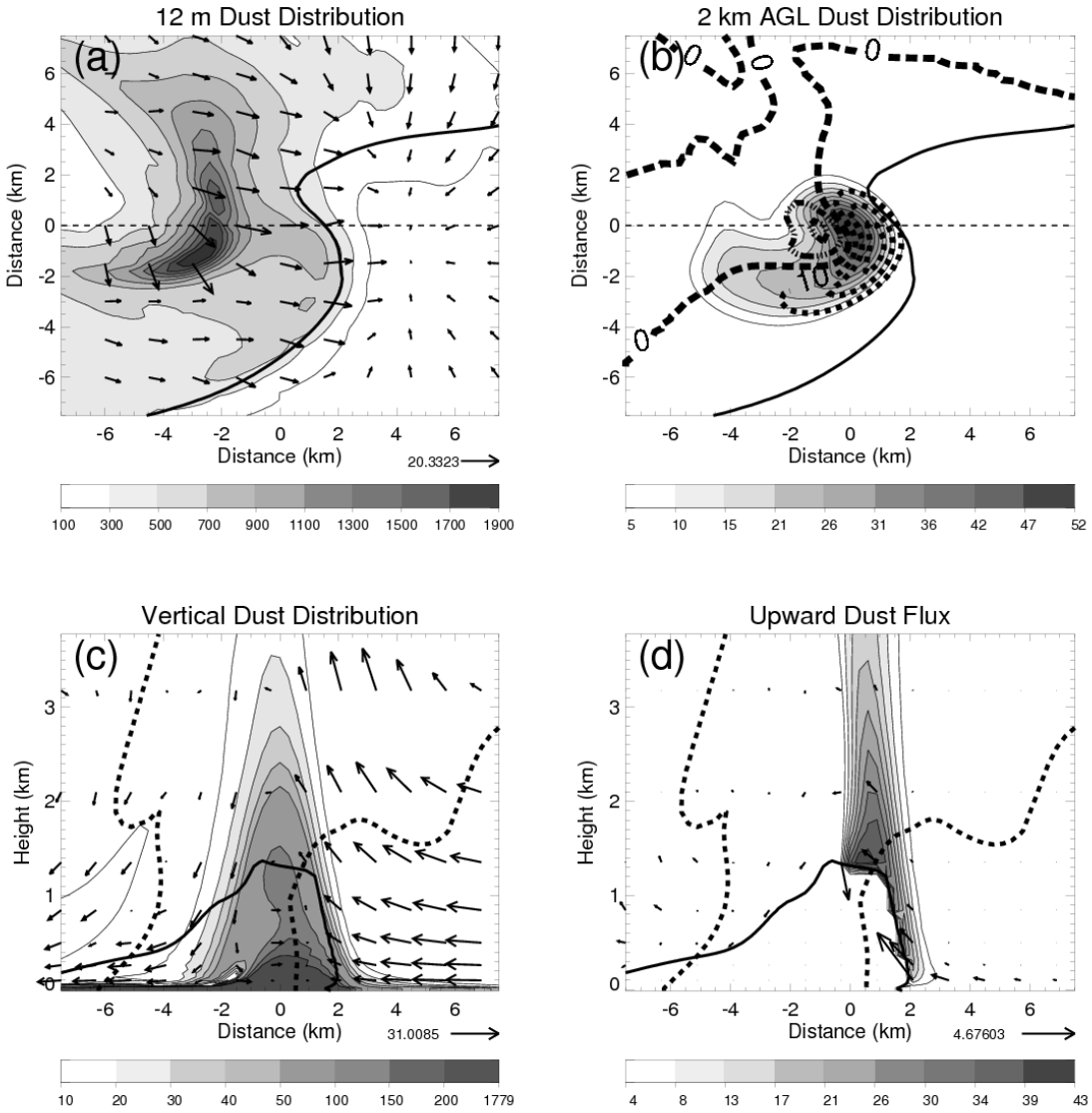

Figure 2.11. Same as Figure 2.10 except at 120 minutes.

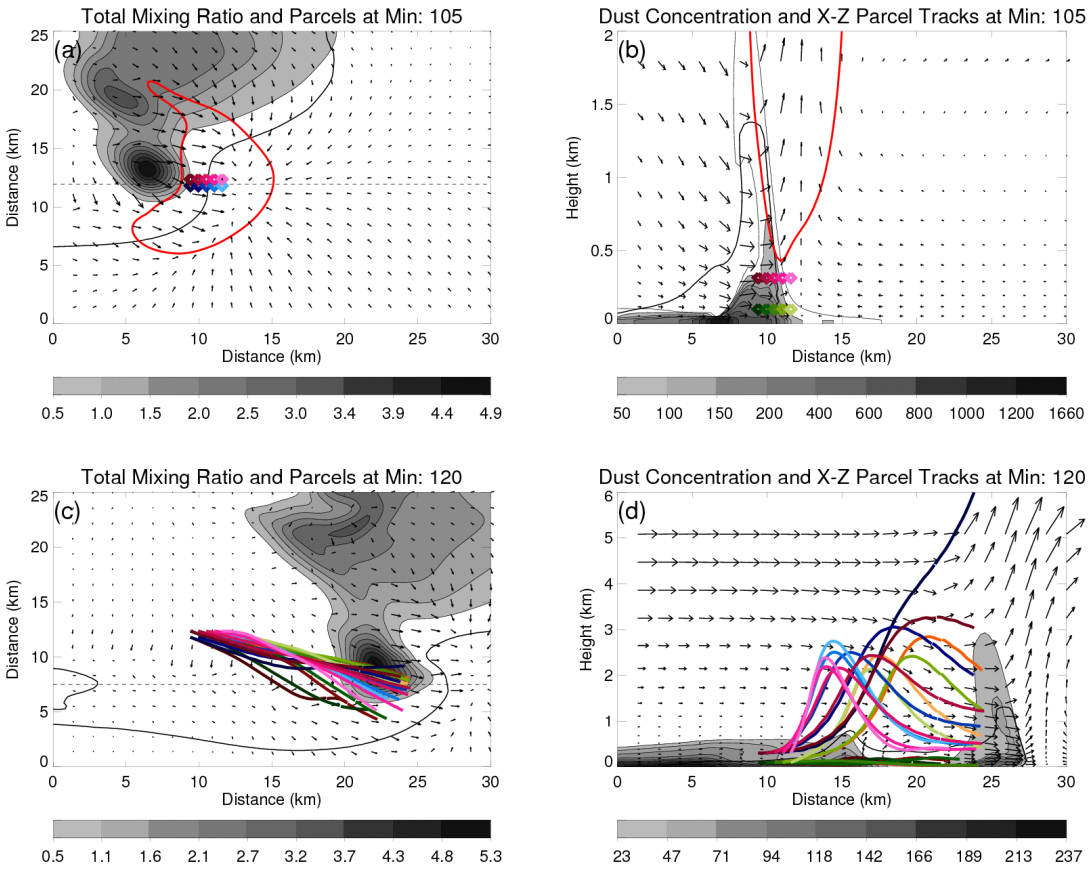

Figure 2.12. EXP-STORM with parcel trajectories during the 15-minute period from 105-120 minutes. Plots are the same as Figure 2.9.

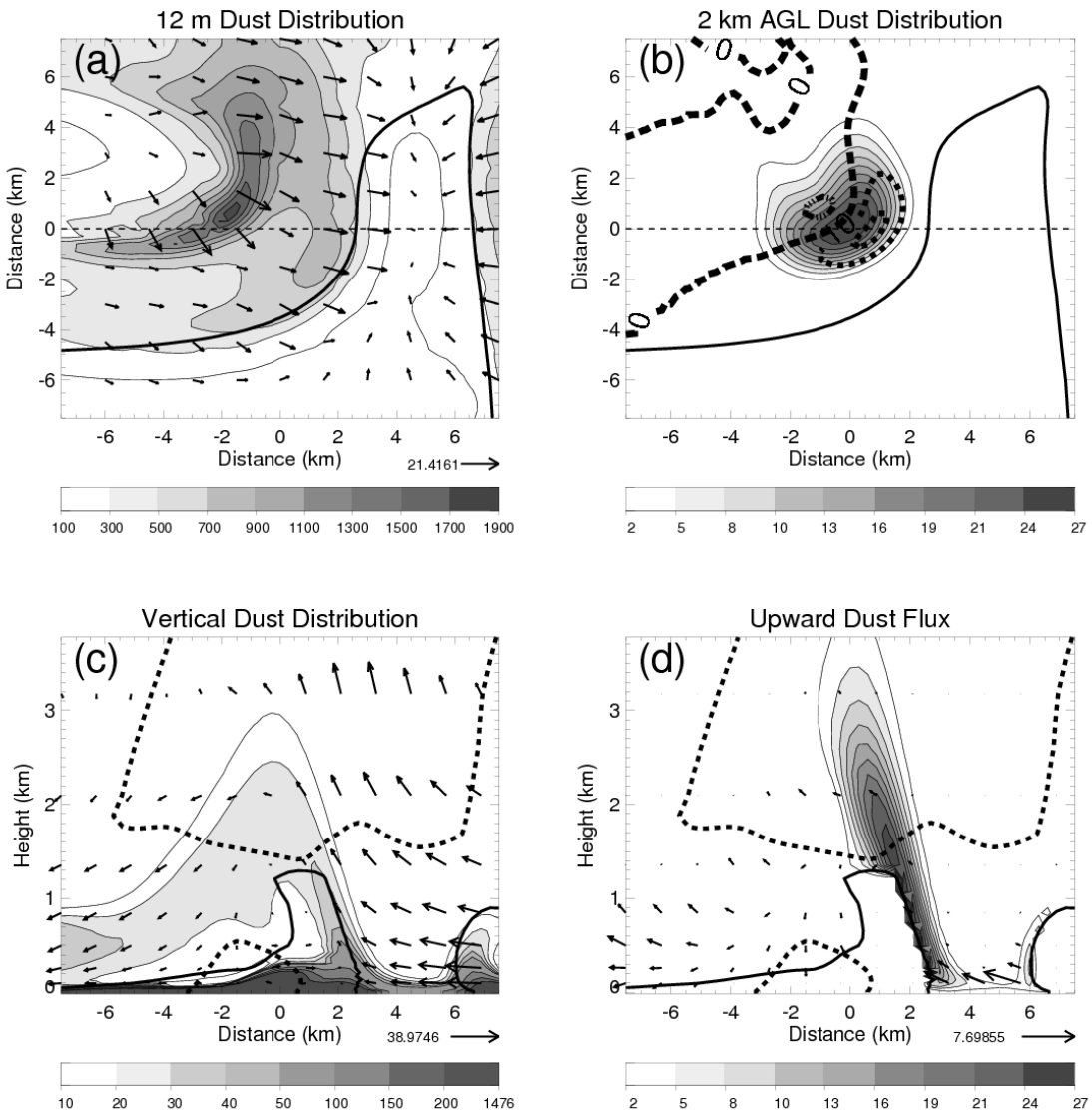

Figure 2.13. EXP-BOUNDARY at 105 minutes. Plots are the same as Figure 2.10.

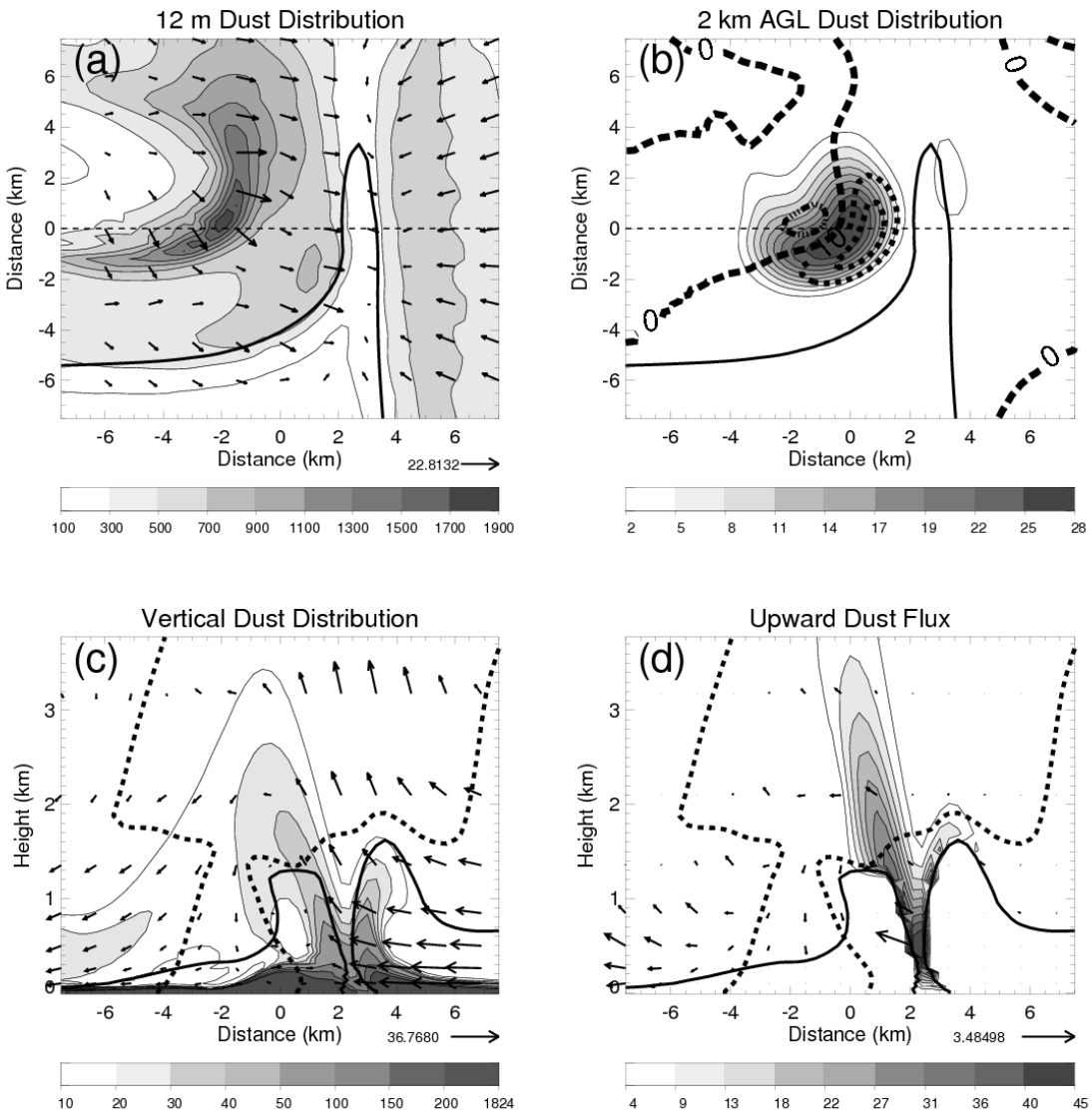

Figure 2.14. Same as Figure 2.13 except at 107 minutes.

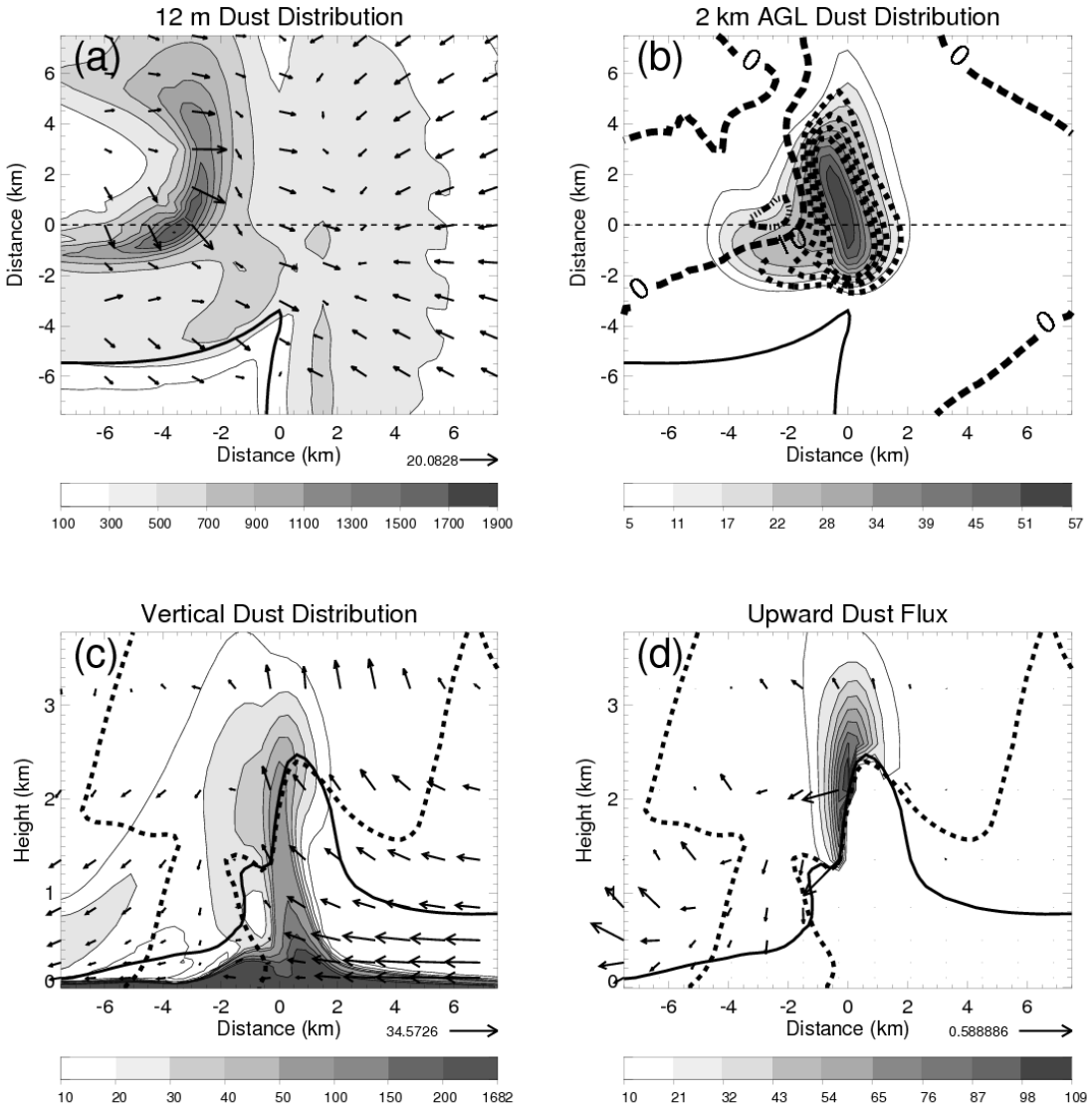

Figure 2.15. Same as Figure 2.13 except at 109 minutes.

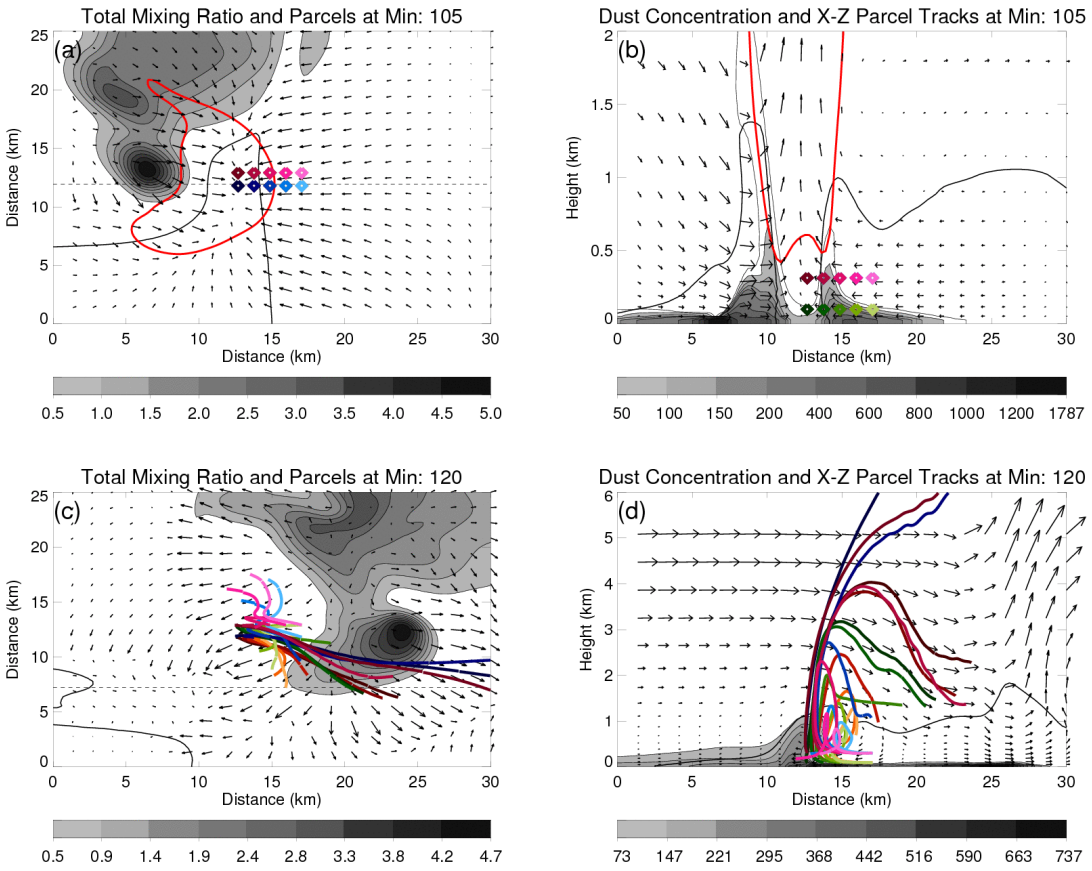

Figure 2.16. EXP-BOUNDARY with parcel trajectories during the 15 minute period from 105-120 minutes. Plots are the same as Figure 2.9.

Table 2.1: Mass and size distribution for soil used in dust emission scheme. Following Tegen and Fung (1994).

Size Interval	1	2	3	4	5	6	7
Radius(μm)	0.15	0.265	0.471	0.831	1.5	2.65	4.71
Mass Fraction	0.0009	0.0081	0.0234	0.0676	0.3	0.3	0.3

Table 2.2. RAMS configuration and options

Model aspect	Setting
• Grid	• Arakawa C grid (Mesinger and Arakawa 1976) • Single grid • Horizontal grid: $\Delta x = \Delta y = 300$ m • Vertical grid: Δz variable Δz (min) = 25 m Δz (stretch ratio) = 1.10 (10%) Δz (max) = 300 m • Model top: ~22 km • Seventeen levels below 1 km AGL
• Initialization	• Horizontally homogeneous • Idealized convective environment (Weismann and Klemp 1982) • Idealized wind profile (Weismann and Klemp 1984)
• Convective initiation	• 10 km wide, square bubble • 2 K thermal perturbation • 2 km depth
• Time step	• 1 s
• Simulation duration	• 3 hours
• Microphysics scheme	• Two-moment bulk microphysics (Saleeby and Cotton (2004); Meyers et al. 1997) • CCN background: 1600 (cm^{-3}) • IN background: 10,000 (kg^{-1})
• Boundary conditions	• Radiative lateral boundary (Klemp and Wilhelmson 1978a)
• Turbulence scheme	• Smagorinsky (1963) deformation-K closure scheme with stability modifications by Lilly (1962) and Hill (1974)
• Radiation scheme	• Harrington (1997)
• Surface scheme	• LEAF-3 (Walko et al. 2000)
• Dust scheme	• See Section 2a

Table 2.3: Mineral dust schemes used in each experiment.

Experiment Name	Model initialized with background dust	Surface emission	Dry deposition	Below-cloud scavenging
EXP-BACKGROUND	✓	X	✓	✓
EXP-STORM	X	✓	✓	✓
EXP-BOUNDARY	X	✓	✓	✓

CHAPTER 3: ASSESSING THE MINERAL DUST INDIRECT EFFECTS AND RADIATION IMPACTS ON A SIMULATED IDEALIZED NOCTURNAL SQUALL LINE

3.1. Introduction

Aerosol can effectively serve as cloud condensation nuclei (CCN), giant cloud condensation nuclei (GCCN), and ice nuclei (IN) such that changes in the concentrations of these nuclei impact the microstructure and radiation budget of clouds and precipitating convection (Twomey, 1974; Albrecht, 1989). This is often referred to as the aerosol indirect effect (AIE) and is one of the largest uncertainties in cloud radiative forcing of the climate system (Forster et al., 2007; IPCC, 2007). Because of this, considerable research efforts have been made to better understand aerosol indirect effects on clouds and precipitation using both observations (e.g. Borys et al., 1998; Ferek et al., 2000; Kaufman and Nakajima, 1993; Heymsfield and McFarquhar, 2001; Rosenfeld, 1999, 2000; Andrae et al., 2005; Roselfeld et al., 2008) and models (e.g. Khain et al., 2005; Seifert and Beheng, 2006; van den Heever et al., 2006, 2011; Lee et al., 2008; Storer et al., 2010; Igel et al., 2012; Morrison, 2012; Storer and van den Heever, 2012). However, results from these studies have indicated that aerosol indirect effects are highly variable, demonstrating the sensitive nature of this problem (Rosenfeld and Feingold 2003; Tao et al, 2012).

The original AIE theories (Twomey, 1974; Albrecht, 1989) were derived from studies of clouds that were comprised only of liquid water (i.e. warm clouds) – shallow cumulus and

stratocumulus. These AIEs have been shown to include a reduction in precipitation for warm cloud systems when aerosols act only as CCN (Borys et al., 1998; Ferek et al., 2000; Kaufman and Nakajima, 1993; Rosenfeld, 2000; Heymsfield and McFarquhar, 2001). However, when aerosols are large enough to act as GCCN, the precipitation effects due to increased aerosol have been shown to reverse for warm clouds in polluted environments. For example, Feingold et al. (1999), Cheng et al. (2009), and Solomos et al. (2011) all found that when high concentrations of both CCN and GCCN were present, precipitation increased. Once clouds reach temperatures that allow for ice processes to become important, the AIE becomes increasingly complex as more microphysical processes are involved, and the impacts of aerosols acting as IN need to be considered. Because it is difficult to quantify the AIE of mixed-phase cloud systems observationally (Rosenfeld and Feingold, 2003; Matsui et al., 2004; Berg et al., 2008), numerous modeling studies have been performed to enhance our understanding of such effects (Khain et al., 2005; van den Heever et al., 2006, 2011; van den Heever and Cotton, 2007; Lee et al., 2008; Storer et al., 2010; Solomos et al., 2011; Igel et al., 2012; Morrison, 2012; Storer and van den Heever, 2012). However, results from these studies have varied both in terms of convective invigoration and precipitation, which could be due to a number of factors (Morrison, 2012; Tao et al., 2012).

Despite the range in results that have been found for mixed-phase convective systems, a common factor amongst many of the modeling studies is that aerosols are typically represented as only one type of nucleating aerosol (Khain et al., 2005; van den Heever et al., 2011; Lee et al., 2008; Storer et al., 2010; Igel et al., 2012; Morrison, 2012; Storer and van den Heever, 2012). However, arguably the most abundant aerosol in our atmosphere, mineral dust (IPCC, 2001), has been found to act as CCN, GCCN, and IN (Twohy et al., 2009; DeMott et al., 2010), thereby

potentially complicating the response. For example, van den Heever (2006) and van den Heever and Cotton (2007) both found that for continental deep convection, AIEs are highly variable and can change sign depending on the aerosol type involved.

While mineral dust is shown to have the highest concentrations close to its sources [desert regions] (Tegen and Fung, 1994), it has been observed to traverse the globe over vast distances (e.g. the Saharan Air Layer [SAL]) thereby impacting a variety of convective systems (Prospero, 1996,1999; Perry et al., 1997; Sassen et al., 2003; van den Heever et al. 2006; Carrio et al., 2007; Bangert et al., 2012). One such system, which has been found to be the leading heavy-rain producer in the tropics and subtropics (Nesbitt et al., 2006), is the mesoscale convective system (MCS). While a number of studies have investigated AIEs on MCSs (Lynn et al., 2005a,b; Wang, 2005; Lee et al., 2008a,b, 2009a; Li et al., 2009), little investigation regarding the specific impacts of mineral dust on MCSs has been performed. This is surprising considering the high frequency of MCS occurrence near the primary dust source regions of the world (Nesbitt et al., 2006).

The primary goal of this study is to assess the aerosol indirect effects of mineral dust on squall lines. As with previous studies of the microphysical impacts on squall lines (Morrison et al. 2009; Bryan and Morrison 2012; Morrison et al. 2012; Seigel and van den Heever, 2012b; van Weverberg et al. 2012) these goals will be achieved through idealized numerical modeling. In order to better our understanding of the mineral dust AIE, recent model developments have been made to the microphysics and aerosol schemes in the model used in this study, the Regional Atmospheric Modeling System (RAMS). These now allow mineral dust particles to nucleate as both cloud drops and ice crystals (including immersion freezing), replenish upon evaporation and sublimation, be tracked throughout hydrometeor transition, and be scavenged by precipitation

and dry sedimentation. This approach offers an excellent framework to explore in detail, the microphysical and radiative processes responsible for the AIEs of a mixed-phase cloud system, such as the squall line.

The role of radiation in squall line development and characteristics has been studied fairly extensively, the results of which indicate that radiation generally acts to strengthen squall lines due to increased instability from longwave cooling (Chen and Cotton, 1988; Dudhia, 1989; Tao et al., 1991,1993; Chin, 1994; Dharssi et al., 1997). However, the role that radiation plays in squall lines due to *changes* in microphysical processes arising from the presence of aerosols is not well understood. Therefore, in order to isolate this role, as well as mineral dust AIEs on squall lines, a suite of idealized cloud resolving model simulations is performed. The analysis of these simulations utilize the technique of factor separation (Stein and Alpert, 1993; Alpert et al., 1995; Homar et al., 2003; van den Heever et al., 2006; Alpert and Coauthors, 2011) to isolate the individual responses in the squall line that (1) arise from radiation, (2) from dust altering the microphysics, as well as (3) from the synergistic effects between (1) and (2). The following section will describe in detail the new microphysical model developments for representing mineral dust, along with an introduction to factor separation and its use in this study. Section 3 will present the results of the simulations and Section 4 will provide a discussion and summary of the work herein.

3.2. Methods

Four numerical simulations of an idealized squall line have been performed to assess the AIE of mineral dust. In order to obtain a realistic representation of mineral dust within the cloud-resolving model (CRM) used for this study, modifications have been made to its microphysical scheme, the details of which are briefly described in this section following a short model description. Subsequently, the experimental design is presented.

3.2.1 Model description

Given that the AIE stems from aerosols modulating microphysical processes within clouds, it is important to use a model that best simulates the microphysical processes observed in reality. This has been demonstrated to be most accurate when using bin-resolved microphysics (Khain et al., 2000; Morrison and Grabowski, 2007), however the use of such schemes on scales that are required to simulate a three dimensional squall line (i.e. ~ 500 km) are too computationally expensive with our current computing technology. As such, a model that is appropriate to simulate both the microphysics and the dynamics of a squall line is the non-hydrostatic Regional Atmospheric Modeling System (RAMS; Pielke et al. 1992; Cotton et al. 2003; Saleeby and Cotton 2004). RAMS has a sophisticated bin-emulating two-moment bulk microphysical parameterization scheme that prognoses mass mixing ratio and number concentration for eight hydrometeor species [cloud droplets, drizzle, rain, pristine ice, snow,

aggregates, graupel, and hail] (Walko et al., 1995; Meyers et al., 1997; Cotton et al. 2003; Saleeby and Cotton 2004). The representation of numerous hydrometeor species that all conform to a generalized gamma distribution (Flatau et al. 1989; Verlinde et al. 1990) helps to resemble the continuous spectrum of hydrometeors within the atmosphere.

In order to gain bin representation of various processes while maintaining computational efficiency, RAMS utilizes look-up tables that have been previously generated offline. These include hydrometeor sedimentation (Feingold et al. 1998), liquid-to-liquid, liquid-to-ice, and ice-to-liquid collisions (Feingold et al., 1988), and cloud droplet nucleation from aerosol within a detailed bin-resolving parcel model (Feingold and Heymsield, 1992; Saleeby and Cotton, 2004; Saleeby et al., 2012). Other schemes used in these simulations are radiative lateral boundary conditions (Klemp and Wilhelmson 1978), a Rayleigh damping layer within the top six levels of the model domain with modifications by Lilly (1962) and Hill (1974), the Smagorinsky (1963) turbulence closure scheme, and Harrington (1997) two-strean radiation.

3.2.2 Mineral dust scheme

In RAMS, four aerosol species (ammonium sulfate, sodium chloride, mineral dust, and "regeneration") are represented. Mineral dust is unique in that the particles are predominantly insoluble and they often have large diameters, which helps to allow them to behave as CCN, GCCN, and IN (Twohy et al., 2009; DeMott et al., 2010). As such, care has been taken in the representation of mineral dust within RAMS to ensure that it behaves similarly to what is seen in reality. As described in detail by Saleeby and van den Heever (2012), the mineral dust scheme

includes parameterizations for surface dust emission from wind and saltation, dry deposition, and wet scavenging by precipitation and nucleation.

Mineral dust is represented as two separate distributions; one small and one large mode, the details of which are described in the next subsection. For nucleation scavenging, the largest particles from the distribution are nucleated first and until supersaturation has been sufficiently reduced to halt nucleation (as is done with the other species). If a dust particle acts as a CCN that is less than or equal to 1μm, then a cloud droplet is formed that contains a dust particle. Similarly, if a dust particle is larger than 1μm the nucleated drop starts off as drizzle drop due to its large size; it also contains a dust particle. Because mineral dust is largely insoluble, the majority of the aerosol mass remains within the droplet in solid form and is then tracked through the various transitions between hydrometeor species. The insoluble mass within a drop is allowed to aid ice nucleation above the freezing level due to immersion freezing, which has shown to be an important ice nucleation mechanism (de Boer et al., 2010). Additionally, dry dust particles that have diameters greater than 0.5μm are allowed to serve as IN, so long as the limit of activated IN at the respective temperature has not been reached (DeMott et al., 2010). All heterogeneous nucleation of ice occurs following the parameterization of DeMott et al. (2010).

If a liquid drop or an ice crystal containing dust evaporates or sublimates, the dust mass is then added to the regenerated aerosol species. Due to the complicated nature of this aerosol regenerative process, assumptions have been made regarding the aerosol characteristics, as multiple aerosol species could be present in any drop. Saleeby and van den Heever (2012) provides a thorough description of the microphysical and aerosol schemes.

3.2.3 Experimental design

In this study, four idealized simulations are performed of a nocturnal squall line to investigate its response to the addition of mineral dust. All simulations are performed in three dimensions with a constant horizontal grid spacing of 500 m and a stretched vertical grid from 50 m to 500 m. The model domain covers a volume of 500 x 150 x 26 km in the zonal, meridional, and vertical directions, respectively. The time step used is 3 s and time integration is performed for 7 hours nocturnally, as this is the peak occurence time of MCSs (Laing and Fritsch 1997; Anderson and Arritt 1998; Jirak et al. 2003).

Squall line initiation is performed from a similar framework as other previous idealized studies (Trier et al. 1997; Fierro et al. 2008; Morrison et al. 2009; Seigel and van den Heever, 2012b). The model domain is initialized with horizontally homogenous temperature and moisture profiles following Weisman and Klemp (1982), but with a boundary layer temperature profile that has been adjusted to mimic a well-mixed boundary layer, which better represents reality (Figure 1). The shear profile used for initialization has a linear increase from 0 to 12.5 m s^{-1} in the lower 2.5 km (Figure 1) and is within the range used by previous studies (Weisman 1992,1993; Weisman and Rotunno 2004; Frame and Markowski 2006; Bryan et al. 2007). The squall lines are initiated using a 4 km deep, -6 K line thermal resting on the surface, representing a cold pool, and contains random embedded $-0.1 \leq \theta \leq 0.1$ potential temperature (θ) perturbations to initiate three-dimensional motions.

Aerosol data near one of the largest dust source regions in the world, the Sahara, is used to represent the nucleating species of sulfates and mineral dust within RAMS. These data have

been collected from the NASA African Monsoon Multidisciplinary Analyses (NAMMA) experiment in 2006 (personal communication with Cynthia Twohy), and are a good sampling of the SAL (DeMott et al., 2003). Figure 2 shows the vertical profiles and distributions (number and mass) of the aerosol concentrations for sulfate, small dust, and large dust particles. The treatment of dust for each simulation is described later in this subsection.

In order to more fully understand how mineral dust impacts the simulated squall line, factor separation (Stein and Alpert, 1993) is used to isolate the contributions from: (1) the inclusion of radiative transfer, while excluding mineral dust (herein referred to as RADIATION), (2) dust altering microphysical processes but not the subsequent radiative responses (herein referred to as DUST MICRO), and (3) the nonlinear interactions *between* dust altering microphysical processes and radiative transfer (herein referred to as SYNERGY). Factor separation has been shown to be an effective technique in other previous studies of deep convection (Romero et al., 1998; Homar et al., 2003; van den Heever et al., 2006). It is important to stress that SYNERGY is not merely the sum of RADIATION and DUST MICRO, but rather it is an additional contribution that is purely due to the nonlinear interactions between the two forcing mechanisms.

Let us consider a simple, hypothetical example that demonstrates a single synergistic contribution from a framework similar to the research herein. It is well known that dust acts as IN and that anvil clouds radiatively cool near cloud top due to longwave emission by condensate, mainly in the form of ice. From this, it could be expected that the sole inclusion of radiative transfer in a nocturnal squall line simulation (i.e. RADIATION) would act to cool the anvil, thereby increasing supersaturation and facilitating ice crystal growth. Similarly, it could be expected that the impacts of the sole inclusion of dust (i.e. DUST MICRO) on the anvil would

act to increase ice crystal number concentrations and subsequently alter the ice crystal size distributions and microphysical processes within the anvil. Now, the synergistic contribution from radiative transfer *and* dust (i.e. SYNERGY) within the anvil is more complex, as nonlinear interactions often occur. For example, because radiative cooling enhances supersaturation in the anvil, the additional cooling may help to nucleate more dust particles relative to the situation in which only the inclusion of dust is considered. The additional ice crystals produced through this synergistic response may then act to further enhance cloud top cooling over and above from that produced in RADIATION due to increases in ice crystal surface area and number concentration. This hypothetical example represents one possible nonlinear interaction that may result from the sensitivity experiments herein.

In order to fully quantify the three previously discussed contributions to the squall line (RADIATION, DUST MICRO, and SYNERGY), four sensitivity experiments are conducted in which the inclusion of radiation and microphysically active dust are systematically toggled. The description and name of each simulation is shown in Table 1, where the following information further describes the experiments:

- when dust is microphysically active, the full dust scheme is used and includes dust nucleating as liquid drops and ice crystals, dry deposition, and precipitation scavenging;
- when dust is not microphysically active, then dry deposition and precipitation scavenging are the only dust removal mechanisms;
- when radiation is turned off, the tendencies to the temperature field from radiative processes are not included; furthermore, radiation is not allowed to interact with the microphysics.

In order to most effectively isolate the AIE using factor separation on the four simulations, dynamic surface interaction is excluded for all simulations and is replaced by fixed values of surface temperature (300 K) and soil moisture (35% volumetric content). Additionally, as the focus of the study is on aerosol indirect effects and not aerosol direct effects, *dust and sulfates are not radiatively active for all simulations*. A constant roughness length of 0.05 is used to simulate the effects of surface friction over grass and brush, which is a common land surface for MCSs in semi-arid regions (Masson et al., 2003). Coriolis forcing is also excluded for all experiments to keep the squall line flow predominantly perpendicular to the meridionally oriented cold pool for more straightforward analysis.

The calculations used to isolate the factors described above are shown in Table 2, along with the naming convention that is used throughout the remaining sections. The term "the factor(s)" refers to the contributions to the squall line from the calculations of RADIATION, DUST MICRO, and SYNERGY (Table 2), and *not* the simulations of dOffrOff, dOnrOff, dOffrOn, and dOnrOn (Table 1). These calculations are applied to the group of simulations in a variety of ways (e.g. domain averaged fields, cloudy region averages, etc.) and will be described with respect to each analysis type.

3.3. Results

This section presents results from factor separation analyses of four simulations of an idealized nocturnal squall line. In order to provide a controlled set up of the experiment, a single squall line simulation was used as the benchmark squall line for the sensitivity experiments. This

benchmark simulation is run for two hours and includes the full dust scheme and the effects of radiation. After two hours, the squall line has matured and the model is restarted using those data as the initial conditions for each of the four sensitivity experiments: dOffrOff, dOnrOff, dOffrOn, and dOnrOn (Table 1). For those analyses in this section that utilize time averaging, the first hour of each sensitivity experiment has been excluded in order to provide sufficient time for the squall line physics to evolve from the benchmark simulation. Furthermore, some of the analyses provided in this section are susceptible to local "shifts" of microphysical processes. Because of these shifts, zonally averaged values are also provided and discussed in order to obtain bulk assessments of the presented analyses. The results in this section are compartmentalized into two subsections that first describe the changes in the general characteristics and dynamics of the squall line due to the factors, and then describe the microphysics and thermodynamics responsible for those changes.

3.3.1 General characteristics and dynamics

The four squall line evolutions are consistent and characterized as a classic trailing stratiform squall line (Parker and Johnson, 2000). Figure 3 shows 1 km AGL simulated radar reflectivity (Matrosov, 1999) and surface winds for the squall lines after one, three, and five hours into each simulation. It can be seen that all four squall lines have a leading line of high reflectivity that is trailed by a ~ 100 km wide region of lower reflectivity, consistent with the categorization of MCS's (Houze, 1993; Parker and Johnson, 2000). It can also be seen that the squall lines that include microphysically active dust (dOnrOff and dOnrOn) begin with stronger

reflectivity values leading the convective line, but at the end of time integration, the two squall lines appear to be breaking up and weakening (compare Fig. 3c,f with Fig. 3i,l).

To begin the assessment of squall line intensity, Figure 4 shows the contributions to precipitation from the factors as meridionally averaged Hovmöller diagrams, along with the full precipitation field of the CONTROL simulation (dOffrOff). The CONTROL simulation exhibits the classic characteristics of accumulated precipitation for a trailing stratiform squall line, where (1) a narrow region of enhanced precipitation occurs at the leading edge due to warm-rain formation, and (2) a precipitation minimum occurs behind the convective line (often referred to as the transition zone) that is followed by another local maximum in precipitation from ice processes (Fig. 4a). Including the effects of radiation (RADIATION; Fig. 4b) acts to increase precipitation for the entire squall line on average by up to 25%, consistent with other studies (Tao et al., 1991,1993; Dharssi et al., 1997). The inclusion of microphysically active dust (DUST MICRO) contributes to the precipitation field in three ways (Fig. 4c): (1) it initially enhances convective precipitation (up through the first 2.5 hours); (2) it systematically decreases the stratiform precipitation; and (3) it reduces the domain mean precipitation during the second half of the experiment by up to 30%. Furthermore, the synergistic contribution to precipitation from microphysically active dust and radiation (SYNERGY; Fig. 4d) is not overall very large, and is characterized by a brief increase in precipitation between hours two and three followed by a decrease towards the end of time integration by up to 15%.

The cold pool has been shown to play an integral role in the organization and structure of squall lines (Thorpe et al., 1982; Rotunno et al., 1988, 1990; Weisman et al., 1988; Weisman, 1992, 1993; Weisman and Rotunno, 2004, 2005; Bryan et al., 2006). To assess each factor's contribution to the cold pool speed of the squall line, a traditional measure of cold pool speed is

used (e.g. Rotunno et al., 1988; Weisman and Rotunno, 2004; Bryan et al. 2006) that is based on density current theory and is given by (Benjamin, 1968)

$$C_B^2 = 2\int_0^H (-B)dz, \tag{1}$$

where C_B represents the cold pool propagation speed based, H represents the depth of the cold pool, and B represents buoyancy, which is calculated following Tompkins (2001). The cold pool boundary is defined by the -0.05 m^2 s^{-2} buoyancy surface. The speed of the cold pool of CONTROL (Fig. 5a) ranges from ~15 – 23 m s^{-1}, and agrees well with other studies using the same thermodynamic profile as the squall line simulations here (e.g. Weisman and Rotunno, 2004; Bryan et al., 2006).

The factor separation analysis for cold pool speed shows perhaps unsurprisingly, a similar trend to precipitation for the contributions of RADIATION, DUST MICRO and SYNERGY (Fig. 5). On average, RADIATION generally does not contribute to a substantial change in cold pool speed until the final hour of the experiment, whereby an increase of up to 8% occurs (Fig. 5b). DUST MICRO acts to initially increase the cold pool speed for the first hour; and is then followed by a decrease in cold pool speed throughout the remainder of time integration (Fig. 5c). SYNERGY's contribution to cold pool speed is overall not large and contains a maximum change in C_B of ~5% (Fig. 5d). This small change in cold pool speed is largely due to the small changes in condensate due to SYNERGY, which will be discussed in greater detail in the next subsection.

It has been shown that cold pool intensity and precipitation of squall lines are both dependent on various microphysical processes (Morrison et al. 2009; Bryan and Morrison 2012;

Morrison et al. 2012; Adams-Selin et al., 2012; van Weverberg et al. 2012). As such, in order to obtain a bulk perspective of the microphysics governing the squall line, Figure 6 shows factor separation analyses of domain-averaged condensate paths and latent heating. The contributions to liquid water path (LWP) show consistent trends in time relative to CONTROL, whereby RADIATION increases LWP by up to 13%, DUST MICRO removes up to ~ 28% of LWP, and SYNERGY has an oscillatory and overall neutral contribution to LWP. With respect to ice processes, RADIATION shows a systematic increase in ice water path (IWP) in time; and at the end of experiment RADIATION contributes up to a 22% increase in IWP. An increase in squall line ice due to the inclusion of longwave radiation has also been seen by Tao et al. (1991, 1993), and will be further investigated later in this section. Both DUST MICRO and SYNERGY show a largely oscillatory response in contribution to IWP, except during the last hour where DUST MICRO dramatically reduces the IWP of the squall line, which is primarily due to the demise of the dOnrOff squall line from the significant weakening of the surface cold pool (Fig. 3i). The total water path (TWP) contributions from the factors indicate that RADIATION increases TWP (up to 14%), DUST MICRO reduces TWP (up to 28%), and SYNERGY again has an oscillatory contribution with small changes in time.

The changes in TWP will contribute to differences in latent heating (LH) that can alter the dynamics and intensity of the squall line. As such, a troposphere depth-normalized, vertically integrated LH rate is shown in Fig. 6d to gain a bulk perspective of LH. Similar to TWP, RADIATION invigorates the squall line latent heating and contributes to an enhancement of up to 26%. DUST MICRO has a neutral contribution to latent heating through the first 2.5 hours, as opposed to an expected negative contribution based on the decrease in TWP during this time. This discrepancy is explained by DUST MICRO's contribution to precipitation, where an

enhancement in the convective precipitation during the first 2.5 hours effectively removed the water from the squall line that already contributed to the total latent heating. The SYNERGY contributions to latent heating are relatively insignificant and have an oscillatory nature.

To better understand how the factors are contributing to the structure and organization of the squall line, Figure 7 shows vertical profiles of various temporally and domain averaged fields from cloud base (~ 1km AGL) up to just below the tropopause (~ 10 km AGL), which are expressed as percent contributions to the squall line. The zonal wind field (U; Fig. 7a) of CONTROL has the classic structure of a well-organized squall line that is contributing to convective momentum transport (CMT; Lane and Moncrieff, 2010). This can be seen by a local maximum in U ~ 3 km AGL due to the rear-to-front flow of the rear inflow jet (RIJ), and a local minimum in U within the anvil region ~ 7 km AGL due to the front-to-rear (FTR) flow of the squall line within the updraft. As such, a positive contribution to the RIJ or a negative contribution to the FTR flow enhances the mesoscale organization of the squall line. From Fig. 7a, it can be seen that RADIATION most positively contributes to the CMT of the squall line, which is consistent with other previous studies (Chen and Cotton, 1988; Dudhia, 1989; Chin, 1994; Dharssi et al., 1997). DUST MICRO significantly weakens the kinematic organizational structure of the squall line, which corroborates the demise of the dOnrOff squall line due to a weaker cold pool. While SYNERGY has thus far indicated no significant contribution to the squall line, it has a slightly positive contribution to the CMT of the squall line.

The mean vertical velocity (W; Fig. 7b) of CONTROL is positive everywhere and peaks in the middle troposphere. The contribution to W by RADIATION is generally positive throughout the depth of the troposphere, except near the top of the anvil where longwave cooling produces sinking motion. DUST MICRO negatively contributes to W up through 5 km AGL, but

positively contributes to W within the 5-9 km AGL layer, indicating that ice processes may be playing a large role. SYNERGY slightly increases the low-level W ~ 3 km AGL and slightly decreases W around 6 km AGL, which may highlight a change to convective organization of the squall line.

By sampling the squall line for grid cells that have strong updrafts and strong downdrafts, a more in-depth assessment of squall line invigoration and convective organization can be made. Fig. 7c shows the profile of total mass flux (MF), sampled where updrafts are greater than 2 m s^{-1} (i.e. convective mass flux, CMF). It is evident that RADIATION acts to enhance the CMF by up to 18%. DUST MICRO decreases the CMF substantially throughout the troposphere, while SYNERGY generally has a neutral contribution to CMF except near the freezing level where it increases CMF by up to 8% at ~ 4 km AGL. Conversely, by sampling the squall line where vertical velocity is less than -1 m s^{-1}, Fig. 7d shows the mean downdraft mass flux (DMF) profile that helps to both transport momentum towards the surface from aloft and enhance the cold pool (Smull and Houze, 1987; Weisman, 1992). Where the CONTROL mesoscale downdraft is maximized (2-4 km AGL), RADIATION positively contributes to DMF, DUST MICRO negatively contributes to DMF by up to 30%, and SYNERGY positively contributes to DMF. The contributions by the factors to both CMF and DMF match well with the contributions by the factors to the zonal wind, further confirming that DUST MICRO reduces CMT while SYNERGY enhances CMT. The reasons for these contributions are due to changes in microphysical processes and will be discussed in the next subsection.

From this subsection, the two factors involved with the mineral dust AIE on a nocturnal squall line, DUST MICRO and SYNERGY, act to weaken and slightly strengthen the squall line, respectively. Because the contributions due to SYNERGY are relatively small, the combined

contributions of DUST MICRO and SYNERGY lead to an overall weakening of the squall line in the presence of mineral dust. Conversely, the contribution of RADIATION is shown to invigorate the simulated squall line and matches well with past studies. The following subsection will explain in detail the microphysical processes responsible for the behavior of the factors (RADIATION, DUST MICRO, and SYNERGY) just discussed.

3.3.2 Microphysical response

Before analyzing the microphysical processes responsible for the behaviors of each factor just described, it is necessary to illustrate and describe how mineral dust is processed microphysically within the squall line. Figure 8 shows a meridionally and temporally averaged view of the dOnrOn squall line experiment. The microphysical processing of mineral dust acting as CCN by the squall line begins by nucleating cloud and drizzle drops in the inflow region of the squall line (Fig. 8a). The dust within cloud and drizzle (Fig. 8b) can then be tracked through the warm rain process as collision-coalescence generates raindrops (Fig. 8c). This process ultimately removes much of the dust through precipitation and may help to explain why DUST MICRO weakens the squall line due to a loss of potential IN. However, some dust remains within cloud, drizzle, and rain that can be followed to hail through riming processes near the freezing level within the updraft (Fig. 8d; Seigel and van den Heever, 2012b).

A second pathway of dust processing by the squall line occurs when dust acts as IN, and first occurs as pristine ice crystals nucleate near cloud top (Fig. 8e). Through vapor deposition, pristine ice grows into snowflake size crystals (Fig. 8f). As the snow containing dust settles

lower and resides longer in the anvil, ice crystal aggregation occurs because of increased probability of collection (Fig. 8g). The larger aggregates are transported rearward, while sedimentating towards the freezing level where increased riming by supercooled droplets can occur. This changes the dust-laden aggregates into graupel particles containing dust once sufficient riming has occurred (Fig. 8h). In the wake of the squall line surrounding the freezing level, a portion of the ice particles, snow, aggregates, graupel, and hail can sublimate, thereby releasing the dust particles back into the atmosphere as regenerated aerosol (Fig. 8i).

A factor separation analysis has been performed on each hydrometeor species' domain averaged path (i.e. a density-weighted, vertically-integrated mass) in order to gain insight into the microphysical processes responsible for the changes in dynamics discussed in the previous subsection. The contributions to each hydrometeor's mass by the factors are expressed as a percent change relative to CONTROL (Fig. 9). RADIATION increases the mass of all the hydrometeor types and adds 6% to the total condensate of the squall line. DUST MICRO negatively contributes to each hydrometeor species' mass with a total condensate contribution of -16%, which is predominantly due to the liquid species. SYNERGY's contribution is predominantly positive, however the total condensate contribution is small (less than 1%) and is mainly due to changes in ice mass.

As a first step in the understanding of why these changes in condensate are occurring due to radiative and microphysical impacts by the factors, Figure 10 shows a temporally- and meridionally- (following the gust front) averaged vertical cross section of the total condensate mixing ratio (TMIX) distribution within the squall line. Relative to CONTROL (Fig. 10a), it can be seen that the factors alter the TMIX distribution of the squall line in multiple ways. RADIATION increases TMIX throughout the depth of the troposphere (Fig. 10b). This is

maximized near cloud top (30% increase) due to cloud top radiational cooling (Fig. 11) that acts to destabilize the anvil region (Churchill and Houze, 1991), thereby promoting increased ice supersaturation that helps to grow condensate by vapor deposition. Additionally, a local maximum in TMIX enhancement occurs ~ 3 km AGL that appears to lead to heavier precipitation shaft. This matches well with the overall increase in precipitation (Fig. 4b) and cold pool intensity (Fig. 5b), indicating that enhanced precipitation production leads to increased evaporational cooling that drives a stronger cold pool and squall line.

Consistent with the individual contributions to hydrometeor mass, DUST MICRO decreases the zonally averaged total condensate throughout the depth of the troposphere. Locally, DUST MICRO increases TMIX near the gust front, decreases the trailing stratiform precipitation, and greatly reduces TMIX just below the freezing level in the wake of the cold pool-forced updraft (Fig. 10c). It is interesting that while an increase in condensate occurs near the gust front, the cold pool intensity weakens due to DUST MICRO. This further highlights the importance of the ice phase in maintaining cold pool intensity through melting and sub-cloud evaporation, as the precipitation originating from ice processes is reduced (~ -20-30 km from GF in Fig. 10c). The physics governing these responses in the squall line TMIX will be discussed in more detail later in this section.

For SYNERGY, while large positive and negative contributions occur locally, its average contribution to TMIX is relatively minor (Fig. 10d). However, there is a general increase in TMIX (1) just above the freezing level, which is due to an increase in hail mass (Fig. 9), and (2) near cloud top which is due to an increase in mass of the ice hydrometeor species that predominantly grow by vapor deposition, pristine ice, snow, and aggregates (Fig. 9).

The changes in TMIX from DUST MICRO are largely due to the increase in warm rain production (Fig. 12). As dust is ingested by the squall line near cloud base (Fig. 8a), which has been shown to be the dominant source region of aerosol ingestion (Tulet et al., 2010; Seigel and van den Heever, 2012a), nucleation of both cloud and drizzle drops occurs that broadens the total distribution of liquid drops. This helps to speed up the collision-coalescence process that generates rain-sized drops. This can be seen by the up to 50% increase in the cloud-to-rain process (CL2RT) just above the gust front (Fig. 12c). The rapid production of rain removes liquid from the squall line that could otherwise help to increase latent heating higher up in the updraft (notice 50% reduction in mean TMIX near the freezing level in Fig. 10c). SYNERGY also enhances CL2RT near the gust front and is due to the strengthening of the cold pool-forced updraft (~ 1-1.5 km AGL in Fig. 7c) that increases supersaturation, leading to increased nucleation of both large and small dust particles (discussed later) that promotes greater collision-coalescence (Fig. 12d). While CL2RT also increases for RADIATION (Fig. 12b), this is because the squall line (dOffrOn) overall is stronger (relative to dOffrOff) and has a faster updraft below the freezing level (Fig. 7c), which increases CL2RT due to both enhanced turbulence and increased condensation (discussed later).

The increase in CL2RT for DUST MICRO removes liquid from the squall line that had the potential to be lofted higher into the storm to aid ice processes. As such, a reduction in riming of hail (the species that incurs the most riming; RIMHT) is evident for DUST MICRO (Fig. 13c) in spatial collocation with those regions where significant riming occurs in CONTROL (Fig. 13a). Due to stronger 3-5 km AGL mid-level updrafts from SYNERGY (Fig. 7c), an increase in RIMHT occurs just above the freezing level (Fig. 13d). The change in RIMHT for SYNERGY near the freezing level also matches the local changes in TMIX (Fig. 10d), indicating that the

riming process is an important contributor to the increase in ice mass (Fig. 9). For RADIATION, riming is perhaps the most important microphysical process driving a stronger squall line. RADIATION dramatically increases RIMHT (Fig. 13b) throughout the depth of the mixed-phase region. This increase in riming is due to both an increase in liquid water (Fig. 9,10b) and the increase in updraft strength above the freezing level (Fig. 7c), which increases riming rates.

In order to better understand how these changes to the microphysics from the factors alter the vertical distribution of LH, which lead to changes in squall line dynamics (Fovell and Ogura, 1988; Tao et al., 1995; Bryan and Morrison, 2012; Seigel and van den Heever, 2012b), a factor separation analysis of the LH budget of the squall line is shown in Figure 14. RADIATION's contribution to the LH budget of the squall line is clear and matches well with the previous microphysical discussion (Fig. 14b). Radiative cooling near cloud top (Fig. 11) drives destabilization and increased ice supersaturation that helps to both nucleate more ice (ICE NUC) and grow more ice by vapor deposition (DEP) within the anvil at ~ 9-11 km AGL. The increase in ice condensate subsequently leads to an increase in melting (MELT), which helps to drive the stronger downdraft (Fig. 7d). This leads to a stronger cold pool (Fig. 5b) and stronger low-level updrafts (Fig. 7c) that increase supersaturation, resulting in a subsequent increase of condensation by up to 41%. The increase in liquid condensate (Fig. 9) forces an increase in the contribution of riming to LH by 13%. All of these microphysical processes act to strengthen the squall line.

Below the freezing level, DUST MICRO highlights the energetic ease of droplet growth versus droplet nucleation. First described by Squires and Twomey (1960), an increase in CCN assuming constant LWC results in a decrease in droplet size but an increase in droplet number, and is also seen here in dOnrOff and dOnrOn relative to dOffrOff and dOffrOn (comparison not

shown). As the change in droplet number occurs due to the addition of nucleating aerosol (dust), this increases the droplet surface area. Because the energy barrier to diffuse vapor onto an already present droplet is less than that to nucleate a dry aerosol (Prupacher and Klett, 1997), the process of vapor diffusion (COND) takes precedence over droplet nucleation (C+D NUC) on average. This effect has been noted by other aerosol modeling studies of aerosol impacts on deep convection (Storer and van den Heever, 2012; Sheffield et al., 2012) and is also seen for DUST MICRO, whereby the increase in C+D NUC below the freezing level is less than that of COND (Fig. 14c). However, the summation of the contribution by these two sources of LH from DUST NUC, which is maximized below the freezing level, positively contributes to the squall line by ~ 42%. This agrees well with many AIE studies that show increases in CCN lead to increases in droplet growth due to condensation (Khain et al. 2008; Lee et al. 2008b; Storer and van den Heever 2012).

Because mineral dust acts as IN, a 37% increase in ICE NUC is also evident near cloud top, however DUST MICRO's net contribution to vapor deposition (DEP) is a mere 2.83%. The reason why this contribution is not larger is due to the increase in warm rain (Fig 11) scouring available water vapor that could have been used to grow ice crystals. The increase in condensation that leads to the invigoration of warm rain precipitation (Fig. 12c) reduces riming by 28%, which has shown to be important for squall line maintenance (Seigel and van den Heever, 2012b).

SYNERGY's LH contributions to the squall line helps to explain why it contributes positively to the mid-level organization of the squall line. As the stronger cold pool-forced updraft (~ 1-1.5 km AGL in Fig. 7c) increases supersaturation, it leads to an increase in nucleation near cloud base at ~ 1.5 km AGL (Fig. 14d) that slightly enhances the warm-rain

process (Fig. 12d). The slight rain increase of up to 10% in this region (Fig. 10d) leads to the removal of the largest drops that temporarily shuts down the warm-rain process higher up ~ 3 km AGL (Fig. 12d). Because the precipitating droplets are removed, the surface area to volume ratio increases and promotes greater condensational growth (COND) within the updraft, especially within the 3-5 km AGL layer. The localized positive contribution to LH near the freezing level helps to drive a stronger mid-level updraft (Fig. 7c) that positively contributes to CMT (Fig. 7a). The stronger mid-level updraft then leads to a stronger mid-level downdraft (Fig. 7d) that increases melting by up to 6%, and further contributes positively to CMT. Seigel and van den Heever (2012b) also found that enhanced latent heating near the freezing level helps to invigorate mesoscale organization of squall lines.

3.4. Summary

The goal of this study is to understand how mineral dust impacts a nocturnal squall line by separating out individual factors that contribute to the aerosol indirect effect. Using the technique of factor separation (Stein and Alpert, 1993), the contributions of mineral dust acting to alter microphysics (DUST MICRO), radiation (RADIATION), and the synergy of dust altering microphysics and radiation (SYNERGY) have been assessed for the squall line. This has been accomplished by using RAMS to simulate an idealized squall line with observed aerosol data from the NAMMA field campaign. Four simulations of the squall line were performed that systematically altered (1) the inclusions of dust acting microphysically (as CCN, GCCN, and IN) and (2) the inclusion of radiation (Table 1). Factor separation was then used to isolate three

factors (RADIATION, DUST MICRO, and SYNERGY; Table 2) from the four simulations that contribute to the squall line.

The experiments showed that the overall role of mineral dust in the squall line simulated here is to weaken the squall line through changes to precipitation processes. From DUST MICRO, it has been shown that as the mineral dust is ingested into the squall line it acts as both CCN (mainly small dust mode) and GCCN (mainly large dust mode), which accelerates the collision-coalescence process of warm rain production. This has been seen by other studies of warm clouds in polluted environment (Feingold et al., 1999; Cheng et al., 2009). The increase in warm rain near the gust front due to DUST MICRO results in a reduction in liquid water aloft and reduces the contribution to latent heating by riming by up to 30%, which weakens the main updraft of the squall line. The contribution from DUST MICRO to the mid-level portion of the squall line is also to decrease ice mass and weaken the mesoscale downdraft. The combination of weaker updrafts and downdrafts from DUST MICRO reduces the convective momentum transport and the overall squall line organization. In association with these processes, the cold pool is weaker, precipitation is reduced, and the total convective mass flux along with net latent heating is suppressed.

In contrast to the microphysical impacts of mineral dust, the role of RADIATION is to invigorate the squall line. This first begins by aiding ice nucleation and ice growth by vapor deposition due to the enhanced cloud top cooling by outgoing longwave radiation. The increase in ice mass due to RADIATION helps strengthen the mesoscale downdraft of the squall line, which enhances the convective momentum transport, surface cold pool, and precipitation. These all combine to then strengthen the low-level updrafts, which enhance supersaturation that aids condensation and additional latent heat release. This further strengthens the mesoscale

organization of the squall line and promotes a positive feedback that is likely initiated from cloud top cooling.

By quantifying the individual contributions to the squall line due to DUST MICRO and RADIATION, it was then possible to assess the SYNERGY contribution to the squall line. SYNERGY represents the non-linear component of the AIE and is the result of the synergistic response to the squall line by having both radiation included and microphysically active dust present. While the overall contribution by SYNERGY to the squall line is small, it is positive for mesoscale organization. This stems from a change to the mid-level microphysical processes of the squall line due to SYNERGY. By having a slightly stronger low-level updraft, additional dust is nucleated by SYNERGY that enhances the warm-rain process just enough to remove the largest rain droplets while still maintaining sufficient droplet surface area to promote extra condensation. The additional latent heating by condensation near the freezing level facilitates a stronger mid-level updraft. This increases melting and results in a stronger mid-level downdraft. The stronger mid-level dynamics promotes better mid-level organization, but is not strong enough to significantly impact precipitation and cold pool intensity.

As the squall line simulated in this study is nocturnal, only the impacts of longwave forcing are considered. During the day, the presence of shortwave radiation may change the impact of both the mineral dust AIE and radiation on the simulated squall line. Therefore, current research is underway to examine the sensitivity of squall lines to mineral dust AIE during the daytime.

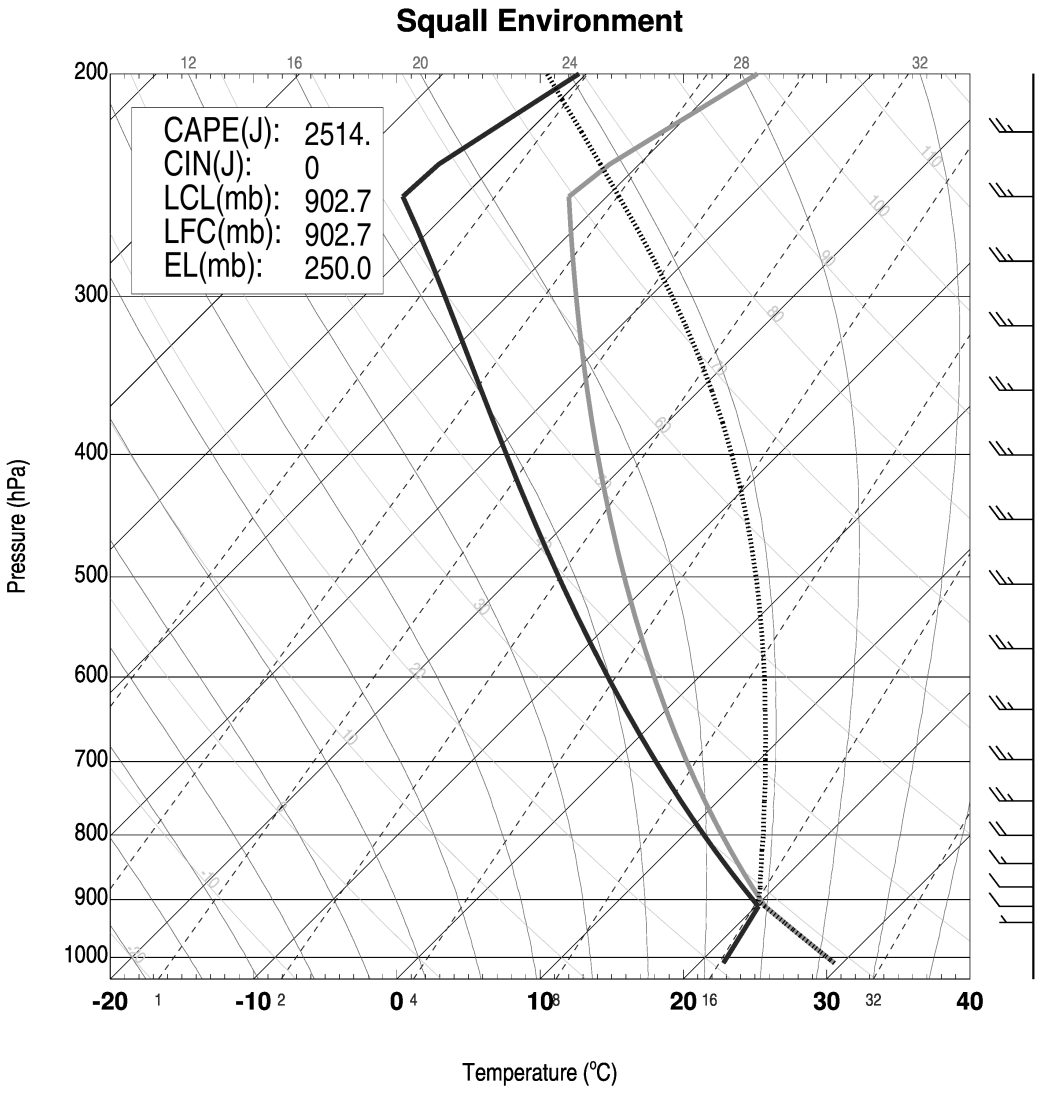

Figure 3.1. Horizontally homogeneous environmental conditions initialized for the squall line. The thick grey line is the temperature profile and the thick black is the moisture profile. The thick dashed line is the adiabatic parcel curve. Following Weismann and Klemp (1982).

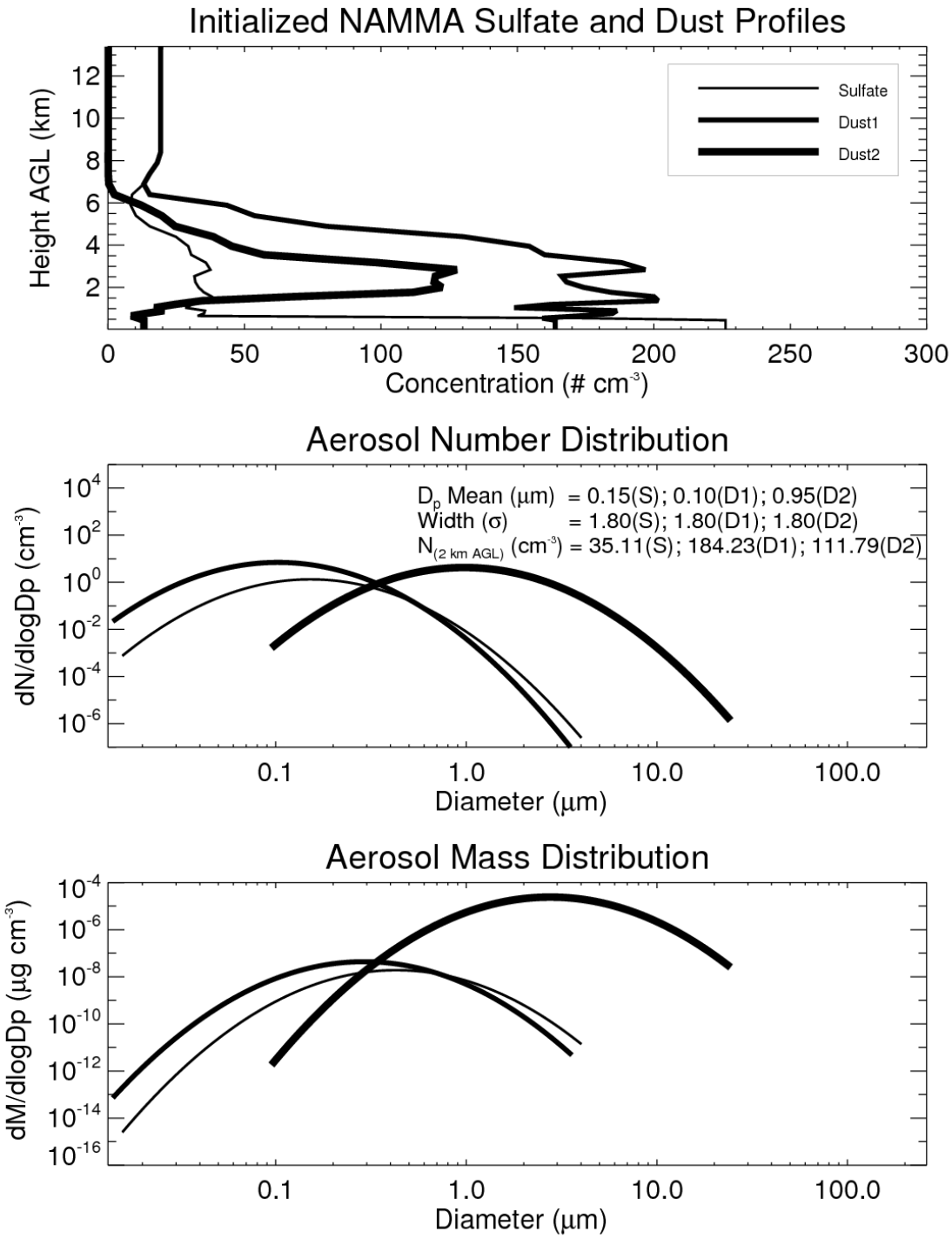

Figure 3.2. Aerosol data from NASA African Monsoon Multidisciplinary Analyses (NAMMA) in 2006. The three aerosol species represented in the study are sulfate (thin), small dust (medium thickness), and large dust (thick). Top: the initialized horizontally-homogeneous profiles (cm^{-3}); middle: aerosol number distribution at 2 km AGL; and bottom: aerosol mass distribution at 2 km AGL. Also shown on (b) are the geometric mean particle diameter, distribution width parameter, and the total number concentration for sulfate (S), Dust1 (D1), and Dust2 (D2).

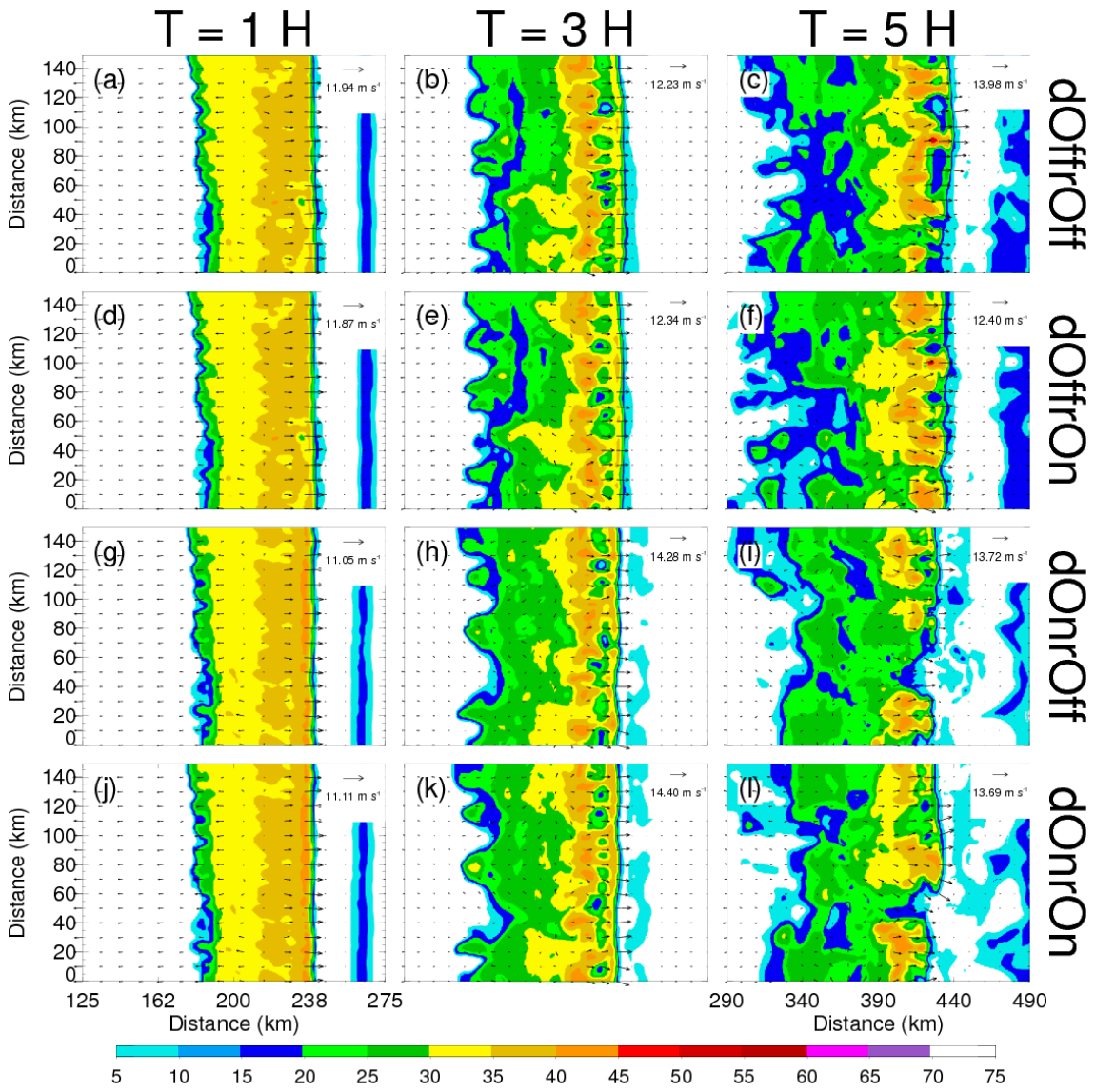

Figure 3.3. Simulated base radar reflectivity (dBZ; Matrosov 1999) of dOffrOff (a-c), dOffrOn (d-f), dOnrOff (g-i), and dOnrOn (j-l) at 1 km AGL for: (a,d,g,j) T=1h; (b,e,h,k) T=3h; and (c,f,i,l) T=5h into the sensitivity simulations. The surface winds are shown (vectors) along with the maximum surface wind reference vector in the upper-right corner for each image.

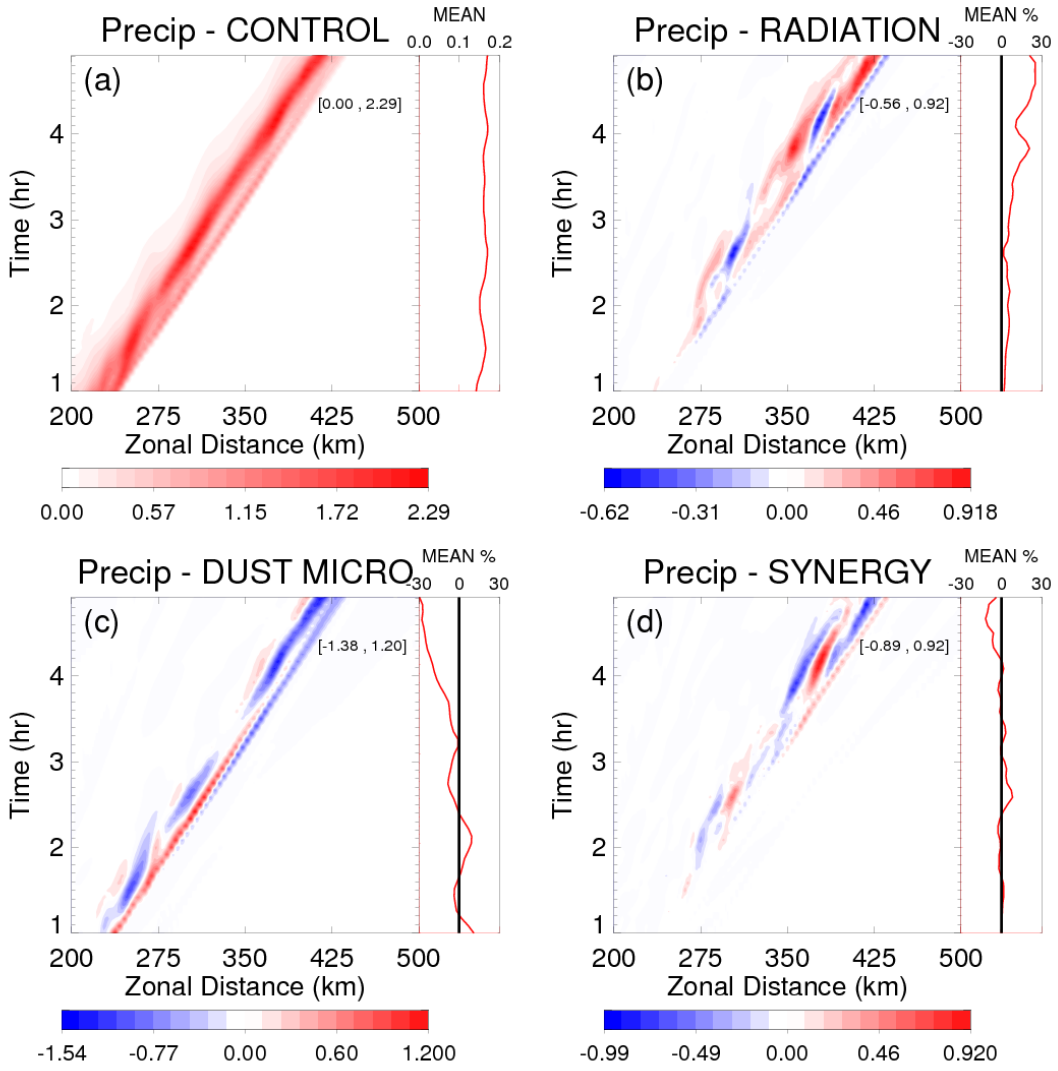

Figure 3.4. Meridionally averaged accumulated precipitation (mm $5min^{-1}$) for the four factors of (a) CONTROL, (b) RADIATION, (c) DUST MICRO, and (d) SYNERGY. See Tables 1 and 2 for factor descriptions. The accumulated precipitation is expressed as a both a Hovmöller diagram (shading) and a zonally averaged time series that is expressed as a percent contribution relative to CONTROL (line plot).

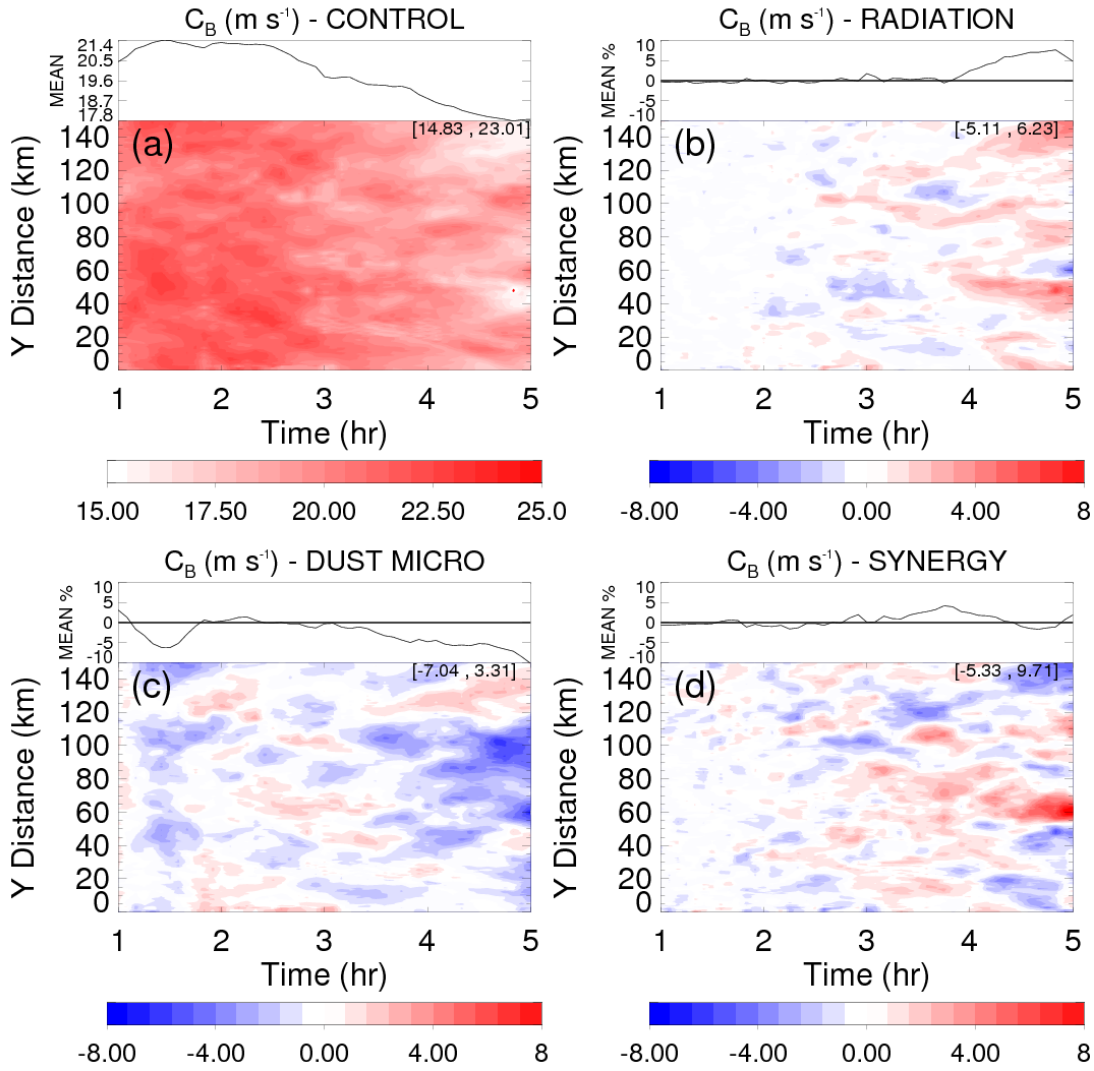

Figure 3.5. Theoretical cold pool speed, which is defined in (1), shown for the four factors of (a) CONTROL, (b) RADIATION, (c) DUST MICRO, and (d) SYNERGY. The cold pool speed is expressed as a both a rotated Hovmöller diagram (shading) and a meridionally averaged time series that is expressed as a percent contribution relative to CONTROL (line plot).

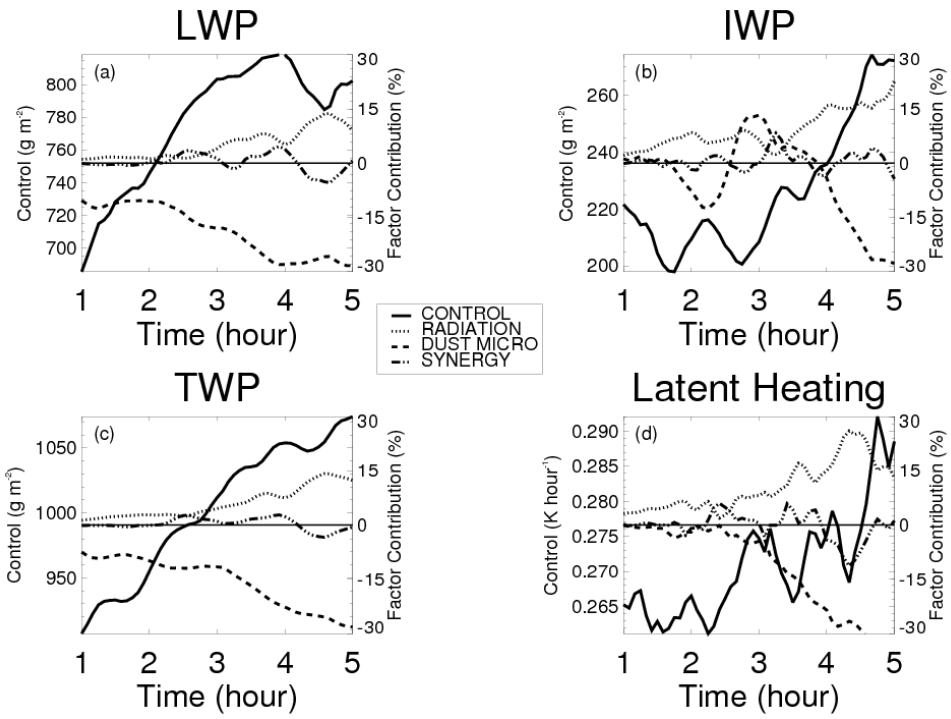

Figure 3.6. Domain averaged time series of (a) liquid water path (g m^2), (b) ice water path (g m^2), (c) total water path (g m^2), and (d) troposphere depth normalized, vertically integrated latent heating rate (K $hour^{-1}$). The solid lines correspond to CONTROL with the full field values on the left axes. The dotted (RADIATION), dashed (DUST MICRO), and dot-dash (SYNERGY) lines correspond to the factors and are expressed as a percent contribution to CONTROL on the right axes.

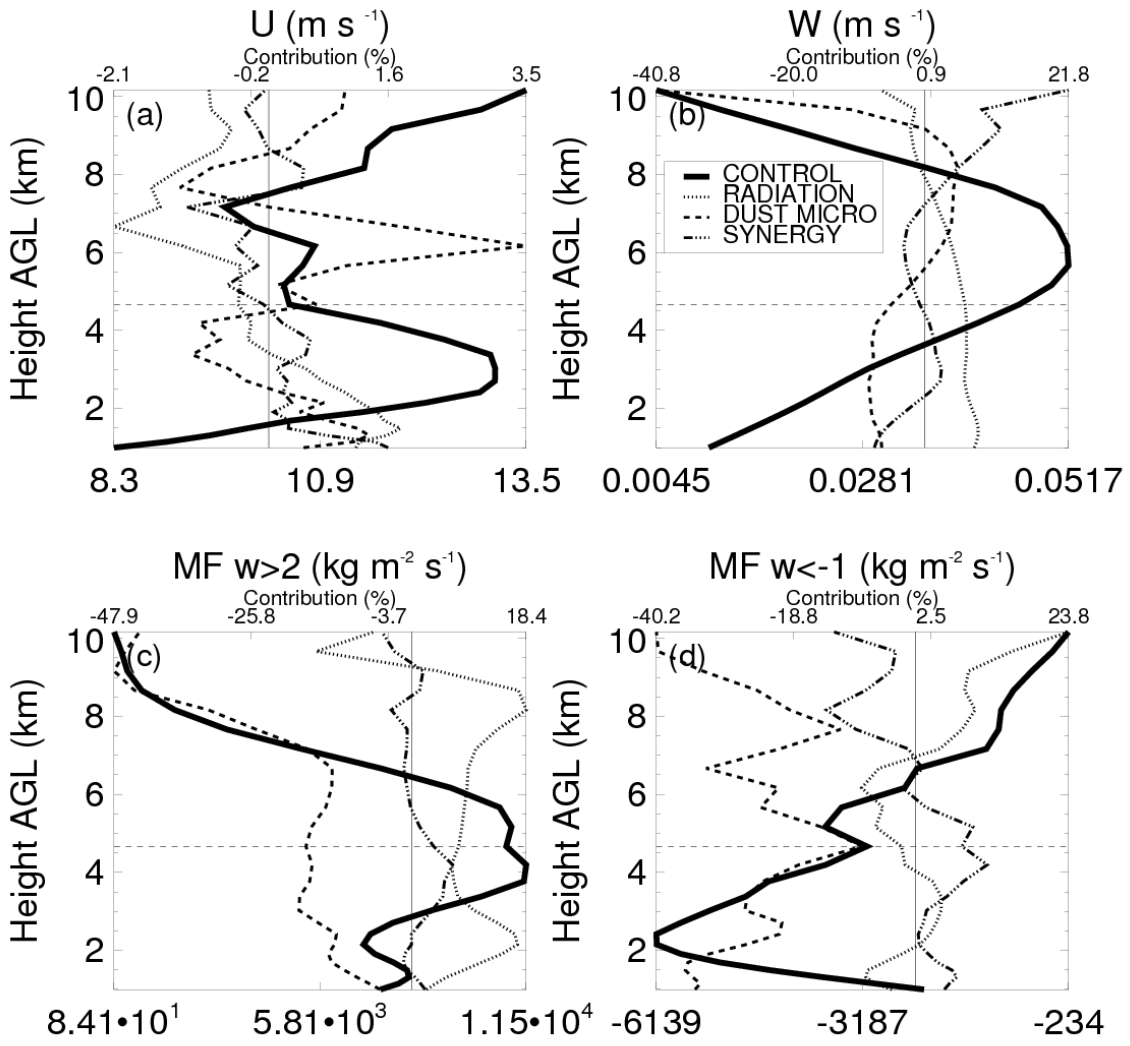

Figure 3.7. Domain averaged vertical profiles of (a) zonal wind (m s^{-2}), (b) vertical velocity (m s^{-2}), (c) total convective mass flux sampled where W > 2 m s^{-2} (kg m^{-2} s^{-1}), and (d) total downdraft mass flux sampled where W < -1 m s^{-2} (kg m^{-2} s^{-1}). The solid lines correspond to CONTROL with the full field values on the bottom axes. The dotted (RADIATION), dashed (DUST MICRO), and dot-dash (SYNERGY) lines correspond to the factors and are expressed as a percent contribution to CONTROL on the top axes.

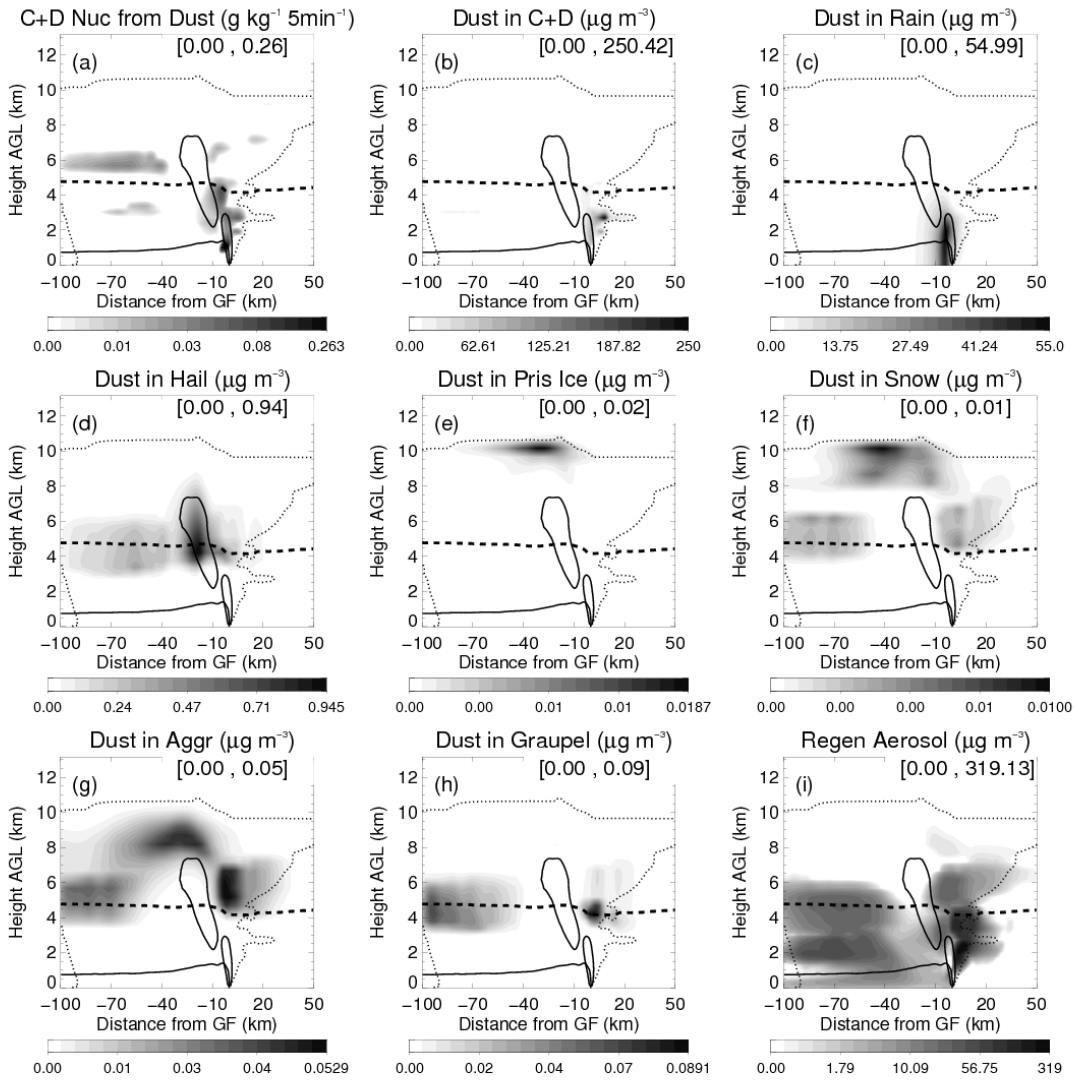

Figure 3.8. The dOnrOn squall line, which has been averaged both meridionally along the gust front and temporally from sensitivity simulation hours 1-5. Each vertical cross section is expressed as a horizontal distance from the gust front (X-axis) and a vertical distance AGL (Y-axis). Shown on each cross section is the squall line cloud boundary [dotted line; 0.05 g kg^{-1} total condensate], the freezing line [dashed black line], the cold pool boundary [thin black line below 2 km AGL; -0.05 m^2 s^{-2} following Tompkins (2001)], the 1 m s^{-1} updraft region [thick black lines stemming from the gust front], and [min, max] values for the shaded quantities of: (a) cloud and drizzle (C+D) nucleation rate by dust; (b) dust within C+D; (c) dust within rain; (d) dust within hail; (e) dust within pristine ice; (f) dust within snow; (g) dust within aggregates; (h) dust within graupel; and (i) concentration of regeneration aerosol. The units are shown on the figure for each quantitiy.

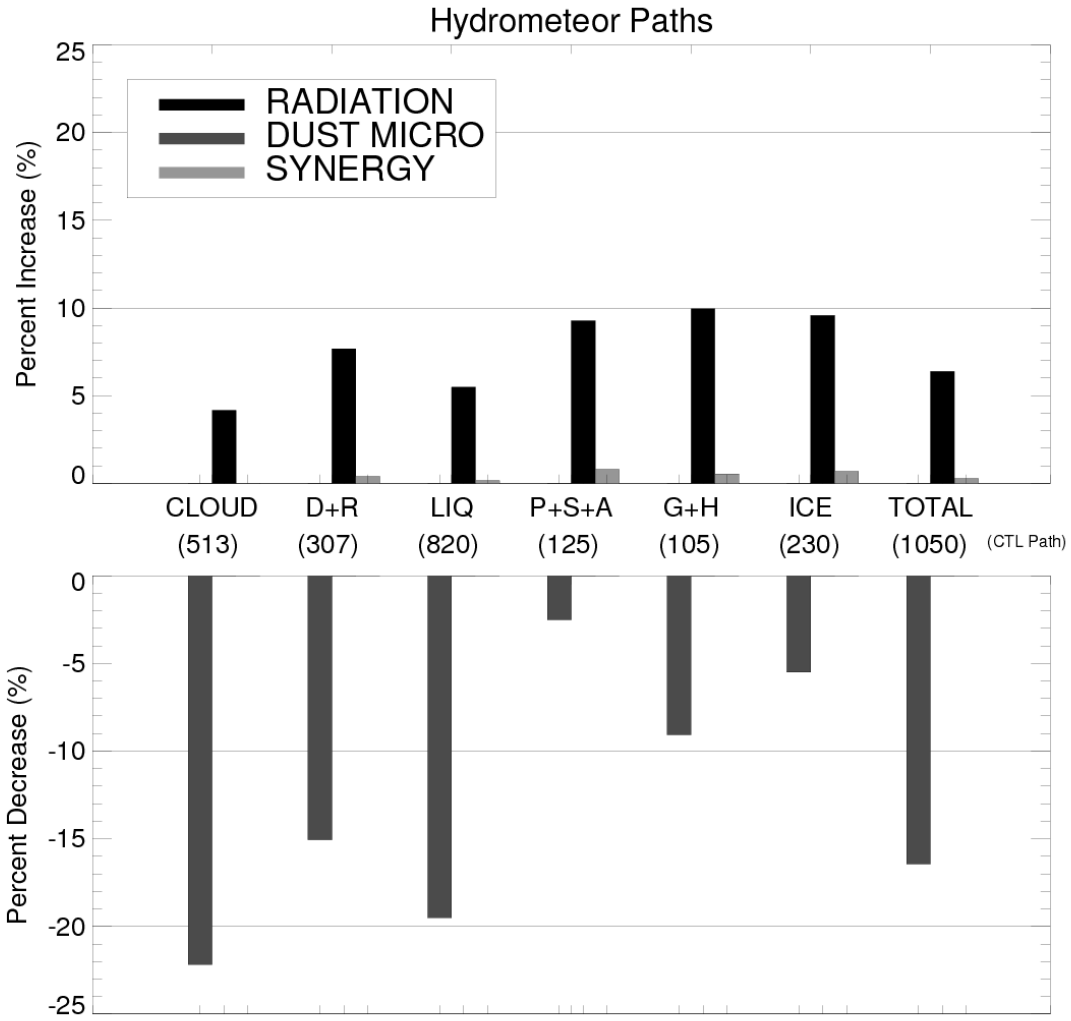

Figure 3.9. Horizontally averaged, vertically integrated mixing ratios of various hydrometeors, referred to in the text as hydrometeor paths (g m^2). The hydrometeor paths are expressed as a percent contribution to CONTROL by RADIATION (black bars), DUST MICRO (gray bars), and SYNERGY (light gray bars). D+R is drizzle and rain, P+S+A is pristine ice and snow and aggregates, and G+H is graupel and hail. The numbers below each hydrometeor group are the full field path value for CONTROL.

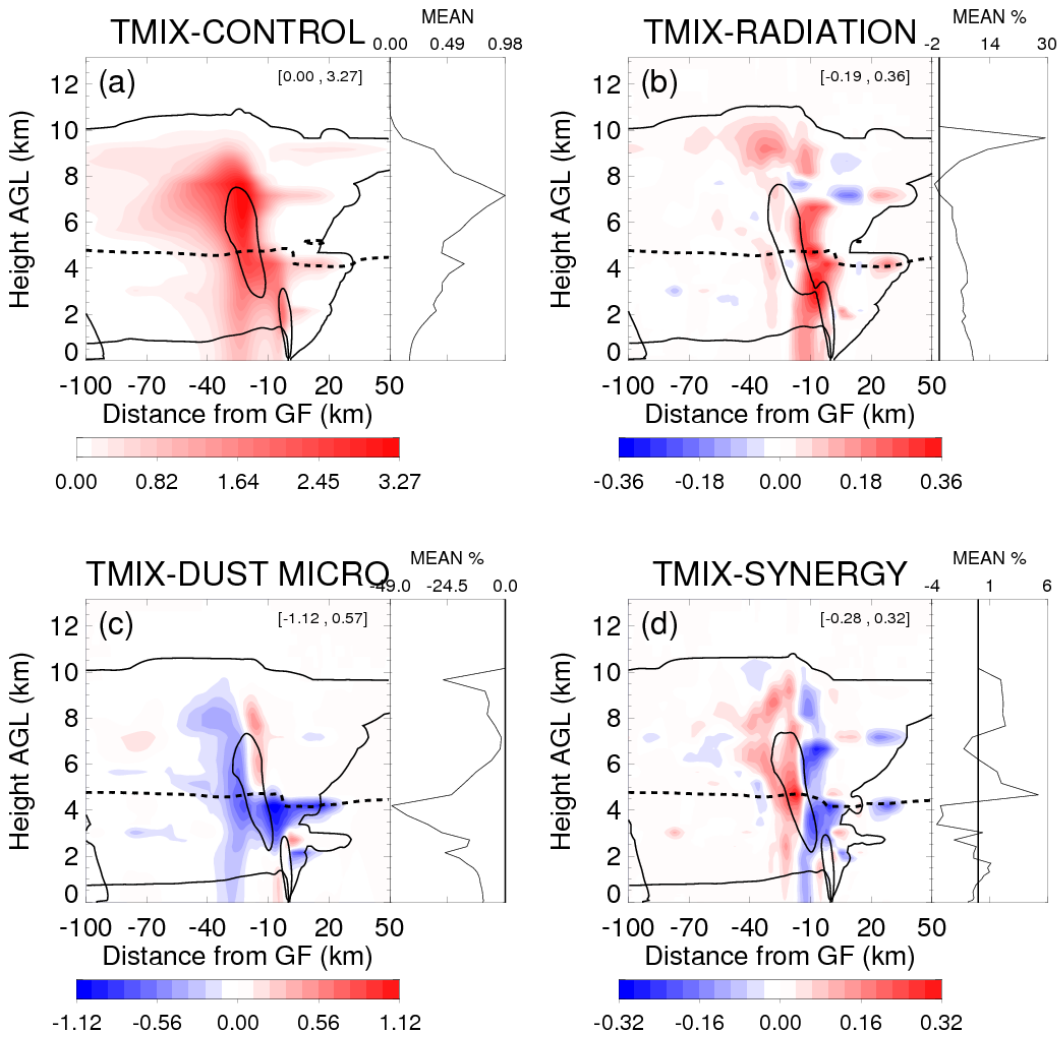

Figure 3.10. Meridionally-averaged along the gust front and temporally-averaged total condensate mixing ratio (TMIX; g kg^{-1}) for (a) CONTROL, (b) RADIATION, (c) DUST MICRO, and (d) SYNERGY from sensitivity simulation hours 1-5. Each vertical cross section is expressed as a horizontal distance from the gust front (X-axis) and a vertical distance AGL (Y-axis). Shown on each cross section is the squall line cloud boundary [thick black line; 0.05 g kg^{-1} total condensate], the freezing line [dashed black line], the cold pool boundary [thin black line below 2 km AGL; -0.05 m^2 s^{-2}] the 1 m s^{-1} updraft region [thick black "ovals" stemming from the gust front], and [min, max] values for TMIX. The cloud boundary, freezing level, cold pool, and updraft contours are of the simulations (a) dOffrOff, (b) dOffrOn, (c) dOnrOff, and (d) dOnrOn. Also shown is a zonally averaged vertical profile that is expressed as a percent contribution relative to CONTROL (line plot) for each factor.

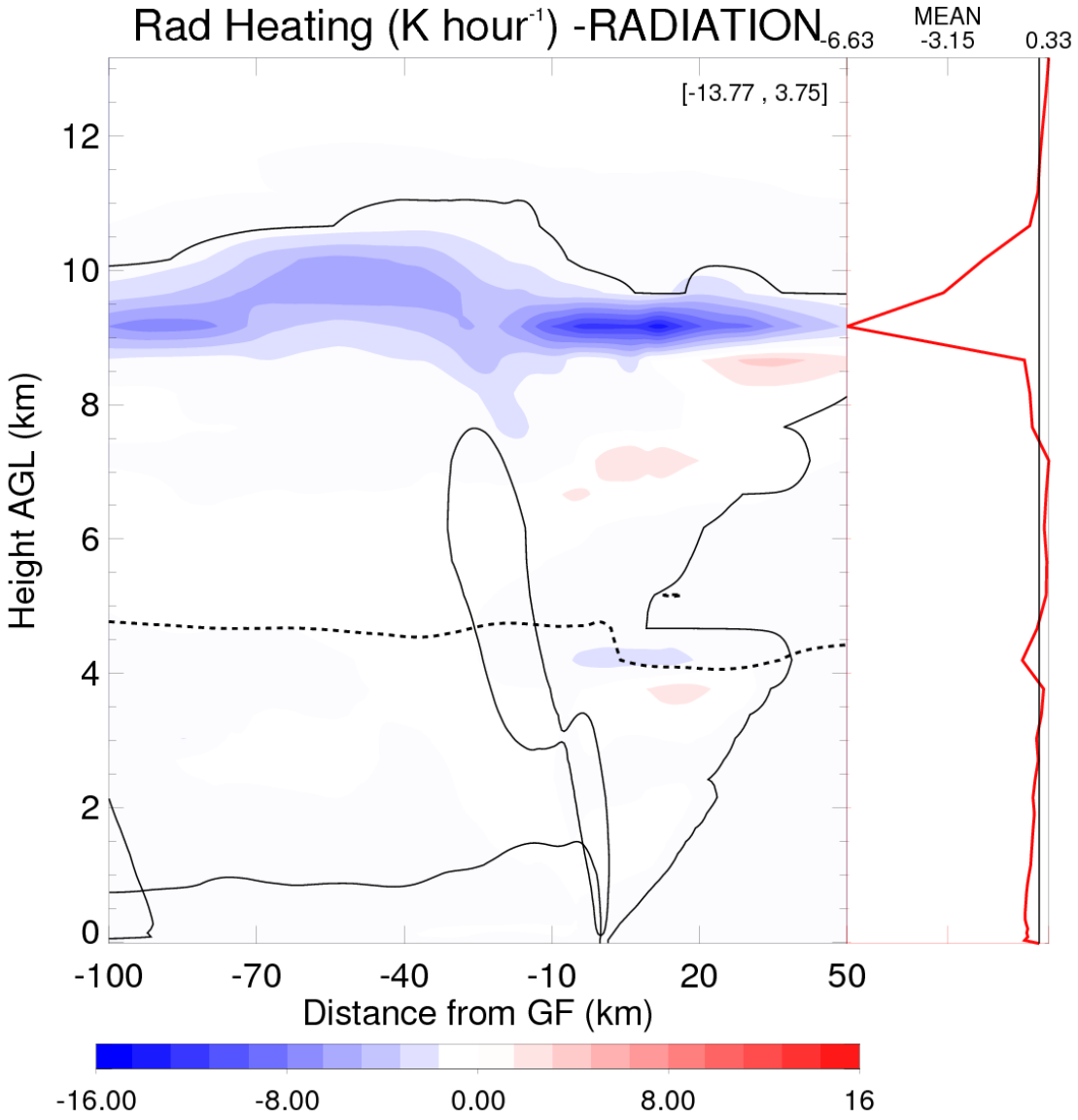

Figure 3.11. Same as Figure 10, except for radiative heating rate (K hour^{-1}) and only shown for RADIATION and dOffrOn.

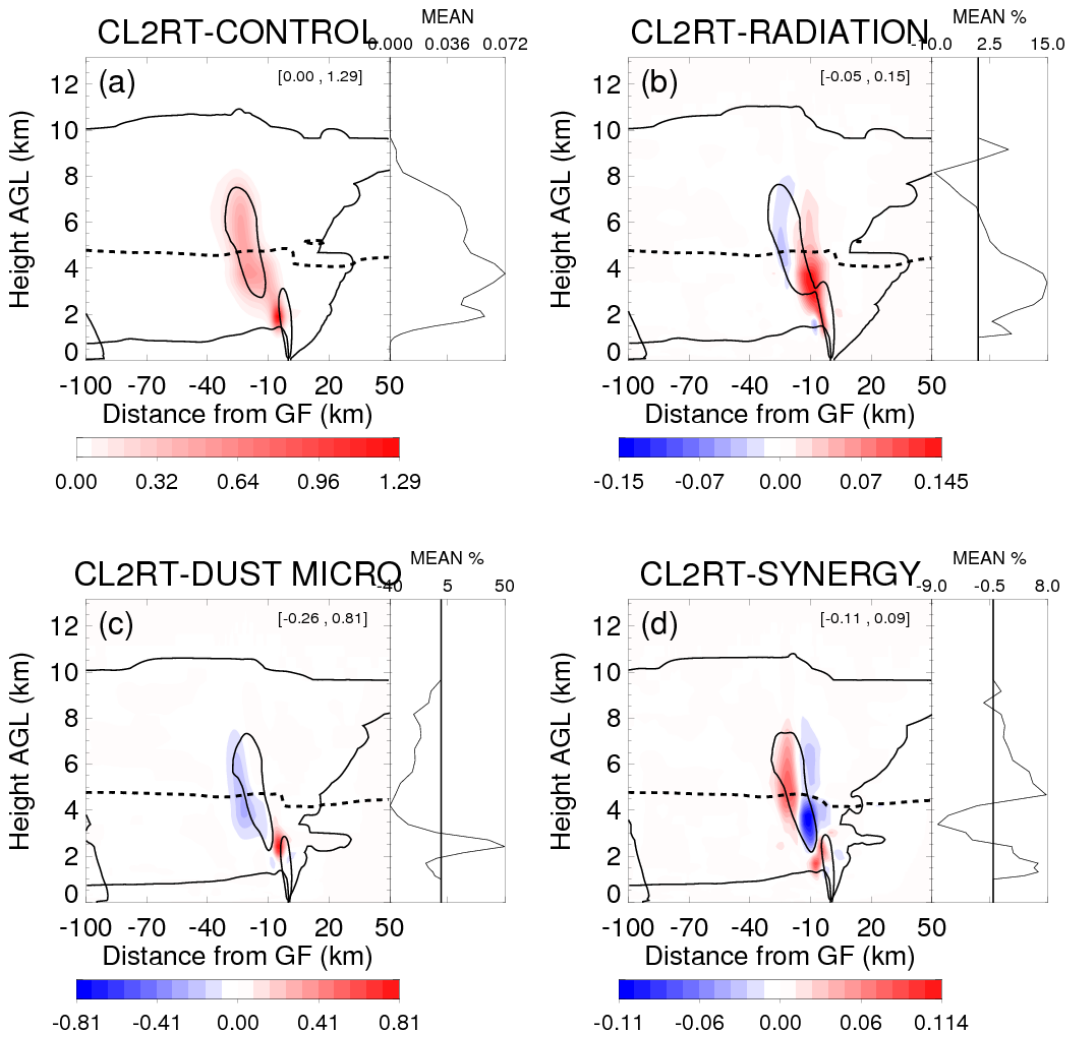

Figure 3.12. Same as Figure 10, except for the collision-coalescence rate (g kg^{-1} $5min^{-1}$) between cloud and rain.

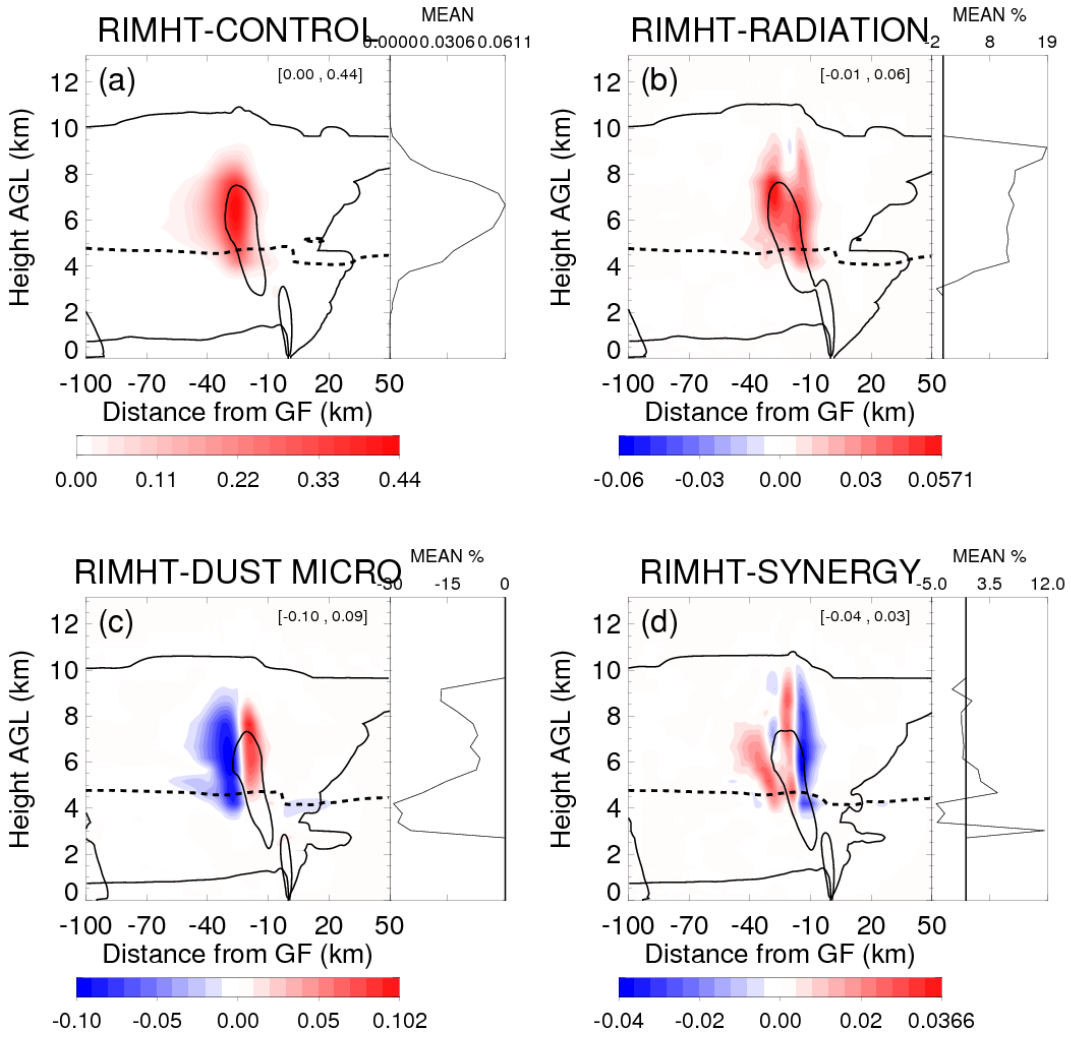

Figure 3.13. Same as Figure 10, except for the riming rate of cloud water onto hail (g kg^{-1} $5min^{-1}$).

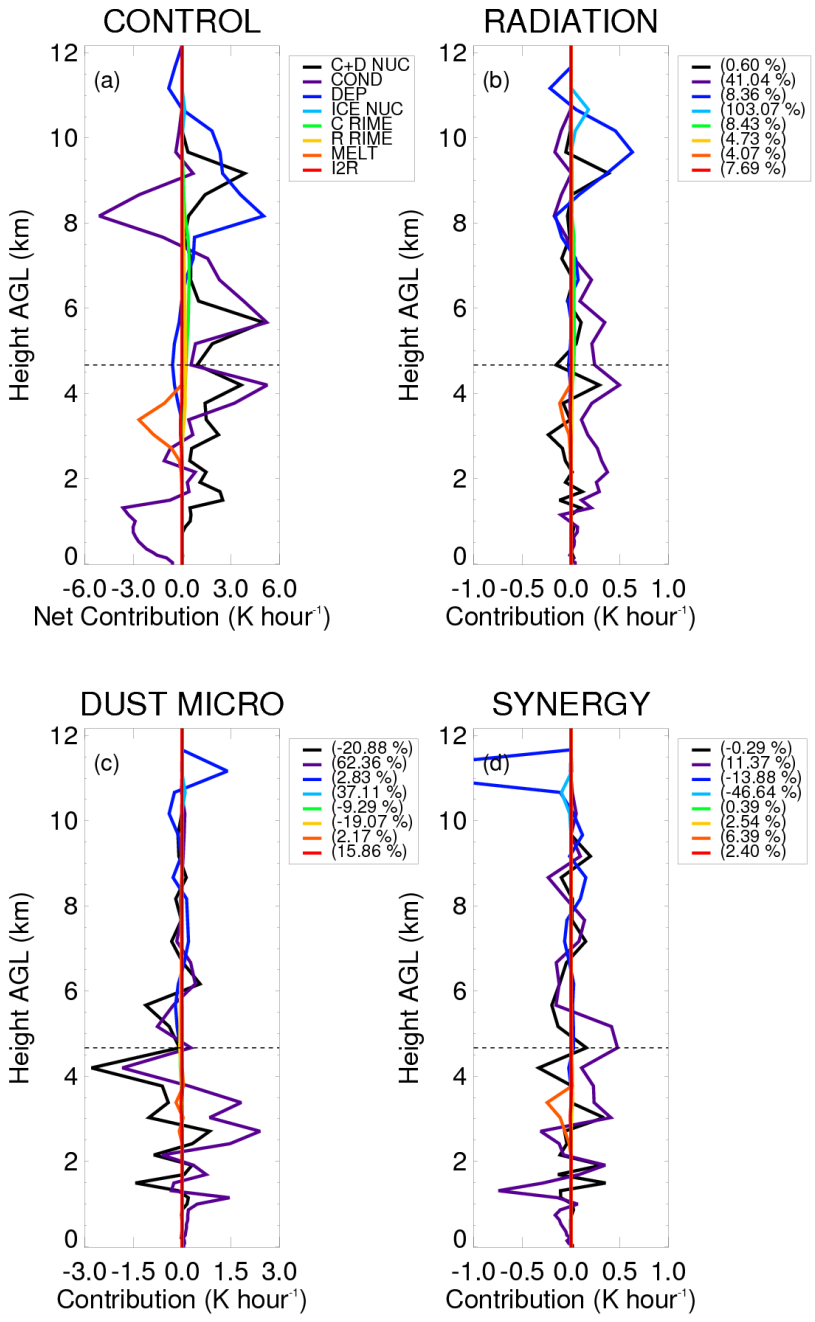

Figure 3.14. Cloud averaged vertical profiles of all microphysical processes that contribute to latent heating (K hour^{-1}) for (a) CONTROL, (b) RADIATION, (c) DUST MICRO, and (d) SYNERGY. Cloud is defined by any grid cell that contains at least 0.01 g kg^{-1} of total condensate.

Table 3.1. Description and naming convention of the four experiments

Name	Description
dOffrOff	• Dust being microphysically active is OFF • Radiation is OFF
dOffrOn	• Dust being microphysically active is OFF • Radiation is ON
dOnrOff	• Dust being microphysically active is ON • Radiation is OFF
dOnrOn	• Dust being microphysically active is ON • Radiation is ON

Table 3.2. The components and naming convection of the factor separation analysis.

Factor	Name	Description	Calculation
f_0	CONTROL	Part of the predicted field independent from dust altering the microphysics and radiation	f_0 = dOffrOff
f_1	RADIATION	Part of the predicted field from the sole contribution of radiation	f_1 = dOffrOn – dOffrOff
f_2	DUST MICRO	Part of the predicted field from the sole contribution of dust altering the microphysics	f_2 = dOnrOff – dOffrOff
f_{12}	SYNERGY	Part of the predicted field from the synergistic effects of dust altering the microphysics *and* radiation	f_{12} = dOnrOn – (dOnrOff + dOffrOn) + dOffrOff

CHAPTER 4: SQUALL LINE INTENSIFICATION VIA HYDROMETEOR RECIRCULATION

4.1. Introduction

The role of the RIJ has been shown to be a key component in the structure and maintenance of squall lines (Smull and Houze 1987; Fovell and Ogura 1989; Lafore and Moncrieff 1989; Weisman 1992; Tao et al. 1995; Grim et al. 2009). The RIJ forms predominantly in response to mid-level horizontal pressure and buoyancy gradients. These gradients are generated by both the latent heating of the main convective updraft and the dipole of upper-level latent heating above low-level latent cooling in upshear-tilted squall lines, driving a mid-level mesolow (Brown 1979; Smull and Houze 1987; Weisman 1992; Haertel and Johnson 2000). The rear-to-front flow of the RIJ impacts squall line intensity by (1) enhancing convective downdrafts that aid in strengthening the surface cold pool (Fovell and Ogura 1989; Fovell 1991; Weisman 1992; Tao et al. 1995); (2) transporting momentum from aloft to the surface cold pool, thereby assisting deeper lifting near the gust front (Newton 1950; Smull and Houze 1987; Lafore and Moncrieff 1989; Weisman 1992); and (3) transporting horizontal vorticity to the leading edge of upshear-tilted squall lines that have an elevated RIJ, such that it opposes the sign of horizontal vorticity within the cold pool and aids the dynamical balance between the cold pool and environmental shear (Rotunno et al. 1988; Weisman 1992,1993). In general, the dominant communication between the RIJ and the intensity of the convective line is through the cold pool.

Studies have shown that the cold pool plays a key role in the lifecycle and dynamics of squall lines (Thorpe et al. 1982; Rotunno et al. 1988 [hereafter RKW88], 1990; Weisman et al. 1988 [hereafter WKR88]; Weisman 1992, 1993; Weisman and Rotunno 2004, 2005 [hereafter WR04 and WR05], 2005; Bryan et al. 2006). RKW88 proposed perhaps the most widely accepted theory for squall line maintenance in which a balance exists between the vorticity generated within the cold pool and the environmental shear. If the vorticities are similar in magnitude but have the opposite sign, then the convective updraft remains upright, which yields the deepest lifting of environmental air and maximum system intensity. RKW88 described this balance using a ratio between cold pool propagation speed (C) and the environmental shear (ΔU), $C/\Delta U$, which was derived using simplifying assumptions of the horizontal vorticity equation. However, numerous factors should be taken into consideration when using RKW88 theory for squall line analysis, such as: (1) the depth and location of the shear layer (WKR88; WR04; Stensrud et al. 2005; WR05; Coniglio et al. 2012), (2) the calculation of cold pool intensity (Stensrud et al. 2005; WR05; Bryan and Parker 2010; Coniglio et al. 2012), (3) stability layers that can interact with the cold pool dynamics (Carbone et al. 1990; Xue 2002; Seigel and van den Heever 2012a), and (4) microphysics (e.g. Fovell and Ogura 1989; Ferrier et al. 1995; Adams-Selin et al. 2012a,b; Bryan and Morrison 2012).

Numerous studies have shown the sensitivity of simulated squall lines to microphysics (Morrison et al. 2009; Bryan and Morrison 2012; Morrison et al. 2012; van Weverberg et al. 2012) and the importance of the ice phase feeding back onto squall line dynamics (Nicholls 1987; Fovell and Ogura 1988; McCumber et al. 1991; Tao et al. 1995; Liu et al. 1997; Adams-Selin et al. 2012a,b; Bryan and Morrison 2012). Fovell and Ogura (1988) were one of the first to show that the inclusion of the ice phase resulted in a more realistic representation of an upshear-

tilted squall line. Tao et al. (1995) demonstrated that the exclusion of the melting process leads to a less commonly observed unicell-type squall line, while the inclusion of the melting process strengthens the RIJ and forces the squall line to tilt upshear as a multicellular system. Bryan and Morrison (2012) found that a numerically simulated squall line with hail microphysics and fine horizontal grid spacing best reproduced an observed squall line. A dependency on melting rates has also been found to impact squall line structure and the subsequent bow echo formation, as shown by Adams-Selin et al. (2012a) in which faster melting rates yield stronger rear-inflow and more frequent, more intense bow echoes. From these studies, it can be seen that there is an intricate balance between the microphysics, which is responsible for latent heating and the associated buoyancy, and the dynamics of the squall line itself. Through both hydrometeor loading and the vertical distribution of latent heating, the behavior of a squall line is subject to changes in the microphysics.

The research presented in this paper attributes another role to the RIJ of a squall line through microphysical influences. Using simulations of an idealized squall line with a convection-resolving model (CRM), it is found that for an upshear-tilted squall line the RIJ can play an integral role in recycling hail and rain hydrometeors that fall out from the updraft back into the main convective updraft, thereby locally enhancing latent heating and generating greater positive buoyancy. In order to assess the importance of this *recirculation mechanism*, sensitivity experiments are performed that vary the mean diameter of the hail hydrometeor size distribution, which can occur in reality via mechanisms such as aerosol ingestion (Tulet et al. 2010; Seigel and van den Heever 2012b) and subsequent microphysical processing (e.g. van den Heever et al. 2006, 2011; Storer et al. 2010; Lebo and Seinfeld 2011). The following section describes the model used for this study and the experimental design. Section 3 presents the results of this

mechanism based on the control simulation, and Section 4 presents and discusses the results of the sensitivity experiment. Finally, a summary is provided in Section 5.

4.2 Methods

4.2.1. Model description

The numerical model that was used for the squall line simulations analyzed here is the non-hydrostatic Regional Atmospheric Modeling System (RAMS; Pielke et al. 1992; Cotton et al. 2003; Saleeby and Cotton 2004). As microphysics has been shown to be an important factor in correctly reproducing squall lines (Tao et al. 1995; Fovell et al. 2006; Adams-Selin et al. 2012a,b; Bryan and Morrison 2012; Morrison et al. 2012; Van Weaverberg et al. 2012), RAMS is appropriate for this numerical study given its sophisticated bin-emulating two-moment bulk microphysical parameterization scheme that prognoses mass mixing ratio and number concentration for eight hydrometeor species [cloud droplets, drizzle, rain, pristine ice, snow, aggregates, graupel, and hail] (Meyers et al. 1997; Cotton et al. 2003; Saleeby and Cotton 2004). The representation of numerous hydrometeor species that all conform to a generalized gamma distribution (Flatau et al. 1989; Verlinde et al. 1990) helps to resemble the continuous spectrum of hydrometeors within the atmosphere. Each hydrometeor distribution has its own density and power law relationship as a function of diameter that allows mass stratification from sedimentation (Walko et al. 1995). Other schemes used in the simulations are radiative lateral boundary conditions (Klemp and Wilhelmson 1978), a Rayleigh damping layer within the top six levels of the model domain, the Smagorinsky (1963) turbulence closure scheme, and Harrington

(1997) two-strean radiation (Lilly 1962; Hill 1974). The Land Ecosystem-Atmosphere Feedback model (LEAF3; Walko et al. 2000) is also used to simulate realistic surface drag over a land-surface of bare soil. Coriolis forcing is excluded to keep the squall line flow predominantly perpendicular to the meriodionally oriented cold pool.

4.2.2. Experimental design

In this study, four idealized simulations are performed of a continental-type squall line to investigate a microphysical recirculation mechanism that is hypothesized to enhance squall line intensity. All simulations are performed in three dimensions with a constant horizontal grid spacing of 500 m and a stretched vertical grid from 50 m to 500 m. The model domain covers a volume of 500 x 150 x 26 km in the zonal, meridional, and vertical directions, respectively. The time step used is 3 s and time integration is performed for 7 hours nocturnally, as this is the peak occurence time of MCSs (Laing and Fritsch 1997; Anderson and Arritt 1998; Jirak et al. 2003). For cloud and ice nucleation in all simulations, background concentrations of 600 cm^{-3} and 10,000 kg^{-1} are used for aerosol species that can be activated as cloud condensation nuclei (CCN) and ice nuclei (IN), respectively, and are typical amounts for continental aerosol regimes (DeMott et al. 2003; Ward and Cotton 2011).

The model setup used here is similar to other previous idealized studies (Trier et al. 1997; Fierro et al. 2008; Morrison et al. 2009). The model is initialized with horizontally homogenous temperature and moisture profiles (Figure 4.1) following Weisman and Klemp (1982), however the boundary layer temperature profile has been adjusted to that of a well-mixed boundary layer (constant potential temperature) to better represent surface-based lifting (i.e. neutral buoyancy of

dry surface air parcels within the boundary layer). The shear profile used for this analysis linearly increases from 0 to 12.5 m s^{-1} in the lower 2.5 km (Figure 4.1) and has been chosen to closely match a C/ΔU ratio ~ 1, which will be discussed further in Section 4. This shear value and depth is within the range used by previous studies (Weisman 1992,1993; Weisman and Rotunno 2004; Frame and Markowski 2006; Bryan et al. 2007). The squall lines are initiated using a 4 km deep, -6 K line thermal resting on the surface, representing a cold pool, and contains random embedded $-0.1 \le \theta \le 0.1$ potential temperature (θ) perturbations to initiate three-dimensional motions. All of the analysis presented here is from three hours after initialization to allow for sufficient spin up of each squall line and to ensure they are self-sustaining.

The squall line recirculation mechanism that is discussed in Section 3 is highly dependent on the size of the hail hydrometeors and their location relative to the convective updraft. Because of this dependence, the experiments presented in this paper are designed to most naturally isolate the recirculation mechanism while maintaining full microphysical representation to best simulate deep moist convection as seen in reality. The experiments consist of a control simulation that uses the full two-moment microphysical scheme (Meyers et al. 1997; Saleeby and Cotton 2004) for all hydrometeors (herein referred to as '2MOM') and three sensitivity simulations that use two-moment microphysics for the nucleating water species (e.g. cloud water, drizzle, and pristine ice) and one-moment microphysics (Walko et al. 1995) for the remaining species (e.g. rain, snow, aggregates, graupel, and hail) to control the variation in hail hydrometeor size, while still keeping the sophisticated nucleation scheme in RAMS active and for best comparison to 2MOM.

The sensitivity simulations all use identical hydrometeor size distributions for rain, snow, and graupel, but vary the mean diameter of the hail size distribution. The range of mean hail

sizes tested for the sensitivity experiments was chosen based on those seen in the control simulation, which ranged from approximately 0.5 mm to 5 mm, and are 1 mm (herein referred to as '1MM'), 5 mm (herein referred to as '5MM'), and 1 cm (herein referred to as '1CM') (Table 4.1). The variation in hail mean diameter permits some degree of direct control over the recirculation mechanism because as hail size increases, its: (1) fall velocity increases; (2) in-cloud residence time decreases; (3) surface area to volume ratio decreases; and (4) position relative to the convective updraft changes. It should be noted that by simply changing the characteristics of hail hydrometeors, various other microphysical processes will also likely be affected that will lead to changes in squall line characteristics. This has been shown for supercells (Gilmore et al. 2004; van den Heever and Cotton 2004; Dawson et al. 2010), squall lines (Ferrier et al. 1995; Bryan and Morrison 2012), and bow echoes (Adams-Selin et al. 2012a,b). However, varying the mean diameter of the hail size distribution provides the most direct contol over the recirculation mechanism while still representing all of the microphysical processes that are seen in reality, without unintentionally and unknowingly biasing a specific process. In order to most effectively assess the recirculation mechanism, a detailed microphysical analysis for the sensitivity simulations is presented in Section 4.

4.3 Control experiment

4.3.1. Squall line overview

Within the first ten minutes of the control simulation (2MOM), deep convection is initiated linearly along the imposed cold pool edge. During the first three hours (i.e. squall line

spin up), the deep convection organizes into a squall line with typical characteristics. Figure 4.2 highlights the convective evolution of the 2MOM squall line from hours 2-7 after initialization and shows simulated radar reflectivity at a height of 1 km AGL, following the methodology of Matrosov (1999). Two hours into the simulation, the zonally propagating squall line is beginning to break down into individual convective cells, as is evident by the 3.5 km AGL 5 m s^{-1} updraft contours. Between hours 3 and 7, the squall line transforms into a mature mesoscale convective system that contains trailing stratiform precipitation and peak reflectivity leading the convective line. Towards the latter half of the simulation, bowing structures develop as RIJs organize within the squall line that are collocated with intense updrafts and heavy precipitation (Fig. 4.2d-f).

The data in some analyses presented hereafter have been averaged first meridionally along the surface cold pool boundary, and then temporally, thus effectively resulting in a vertical cross section of the squall line in order to obtain a cohesive view of the simulated system. The cold pool boundary (or gust front) is defined by the -0.05 m^2 s^{-2} buoyancy surfaces. Buoyancy is defined after Tompkins (2001) as:

$$B \equiv g\left(\frac{\theta_V'}{\overline{\theta}_V} - q_C\right), \tag{1}$$

where $\overline{\theta}_V$ is the mean virtual potential temperature downshear of the squall line at the respective y grid point, θ_V' is the local virtual potential temperature perturbation relative to $\overline{\theta}_V$, and q_C is the total condensate mixing ratio. It should be noted that all quantities presented as averages have been calculated prior to spatial and temporal averaging.

The simulation produces an upshear tilted squall line, as is obvious from several classic squall line characteristics evident in Figure 4.3. Front-to-rear flow, broad anvil divergence, and a

RIJ located 2-4 km AGL are apparent in the storm relative wind field (Figure 4.3a; Weisman 1992, 1993; Trier et al. 1997; Parker and Johnson 2000; Houze 2004). Also, the convective updraft can be seen extending from the cold pool up through the anvil and downshear of the mesoscale downdraft (Fig. 4.3b; Smull and Houze 1987). The spatial disconnect between the cold pool forced updraft and the mid-level updraft evident here has been seen in other observational and modeling studies (Jorgensen et al. 1997; Trier et al. 1997; Takemi and Satomura 2000; Bryan et al. 2003, 2007; Xiao and Sun 2007; Fierro et al. 2009; Morrison et al. 2009) and is likely explained by the finer scale grid-spacing used in these simulations (500 m) compared with the more commonly used 1 km horizontal grid spacing (e.g. Fovell and Tan 1998; Weiman and Rotunno 2004) [see Fig. 4.5b in Bryan et al. 2003 showing simulated squall lines in a strongly-sheared environment using varying grid spacings]. The y-component of relative vorticity (Fig. 4.3c) shows the balance between positive and negative vorticity on the downshear and upshear flanks of the updraft, respectively, as described by RKW88 (RKW88; Tao et al. 1995; Meng et al. 2012). Finally, the pressure perturbation field (Fig. 4.3d), which has been calculated relative to the mean environmental pressure field ahead of the squall line, shows the rear-to-front horizontal pressure gradient that is hypothesized to partially drive the RIJ (Schmidt and Cotton 1990; Weisman 1992; Grim et al. 2009). The generation of the peak mid-level updraft velocity (and associated local minimum in perturbation pressure) just below the freezing level is the primary focus of this study and will be further discussed in the next section.

4.3.2. Recirculation mechanism

The upshear-sloped squall line presented in this paper contains a mid-level circulation centered at the freezing level on the upshear side of the main updraft. This circulation is found to enhance the mid-level updraft of the simulated squall line and it stems from the incorporation of RIJ-transported hydrometeors into the mid-level convective updraft. Figure 4.4 shows the cold pool and temporally averaged microphysical processes contributing to the recirculation mechanism that help to invigorate the mid-level updraft. The recirculation mechanism begins with hail that has been ejected upshear from the main convective updraft due to the front-to-rear (FTR) flow above the freezing level (Fig. 4.3a). The hail hydrometeors have grown large enough to descend below the freezing level and into the RIJ. They are then advected downshear towards the updraft, where they become entrained back into the updraft (Fig. 4.4a). The other ice species (pristine ice, snow, aggregates, and graupel) all have densities and associated fall speeds that are too low to allow sedimentation into the RIJ sufficiently close enough to the updraft in order to become entrained. Herein, entrainment is defined as the incorporation of air or hydrometeors into the main convective updraft that originated from external regions. Because the hail advection by the RIJ is occurring below the freezing level, partial melting of the hailstones (Fig. 4.4b) leads to shedding of liquid water, which generates rain hydrometeors (Fig. 4.4c) that are also advected by the RIJ into the updraft. The extra hail and rain hydrometeors within the updraft, which contains supersaturated air, increases the net surface area onto which vapor can be deposited and thus enhances the hydrometeor growth process of vapor deposition (Fig. 4.4d). This more effectively removes supersaturation (Fig. 4.4e) and positively contributes to the latent heating within the convective updraft. This can be seen in the vicinity of the marker in Figure 4.4 by the minimum

in supersaturation (Fig. 4.4e) collocated with the positive hail flux (Fig.4a) and a local maximum in rain mixing ratio (Fig. 4.4c).

The hailstones that are entrained into the mid-level convective updraft may collide with cloud and rain droplets already in the updraft. Providing that the internal energy of the hailstones is sufficiently low (i.e. the hailstones are cold; see Walko et al. (1995) for a detailed description of the treatment of the internal energy of hail within RAMS), the hailstones can then become rimed by cloud droplets and rain hydrometeors (Fig. 4.4f). This process also contributes positively to the latent heating within the convective updraft. Furthermore, some of the RIJ-advected rain hydrometeors within the updraft that have not yet collided with hailstones can also be transported higher into the storm and later serve as a source of latent heat from fusion. This will be discussed further later in this section.

To assess the relative importance of the recirculation mechanism that has just been described, a recirculation heating fraction is used that includes all of the latent heating processes directly involved in the mechanism relative to the total latent heating. The total latent heating of the mid-level updraft region is shown in Fig. 4.4g and includes the processes of condensation, evaporation, ice deposition, ice sublimation, riming, melting, cloud nucleation, and ice crystal nucleation. The microphysical processes that are not directly associated with the recirculation mechanism are cloud nucleation and cloud droplet condensation and evaporation; they may however be indirectly related through feedbacks in updraft strength, supersaturation and droplet activation. The fraction of latent heating due to those microphysical processes directly associated with the recirculation mechanism can then be defined as

$$F_{RECIRC} = \frac{\dot{Q}_{NET} - \dot{Q}_{CLOUD}}{\dot{Q}_{NET}}, \tag{2}$$

where F_{RECIRC} is the recirculation heating fraction, $\dot{Q}_{NET}$ is the total latent heating from all microphysical processes, and $\dot{Q}_{CLOUD}$ is the latent heating associated with cloud droplet nucleation, cloud droplet condensation and evaporation. As it can be seen from Eqn. 2, F_{RECIRC} becomes larger as the processes associated with cloud droplet growth become less important, or as the other processes become more important. The latter processes have been shown to be the dominant process in condensational latent heating for deep tropical convection below the freezing level (Storer and van den Heever 2012). It can also be seen from Eqn. 2 that: (1) if $\dot{Q}_{NET}$ becomes small, then slight variations in cloud latent heating relative to the net latent heating can lead to relatively large values of F_{RECIRC}, and (2) if $\dot{Q}_{CLOUD}$ is more negative than $\dot{Q}_{NET}$ then false positive values of F_{RECIRC} can exist. The recirculation heating fraction is shown in Fig. 4.4h, but has been truncated to where the mean updraft speed is greater than 0.5 m s^{-1} and values of $\dot{Q}_{NET}$ and $\dot{Q}_{CLOUD}$ are both positive in order to isolate the recirculation mechanism and to remove the caveats of the calculation just described. It is clear that F_{RECIRC} is maximized in the region of the updraft close to and just below the freezing level (Fig. 4.4h), which is collocated with the entraining hail hydrometeors (Fig. 4.4a) and the microphysical processes associated with the recirculation mechanism (Figs. 4.4a-f).

It is likely that in addition to the entrainment of hail into the updraft, less buoyant non-updraft air is also being mixed into the updraft that can counteract the positive contribution of latent heating by the recirculation mechanism. Figure 4.4i shows the mean buoyancy distribution in and around the mid-level updraft. From the buoyancy field it can be seen that the peak in positive buoyancy occurs towards the lower portion of the main updraft, centered around 3.5 km AGL, which is due to condensational growth of both cloud and rain water. As rain

condensational growth is included in $\dot{Q}_{NET}$, this peak in positive buoyancy shows up in the F_{RECIRC} field (Fig. 4.4h), however its value is small. Moving higher up in the updraft, it can be seen that the region of largest positive buoyancy is shifted towards the upshear side of the updraft (Fig. 4.4i) and matches well with the location of maximum F_{RECIRC} (Fig. 4.4h). This suggests that the microphysical processes associated with the recirculation mechanism contribute positively to the net buoyancy field in the mid-level updraft.

To see how this mechanism operates for an individual convective cell, Figure 4.5 shows a vertical cross section through a well-organized portion of the squall line (Fig. 4.5a) seven hours into the simulation. From this cross section, the following processes (Fig. 4.5b) can be seen that lead to an enhancement in F_{RECIRC} (Fig. 4.5c): (1) hail is falling into the RIJ from above the freezing level; (2) the falling hail has net condensational growth below the freezing level both within the RIJ and in the upshear flank of the updraft; (3) the melting hail generates rain hydrometeors in the updraft and within the RIJ that are then fluxed into the updraft at ~ 3-3.5 km AGL; (4) due to their slower fall velocity, the ingested rain drops are transported higher into the updraft (i.e. *recirculated*) and can then serve as a source of latent heat by freezing onto hailstones. These processes generate local F_{RECIRC} values up to ~30% (Fig. 4.5c), however positive feedbacks can also potentially invigorate the squall line even more; and will be assessed in Section 4.

It is obvious that ice processes will become more important in generating net positive latent heating at and above the freezing level (Fig. 4.4h) for squall lines, however it is not obvious that ice processes *below the freezing level* can strengthen the updraft through a positive contribution to latent heating (Fig. 4.4h) that enhances buoyancy (Fig. 4.4i) and potentially induces a positive feedback on squall line strength. This is the fundamental role of the

recirculation mechanism, which is summarized in schematic form in Figure 4.6, and will be further analyzed in the next section through sensitivity experiments.

4.4 Sensitivity experiments

Assessing the precise contribution of the recirculation mechanism to the intensity of a simulated squall line is not simple, as it has been shown that microphysics and dynamics within squall lines are intimately connected (e.g. Fovell and Ogura 1988; Ferrier et al. 1995; Adams-Selin et al. 2012a,b; Bryan and Morrison 2012). Systematically turning off processes involved in the recirculation mechanism (e.g. hail riming or vapor deposition onto hail) within the microphysics scheme in order to assess their individual importance does not necessarily isolate cause and effect because of the delicate balances between processes and their nonlinear responses and feedbacks. For example, when simulating a hailstorm that occurred over Germany, Noppel et al. (2010) ran sensitivity simulations that varied the concentration of CCN and the shape of the cloud drop distribution and concluded that the strong coupling between numerous microphysical processes "makes it difficult to forsee, what will happen, when one microphysical parameter is changed." In an effort to show the delicate balances between microphysics and dynamics of a supercell storm, Morrison (2012) performed an ensemble of simulations in which various microphysical processes are turned off and found a "network-like" response for the supercell in which other microphysical processes act to compensate for the excluded process.

In order to isolate the importance of the recirculation mechanism while still realistically preserving all of the microphysical processes and not biasing specific processes, a sensitivity

experiment has been designed that varies the mean diameter of the hail hydrometeor distribution. It was shown in the previous section that the recirculation mechanism stems from the entrainment of hail and rain hydrometeors into the mid-level updraft of a squall line. By altering the size characteristics of hail that will result in changes to both hail and rain microphysics and the position of hail sedimentation relative to the RIJ and mid-level updraft, the recirculation mechanism's importance on squall lines can potentially be assessed. The four experiments that accomplish this task will be presented in this section, and consist of the control simulation (2MOM; see Section 3) and three sensitivity simulations that vary the mean diameter of the hail size distribution between 1 mm (1MM), 5 mm (5MM), and 1 cm (1CM).

4.4.1. Squall line characteristics

To highlight some evolutionary differences and similarities between the four squall lines, Figure 4.7 shows the 1 km AGL simulated reflectivity at three times during the simulations that span the first four hours of the analysis period. For each simulation, it is evident that bowing in the reflectivity field is collocated with strong updraft and anomalously strong RTF flow in the mid-levels, which persists for multiple hours. This indicates that each squall line is well organized (Weisman 1992, 1993) and freely evolving. Relative to the control simulation (2MOM), it can be seen that: (1) squall line propagation is very similar for all simulations; (2) the 1MM simulation shows the most expansive stratiform region and qualitatively looks the most similar to 2MOM; (3) bowing structures are evident for all simulations; and (4) the highest reflectivity occurs with the 1CM simulation, which is due to more large hail reaching the surface,

as reflectivity is strongly dependent on hydrometeor size. From Figure 4.7 it is clear that by simply changing the mean diameter of hail, notable structural differences occur. These differences could be influenced by changes to the cold pool, which alters the dynamics of the squall line according to RKW88, and has also been linked to microphysics by other studies such as Luo et al. (2010), Adams-Selin et al. (2012a,b) and Bryan and Morrison (2012). Therefore, in order to assess the significance of the recirculation mechanism on the intensity of the simulated squall lines, the influence of the cold pool for each squall line will be investigated through the application of RKW Theory. This will help to isolate the impacts of the cold pool from the recirculation mechanism for the squall lines.

Given that the base state shear profile is not varied between simulations, the cold pool propagation speed (C) dominates the C/ΔU variability among the simulations. Traditionally, a theoretical measure of C is used based on density current theory (e.g. RKW88; WR04; Bryan et al. 2006) and is given by (Benjamin 1968)

$$C_B^2 = 2\int_0^H (-B)dz, \tag{3}$$

where C_B represents the cold pool propagation speed based on the theoretical buoyancy calculation, H represents the depth of the cold pool, and B represents the buoyancy defined in (1). Most previous studies also all make use of a free slip bottom boundary condition that allows C_B for squall lines to behave similarly to classical density current theory (e.g. RKW88; WR04; Bryan et al. 2006). However, in reality the lower boundary is not a free slip surface and is not treated as such in the simulations performed here. Thus, C_B will be compared to a direct measure of squall line propagation that is calculated by tracking the location of the gust front in time (C_D).

This calculation most precisely describes the motion of the squall line while including the effects of surface friction, which are implicit for squall lines in reality.

The comparison between C_D and C_B and their respective C/ΔU ratios are shown in Table 4.2 as time and meridional averages. The most obvious difference between C_D and C_B is that C_B is 50 – 60% larger than C_D, which is primarily due to the inclusion of surface drag because the mean wind should act to increase the ground-relative cold pool propagation speed (Moncrieff and Liu 1999; Corfidi 2003). The values of C_B (~ 15-20 m s^{-1} for instantaneous speeds) match well with those in other studies using the Weisman-Klemp sounding (e.g. Weisman and Rotunno 2004; Bryan et al. 2006). In WR04's revisit of RKW88, they showed that when using three-dimensional simulations and calculating ΔU over the lowest 2.5km AGL, squall line intensity is maximized when $C_B/\Delta U$ ~ 1.0-1.7 (see Table 4.1c in WR04). From Table 4.2, it can be seen that the $C_B/\Delta U$ values for the experiments here, which also have the shear within the lowest 2.5 km AGL, fall within this range. However when using $C_D/\Delta U$, the ratios are lower and range from 0.7-1.3, which is not surprising given that surface drag is included in the simulations. In both sets of C calculations, a modest decrease in cold pool speeds is evident as hail size increases (Fig. 4.9), which has also been noted by other numerical studies (Szeto and Cho 1994; van den Heever and Cotton 2004; Adams-Selin et al. 2012a,b). While a trend is evident in cold pool speeds, the C/ΔU ratios are largely similar between simulations and centered within the range where each squall line should be close to its maximum system intensity. For all subsequent analysis, C_D will be used as the metric for cold pool propagation speed.

Based on RKW Theory, the analysis above demonstrates that all these squall lines should be near their maximum system intensity, however changes in cold pool intensity have been

shown to lead to changes in squall line organization (Szeto and Cho 1994; Adams-Selin et al. 2012). Figure 4.8 shows vertical cross sections of the basic fields of system-relative U-wind (relative to C_D), vertical velocity, and pressure perturbation (calculated relative to the pre-squall environment) for all experiments, which have been averaged meridionally with respect to the gust front and temporally. As hail size decreases, the FTR flow strengthens and the RIJ resides closer to the mid-level updraft (compare Figs. 4.8d,g,j). The vertical velocity field also shows similar trends in that as hail size decreases, the mid-level updraft increases and the mesoscale downdraft strengthens (compare Figs. 4.8e,h,k). Upon comparing simulations of a bow echo in which characteristics of graupel were changed to represent hail, similar trends were seen by Adams-Selin et al. (2012a), whereby as the hydrometeors were more graupel-like the bow echo contained stronger updrafts and faster RTF flow. The squall lines of 2MOM and 1MM are the only simulations that have a significant minimum in pressure due to latent heating within the main convective updraft near the freezing level, further indicating that they are the most organized of the group.

As WR04 note, the "optimal" state of squall lines is not clear-cut, as many parameters can define system intensity. Mean precipitation rate (Fig. 4.9a) generally decreases with increasing hail size, and the 1MM and 2MOM produce the most amount of precipitation. Similar trends are seen for total water path (TWP; Fig. 4.9b), except the 2MOM squall line has less TWP than all squall lines from T= 3h to T=4.5h, but still follows the temporal trend of 1MM closely. The time series of meridionally averaged C_D and $C_D/\Delta U$ are shown in Fig. 4.9c. The sensitivity simulations all show a relatively steady mean cold pool speed and associated $C_D/\Delta U$ close to 1, however the 1CM cold pool is consistently slower than the 1MM cold pool by ~ 10%, and the 5MM cold pool does not follow the trend. This indicates that the squall lines are all stable and

near their maximum system intensity according to RKW88, but the 1MM cold pool is indeed stronger.

To better understand how the structure of the squall lines differs between simulations, Figure 4.10 shows horizontally and temporally averaged vertical profiles of various quantities that assess squall line organization and intensity. The line-perpendicular wind (Fig. 4.10a) shows an enhancement of both the RIJ and the FTR flow with decreasing hail size, signifying that as hail size decreases the convective momentum transport is more pronounced. A smooth trend in vertical velocity is also seen (Fig. 4.10b), whereby as hail size decreases the domain-averaged vertical velocity increases systematically through the depth of the troposphere. A similar trend is also evident in total condensate (Fig. 4.10c), however the 2MOM squall line contains smaller amounts of condensate above the freezing level. Throughout most of the troposphere, buoyancy shows little variation between simulations (Fig. 4.10d), except near (1) the freezing level where buoyancy increases with decreasing hail size, and (2) the surface where a slight decrease in buoyancy with smaller hail size is evident supporting the observed cold pool trend (Table 4.2 and Fig. 4.9c). These trends highlight the importance of the ice phase for squall line intensity and organization, which will be discussed in the next sub-section via the recirculation mechanism.

As hail size decreases, the total upward mass flux, MF, increases systematically throughout the troposphere (Fig. 4.10e). Additionally, when the updrafts are sampled for deep convection where $W > 1$ m s^{-1} (Fig. 4.10f) and $W > 2$ m s^{-1} (Fig. 4.10g), the trend also holds, indicating that convective mass flux increases with decreasing hail size. Similarly, the mesoscale convective downdrafts are enhanced as hail size decreases (Fig. 4.10h), highlighting the importance of ice microphysics in overall squall line organization. In order to assess the intensity of the squall line as a whole, the fraction of the domain that satisfied the sampling conditions for

updrafts and downdrafts are plotted below their corresponding Figure 4.(Fig. 4.10i-l). With the exception of $W > 0$ m s^{-1} (Fig. 4.10i), which shows virtually no trend, all updraft and downdraft conditions show a large (up to a factor of ~2) increase in domain coverage with decreasing mean hail size. The trends in both *greater total mass flux* (Figs. 4.10e-g) and *increased domain coverage* of sampling threshold (Figs. 4.10i-k) as hail size decreases indicates consistency regardless of the sampling condition applied. The same trends are seen with the strength of the downdrafts increasing with decreasing hail size (Figs. 4.10h,l).

The latent heating profiles can provide insight into the trends seen in the vertical mass flux (Fig. 4.10m-o). The most significant changes in the net latent heating for the sensitivity experiments occur in the mixed-phase region (Fig. 4.10m), where the sensitivity to hail size is most profound. As hail size decreases, the net latent heating increases. This is likely the cause of the increase in buoyancy for smaller hail sizes (Fig. 4.10d), as the environmental conditions have been held fixed between simulations and increased hydrometeor loading has been found to increase with decreasing hail size, which actually counteracts this trend. Separating net latent heating into its phase components, the latent heat of fusion helps to explain the signature seen in convective downdrafts (Fig 11h,l), where increased melting occurs with smaller hail sizes thus leading to more negative buoyancy (Fig. 4.10n). This is not surprising given the increase in surface area associated with smaller hail hydrometeors, which is the largest factor in melting (van den Heever and Cotton 2004). The latent heat of vaporization (Fig. 4.10o) is predominantly responsible for the trend seen in total latent heating and also shows that above 2 km AGL net condensation increases with decreasing hail size, predominantly near the freezing level. Increased evaporation near the surface is also evident as hail size decreases, which contributes to the increase in cold pool speeds.

The analysis in this sub-section demonstrates that as the mean hail size decreases, the cold pool speed increases by ~ 10%. While the variation in cold pool speed is modest between simulations, the trends seen in various assessments of squall line intensity are more substantial. These trends match well with those seen in microphysical processes near the freezing level that are contributing to increased buoyancy, resulting in stronger squall lines with decreasing hail size. Because consistent trends in both the cold pools and microphysical processes near the freezing level are occurring, a positive feedback is likely assisting squall line intensity. This feedback can be synthesized whereby ice processes (i.e. the recirculation mechanism) are aiding mid-level updraft invigoration that ultimately leads to more precipitation and to stronger downdrafts. This then leads to stronger cold pools, which enhance low-level convective updrafts and provide more supersaturation for hydrometeor growth, thereby providing more latent energy for the recirculation mechanism. This will now be examined in more detail via the recirculation mechanism.

4.4.2. Recirculation mechanism

To illustrate the differences in the recirculation mechanism as hail size is varied, Figure 4.11 shows a single vertical cross section of the microphysical processes and latent heating (F_{RECIRC}) associated with the recirculation mechanism through the location of the maximum mid-level condensate mixing ratio for each simulation (Fig. 4.11a,d,g,j). As hail size increases, multiple trends can be seen in Figure 4.11e,h,k, including: (1) the amount of hail residing in the updraft decreases; (2) the amount of net condensational growth of hail decreases; and (3) horizontal rain flux by the RIJ into the updraft, which serves as an additional source of latent

heating by riming as the rain is lofted towards and above the freezing level by the updraft, decreases. These processes all contribute (though not entirely) to the increase in F_{RECIRC} near the freezing level as hail size decreases (Fig. 4.11f,i,l). Additionally, as hail size increases, the mid-level updraft narrows (Fig 11f,i,l), which corresponds well with the trends seen in domain updraft coverage (Fig 10). The narrowing of the convective updraft is not due to condensate loading as there is a consistent trend of increasing hail and rain mass with smaller hail size (Fig. 4.11e,h,k). These trends all combine to show that the recirculation mechanism is helping to increase the net latent heating that partially drives the mid-level dynamics of the squall line.

By averaging each simulation both meridionally along the gust front and temporally, Figure 4.12 shows a comprehensive assessment of the recirculation mechanism and how it becomes more important with decreasing hail size. Following similar logic as with the control experiment (2MOM; Section 3b), as hail size decreases (Figure 4.12): (1) more hail and rain is fluxed into the mid-level updraft; (2) net condensation onto rain and hail increases *below the freezing level*; (3) net riming onto hail increases near the freezing level; and (4) F_{RECIRC} increases near the freezing level in the mid-level updraft. The F_{RECIRC} is estimated to account for up to ~ 20%, 26%, 10%, and 0% of the net latent heating near the freezing level of the updraft for the 2MOM, 1MM, 5MM, and 1CM squall lines, respectively (Fig. 4.12). While the spatial extent of the region within the updraft that is most directly impacted by F_{RECIRC} is not large, its influence on squall line intensity has been shown to be large, as it acts as a positive feedback mechanism. This can be summarized as follows: (1) hail and rain is ingested into the mid-level updraft and helps to invigorate vertical velocity through microphysically-induced enhancement of buoyancy; (2) the increase in convective mass flux combined with the entrained hydrometeors helps to loft more liquid condensate higher above the freezing level, potentially enhancing the latent heat

released in association with freezing, thereby further enhancing buoyancy and increasing ice mass; (3) the increase in ice mass enhances convective downdrafts that strengthen the cold pool and simultaneously enhance the low-level updrafts; and (4) the stronger updrafts enhance supersaturation and produce more condensate that further facilitates the recirculation mechanism.

4.5. Summary

Four simulations of an idealized squall line have been performed using RAMS that show the importance of a microphysical recirculation mechanism and its role in aiding squall line invigoration. First, a control simulation of a squall line using two-moment microphysics for all eight hydrometeor species showed the existence of a recirculation mechanism that begins with hail hydrometeors being ejected upshear from the main convective updraft. As the hail hydrometeors descend below the freezing level, they encounter the RIJ of the squall line that advects them and melted rainwater back towards the mid-level updraft. The hail and rain become entrained into the upwind side of the updraft *below the freezing level*, where condensation and fusion onto the additional hail and rain hydrometeors promote extra latent heating that in turn enhances buoyancy. The net effect of the recirculation mechanism is to locally enhance latent heating such that it overcompensates the entrainment of negatively buoyant processed air, leading to buoyancy enhancement and subsequent updraft invigoration.

As microphysics and dynamics in squall lines are intimately connected (Fovell and Ogura 1988; Ferrier et al. 1995; Adams-Selin et al. 2012; Bryan and Morrison 2012), a sensitivity experiment was designed that would most effectively isolate the importance of the recirculation mechanism for squall lines. Three additional sensitivity simulations of a squall line were

performed using single-moment microphysics in which the mean diameter of the hail hydrometeor distribution was varied. Analysis of the sensitivity experiments can be briefly summarized as follows.

(1) C/ΔU ratios indicate that the squall lines are all near their maximum system intensity, while the mean squall line propagation speed increases by up to ~10% as hail size decreases.

(2) With smaller hail sizes, the vertical structure of the squall lines have a better-defined RIJ, stronger FTR flow, and stronger mesoscale updrafts and downdrafts.

(3) As hail size decreases, precipitation increases along with TWP.

(4) Both convective and total upward mass flux increase with smaller hail sizes.

(5) Net latent heating, especially near the freezing level, increases with smaller hail sizes, leading to greater buoyancy.

(6) The increased buoyancy near the freezing level can be attributed to a positive feedback between the recirculation mechanism and the cold pool, whereby the recirculation mechanism strengthens the mid-level updraft, which promotes increased frozen condensate that enhances the convective downdraft and strengthens the cold pool. The cold pool then enhances the low-level updraft and produces greater supersaturation and subsequent condensation, thereby facilitating the recirculation mechanism.

The experiments presented in this paper highlight the importance of the ice phase in numerically simulated squall lines. It is shown that through the recirculation mechanism, a stronger squall line can be sustained. While changes in cold pool intensity assist in strengthening the squall line, the greatest variations among the simulations occurred near the freezing level where the recirculation mechanism is present.

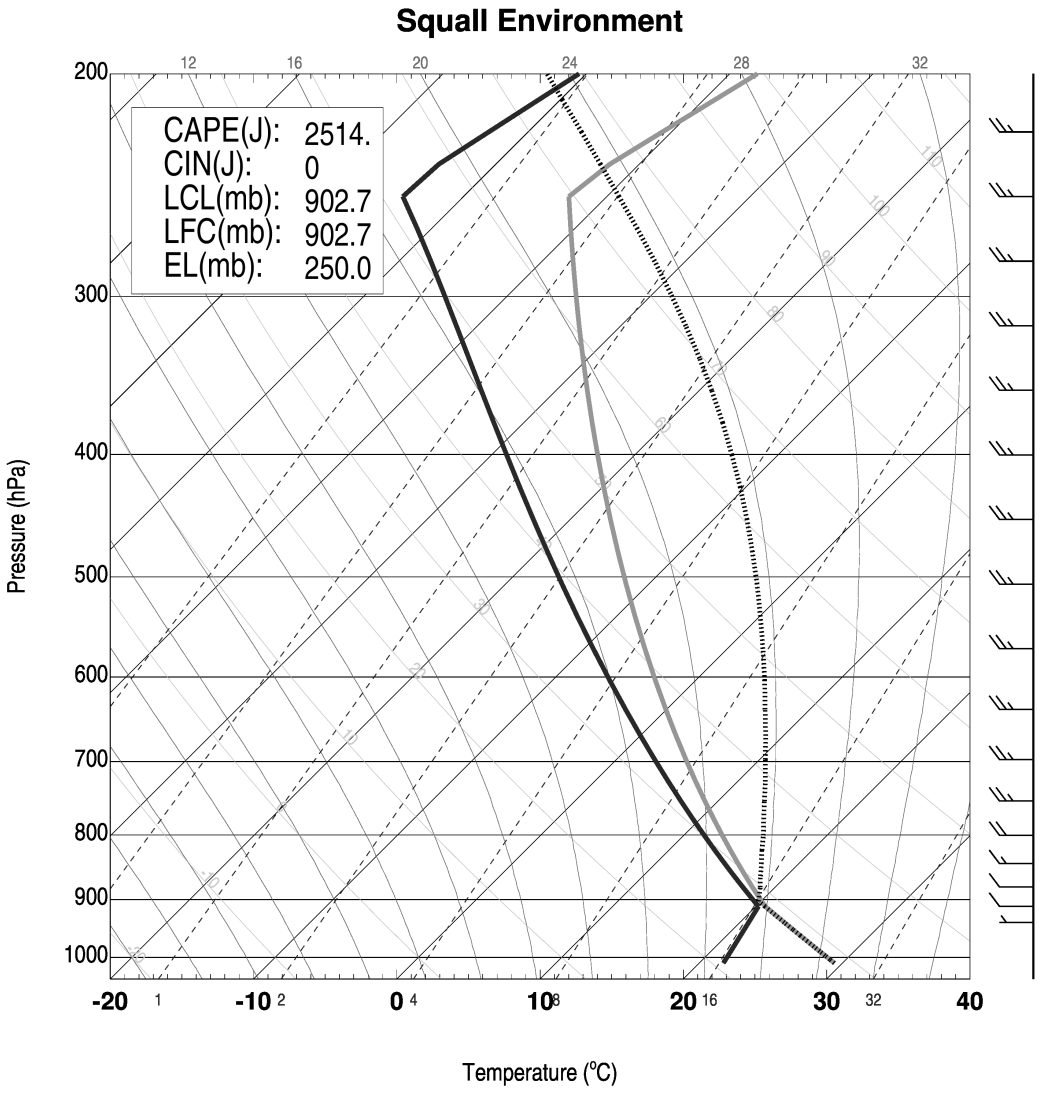

Figure 4.1. Horizontally homogeneous environmental conditions initialized for the squall line. The thick grey line is the temperature profile and the thick black is the moisture profile. The thick dashed line is the moist adiabatic parcel curve. Following Weismann and Klemp (1982).

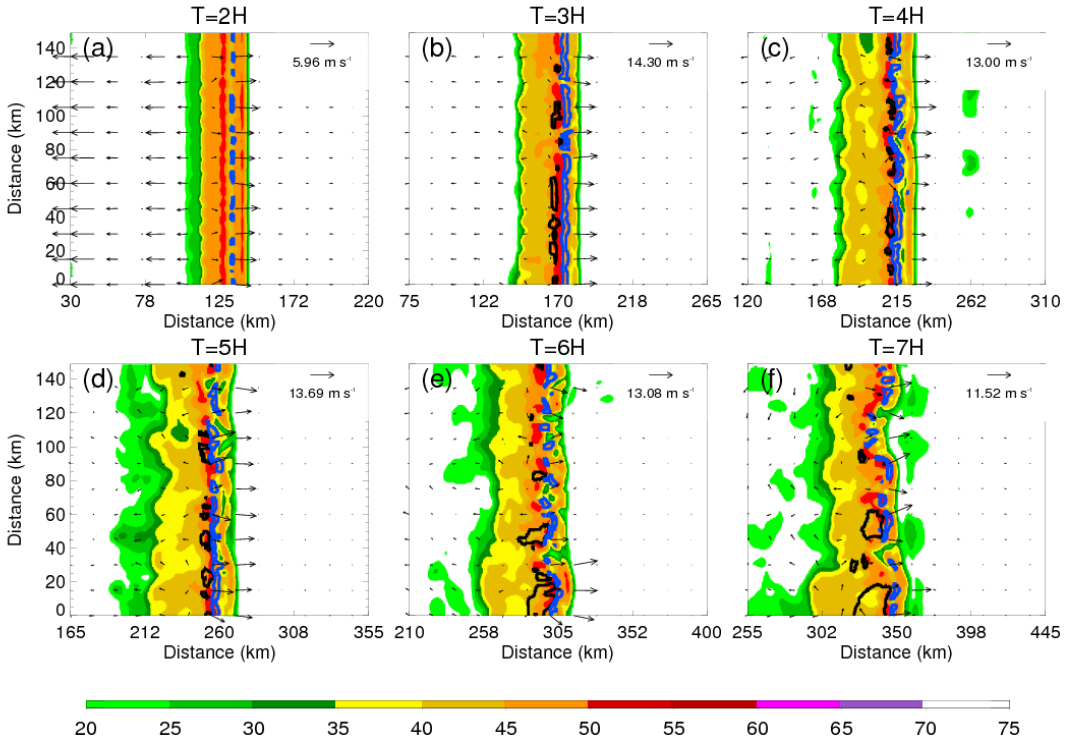

Figure 4.2. Simulated base radar reflectivity (dBZ) of 2MOM at 1 km AGL using the methodology of Matrosov (1999) for: (a) T=2h; (b) T=3h; (c) T=4h; (d) T=5h; (e) T=6h; and (f) T=7h into the simulation. The surface winds are shown (vectors) along with the maximum surface wind reference vector in the upper-right corner for each time. Two-sigma standard deviation anomalies of U-wind at 3.5 km AGL (black contours) and updraft speeds of 5 m s^{-1} (blue contours) are also shown.

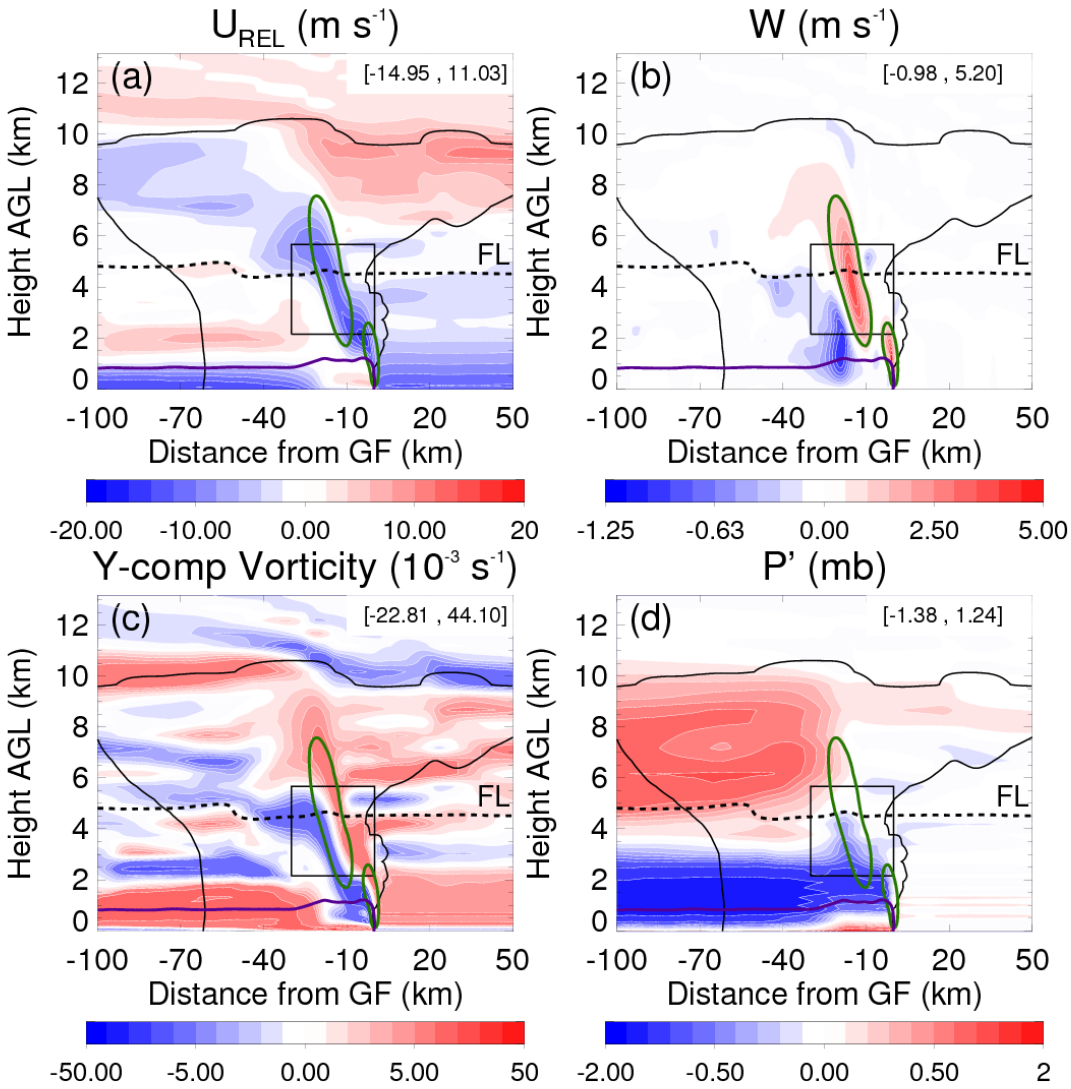

Figure 4.3. Control squall line from simulation hours 3-7 that has been temporally and meridionally averaged along the gust front. Each vertical cross section is expressed as a horizontal distance from the gust front (X-axis) and a vertical distance AGL (Y-axis). Shown on each cross section is the squall line cloud boundary [thick black line; 0.05 g kg^{-1} total condensate], the freezing line [dashed black line], the cold pool boundary [thick purple line; -0.05 m^2 s^{-2} following Tompkins (2001)], the 1 m s^{-1} updraft region [thick green line], a box centered over the mid-level updraft that is the domain shown in Figure 4.4, and [min, max] values for the shaded quantities of: (a) system-relative U-component wind (m s^{-1}); (b) vertical velocity (m s^{-1}); (c) y-component relative vorticity (10^{-3} s^{-1}); and (d) pressure perturbation (hPa).

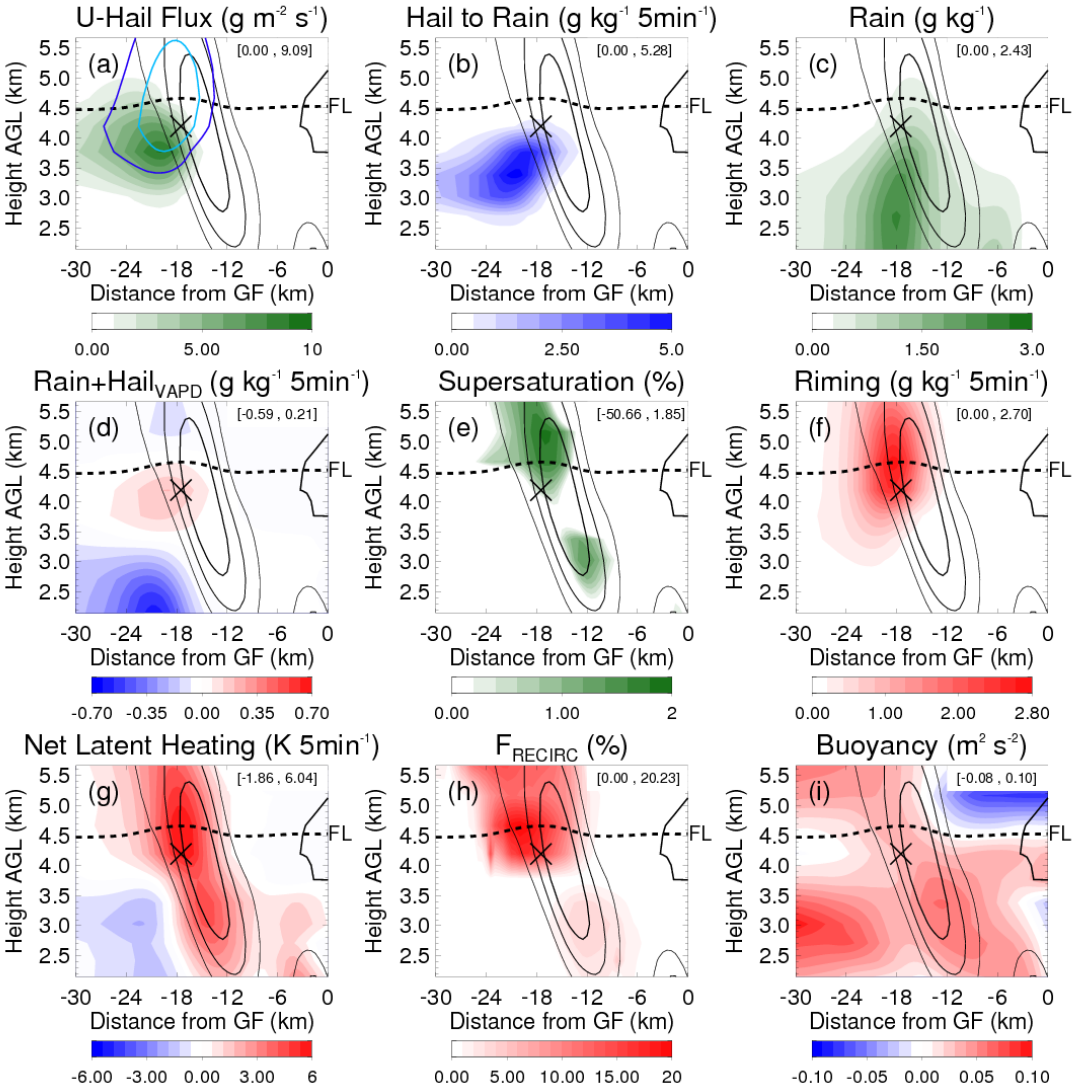

Figure 4.4. Same as Figure 4.3, except the domain shown is centered over the recirculation mechanism and can be seen relative to the entire squall line as the box in Figure 4.3. The marker near the center of each Figure 4.(X) is for a point of reference between the figures. The black lines in the center of each image are the 1, 2, and 3 m s^{-1} updraft contours, the dashed line is the freezing level, the thick black contour at the right edge of each image is cloud boundary, and the shaded contours are: (a) positive zonal flux of hail condensate (g m^{-2} s^{-1}) with hail mixing ratios contoured [0.5 (dark blue) and 1.0 (light blue) g kg^{-1}]; (b) ice to rain conversion mixing ratio averaged as five minute differences (g kg^{-1} $5min^{-1}$); (c) rain mixing ratio (g kg^{-1}); (d) vapor deposition onto hail and rain hydrometeors expressed as a mixing ratio averaged over five minute differences (g kg^{-1} $5min^{-1}$); (e) supersaturation (%); (f) total riming expressed as a mixing ratio averaged as five minute differences (g kg^{-1} $5min^{-1}$); (g) total latent heating minus total latent cooling (K $5min^{-1}$); (h) net latent heating due to the recirculation mechanism (Eqn. 2); and (i) buoyancy (m^2 s^{-2}).

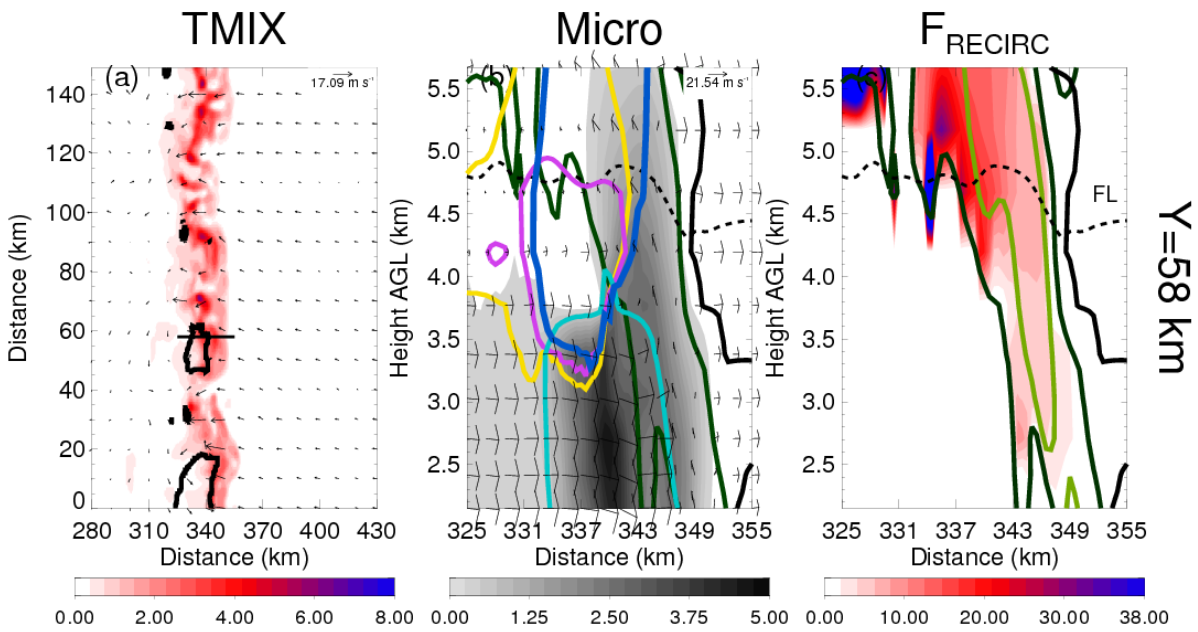

Figure 4.5. Plan-view cross-section of total condensate (shaded; a,d,g) and a vertical cross sections through an organized segment of the squall line at Y=58km. The location of the vertical cross section is depicted by the black horizontal line in (a). Rain mixing ratio (g kg^{-1}; shaded), hail mixing ratio (0.5 g kg^{-1}; blue contour), riming of rain by hail (0.5 g kg^{-1} $5min^{-1}$; yellow contour), net vapor deposition of hail (0.05 g kg^{-1} $5min^{-1}$; magenta contour), horizontal rain flux (0.05 g m^{-2} s^{-1}; light blue contour), U-W wind vectors, 1 m s^{-1} vertical velocity (dark green contour), the freezing level (dashed), and cloud boundary (thick black) are shown in (b). The recirculation heating fraction (shaded), 1 m s^{-1} (dark green contour) and 5 m s^{-1} (light green contour) vertical velocity, the freezing level (dashed), and cloud boundary (thick black) are shown in (c).

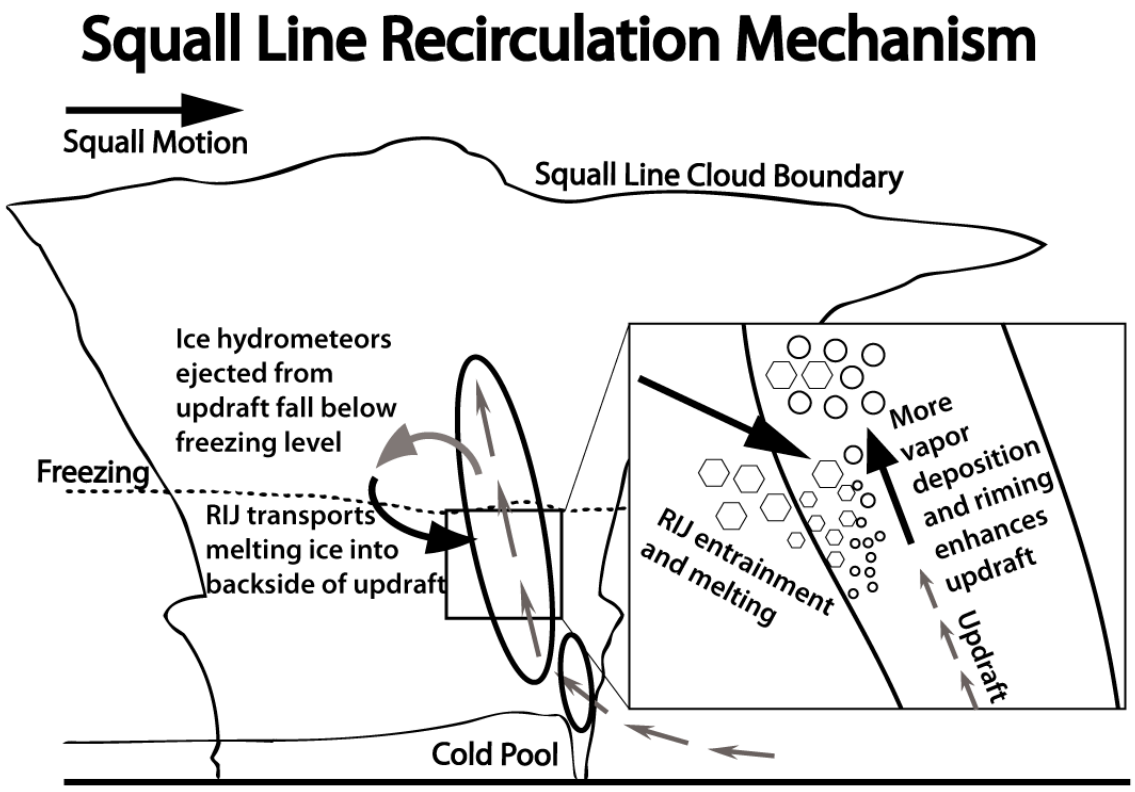

Figure 4.6. Idealized schematic showing the microphysical mechanism aiding enhancement of the mid-level updraft of a squall line. A view of the processes occurring near the freezing level is shown within the box in the right half of the schematic.

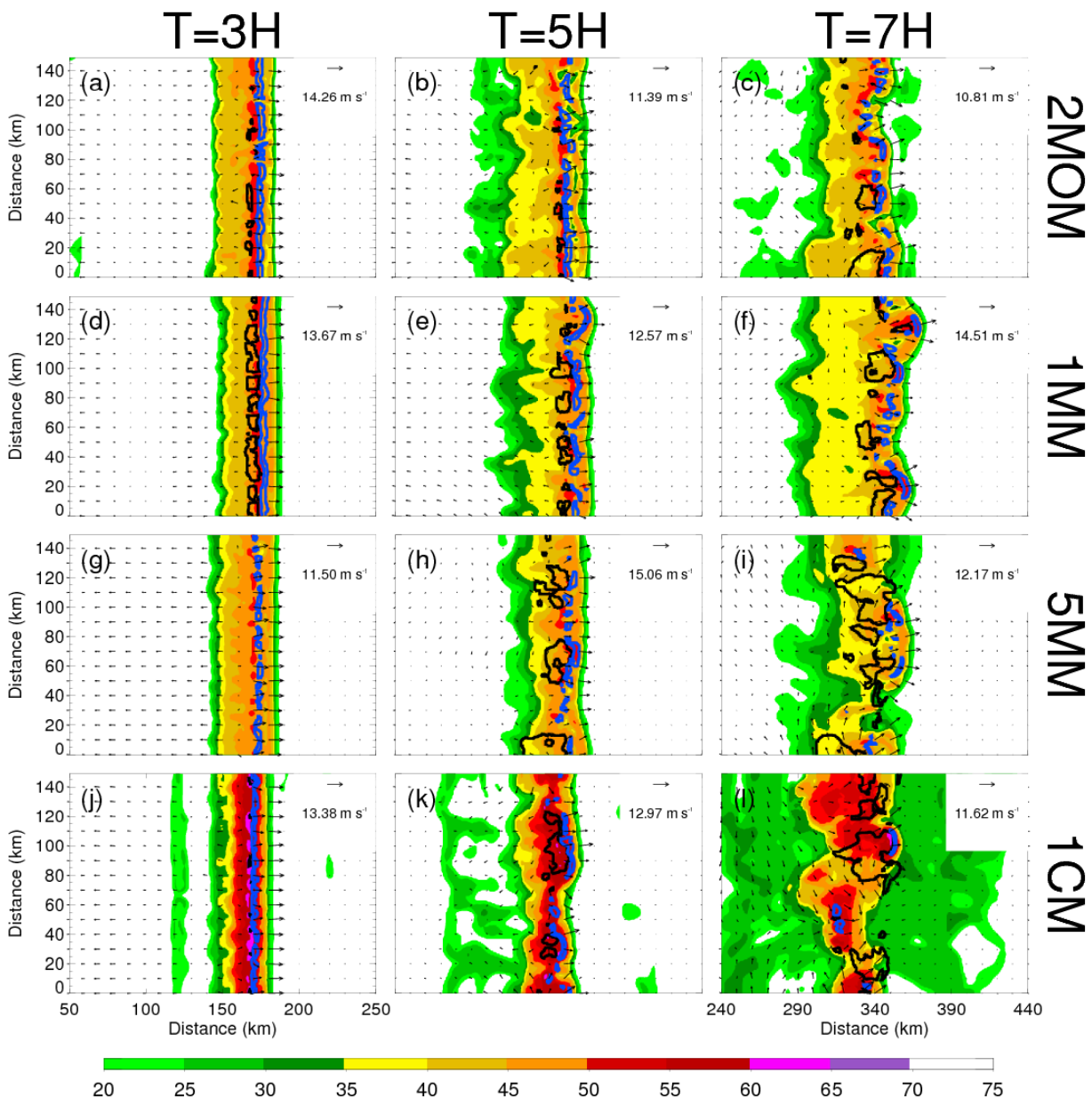

Figure 4.7. Simulated base radar reflectivity (dBZ; Matrosov 1999) of 2MOM (a-c), 1MM (d-f), 5MM (g-i), and 1CM (j-l) at 1 km AGL for: (a,d,g,j) T=3h; (b,e,h,k) T=5h; and (c,f,i,l) T=7h into the simulation. The surface winds are shown (vectors) along with the maximum surface wind reference vector in the upper-right corner for each image. Two-sigma standard deviation anomalies of U-wind at 3.5 km AGL (black contours) and updraft speeds of 5 m s^{-1} (blue contours) are also shown.

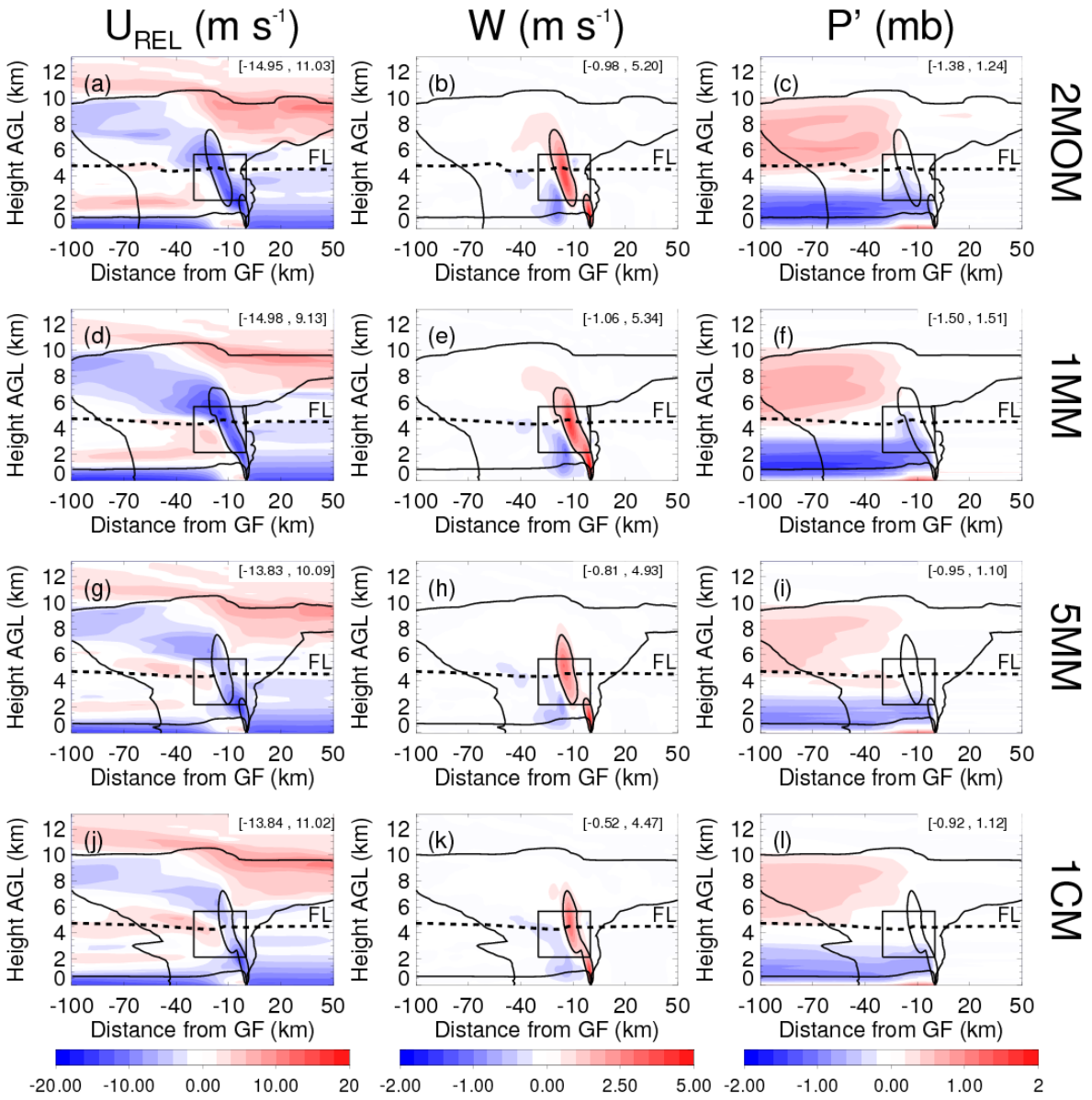

Figure 4.8. Gust front and temporally averaged for 2MOM (a-c), 1MM (d-f), 5MM (g-i), and 1CM (j-l) squall line from simulation hours 3-7. Each vertical cross section is expressed as a horizontal distance from the gust front and a vertical distance above ground level (AGL). Shown on each cross section is the squall line cloud boundary [thick black line; 0.05 g kg^{-1} total condensate], the freezing line [dashed black line], the cold pool boundary [thin black line; -0.05 m^2 s^{-2} following Tompkins (2001)], the 1 m s^{-1} updraft region [thin black line], a box centered over the mid-level updraft that is the domain shown in Figure 4.12, and [min, max] values for the shaded quantities of: (a,d,g,j) system-relative U-component wind (m s^{-1}); (b,e,h,k) vertical velocity (m s^{-1}); and (c,f,i,l) pressure perturbation (mb).

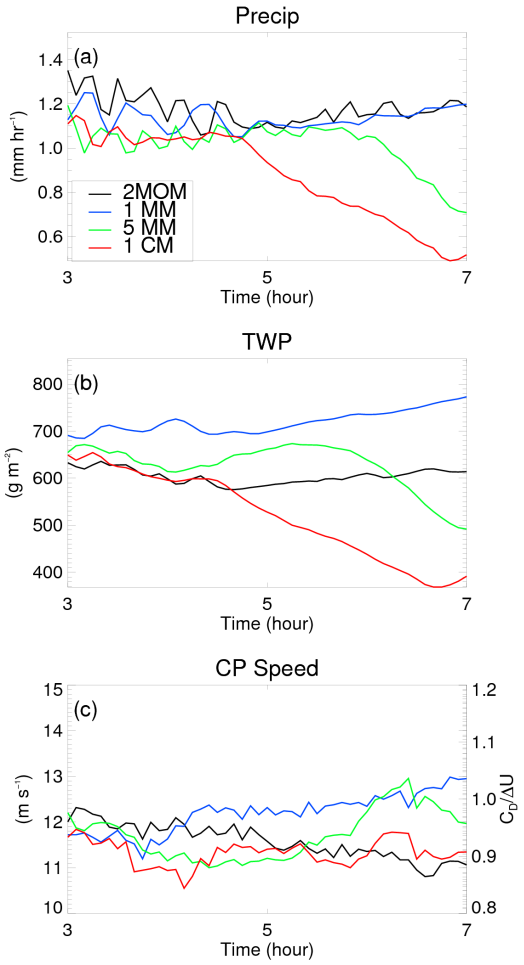

Figure 4.9. The time evolution of horizontally averaged plots of: (a) surface precipitation; (b) total water path; and (c) cold pool speed (C_D) with its corresponding $C_D/\Delta U$ values. The legend indicates the respective simulations of 2MOM, 1MM, 5MM, and 1CM.

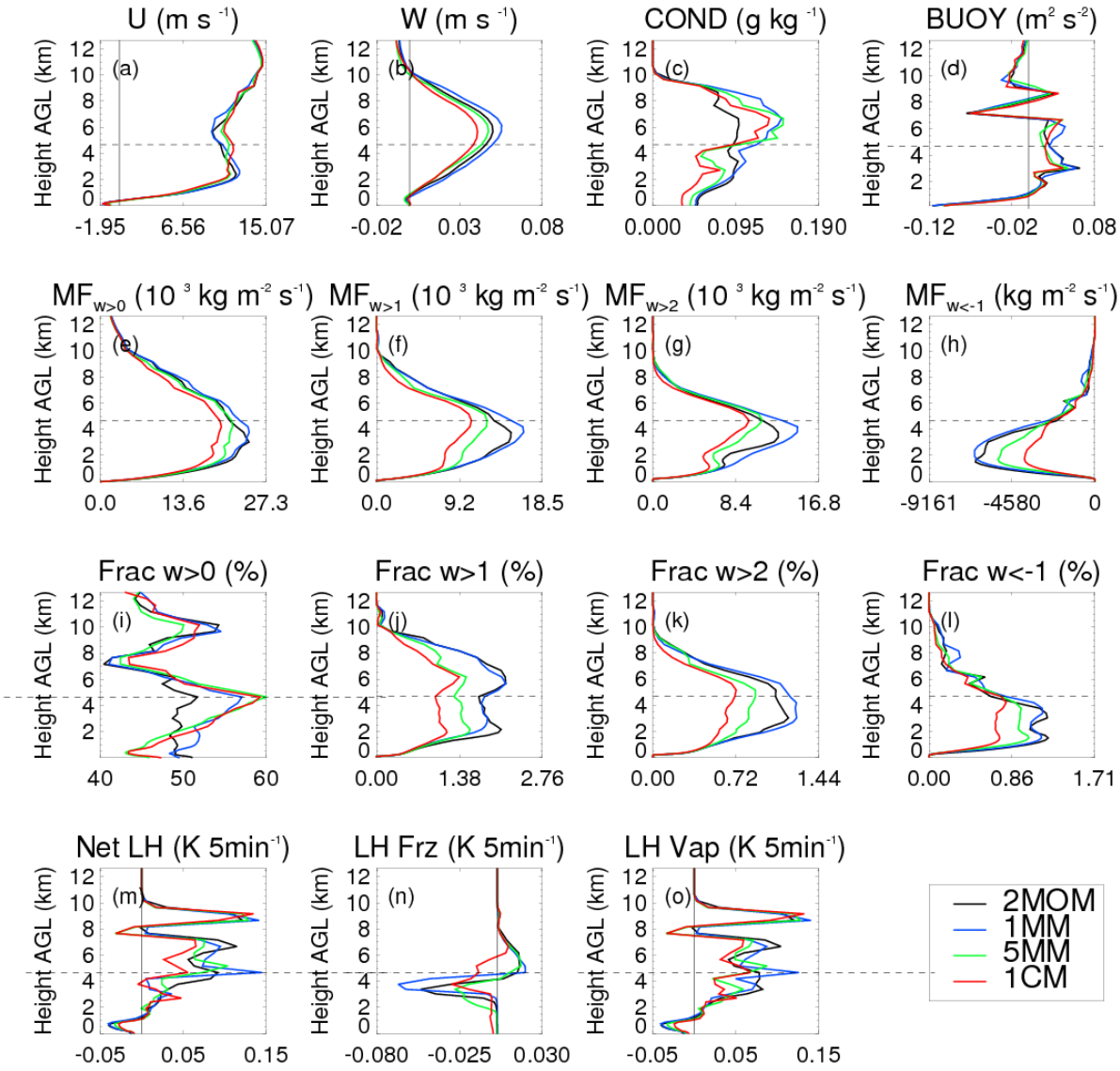

Figure 4.10. Horizontally-averaged and temporally averaged (between hours 3-7) vertical profiles of: (a) U-wind; (b) vertical velocity; (c) total condensate mixing ratio; (d) buoyancy; (e) total vertical mass flux; (f) total convective mass flux sampled where vertical velocity is greater than 1 m s^{-1}; (g) total convective mass flux sampled where vertical velocity is greater than 2 m s^{-1}; (h) total downdraft vertical mass flux sampled where vertical velocity is less than 1 m s^{-1}; (i) the fraction of the domain satisfied by (e); (j) the fraction of the domain satisfied by (f); (k) the fraction of the domain satisfied by (g); (l) the fraction of the domain satisfied by (h); (m) net latent heating; (n) net latent heat of fusion; and (m) net latent heat of vaporization. The legend indicates the respective simulations of 2MOM, 1MM, 5MM, and 1CM.

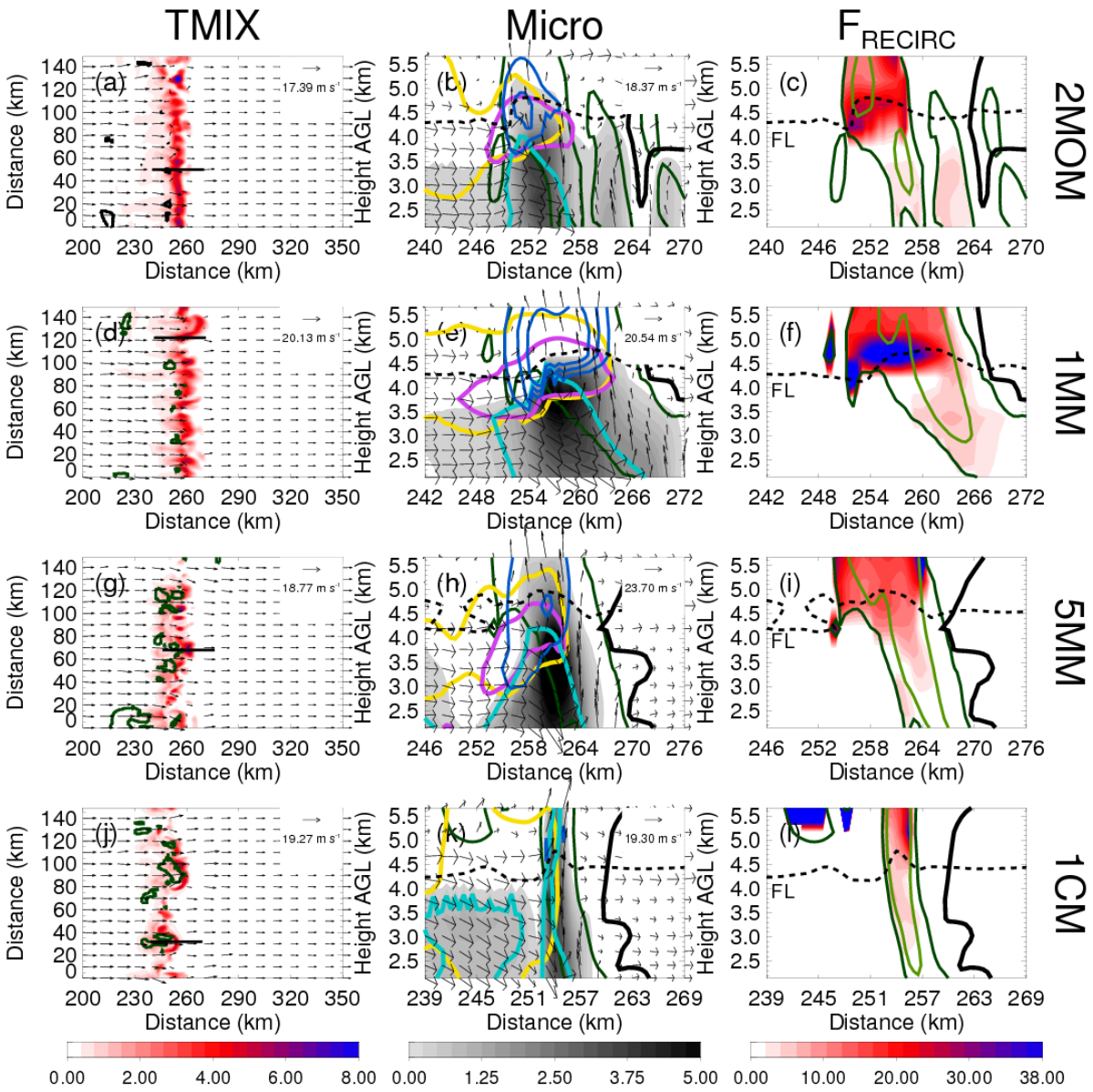

Figure 4.11. Plan-view cross-sections of total condensate (shaded; a,d,g,j) and vertical cross sections through the maximum value of 4 km AGL total condensate: (b-c) 2MOM; (e-f) 1MM; (h-i) 5MM; and (k-l) 1CM. The location of each vertical cross section is depicted by the black horizontal line in (a), (d), (g), and (j). Rain mixing ratio (g kg^{-1}; shaded), hail mixing ratio (0.5 g kg^{-1}; blue contour), riming of rain by hail (0.5 g kg^{-1} $5min^{-1}$; yellow contour), net vapor deposition of hail (0.05 g kg^{-1} $5min^{-1}$; magenta contour), horizontal rain flux (0.05 g m^{-2} s^{-1}; light blue contour), U-W wind vectors, 1 m s^{-1} vertical velocity (dark green contour), the freezing level (dashed), and cloud boundary (thick black) are shown in (b), (e), (h), and (k). The recirculation heating fraction (shaded), 1 m s^{-1} (dark green contour) and 5 m s^{-1} (light green contour) vertical velocity, the freezing level (dashed), and cloud boundary (thick black) are shown in (c), (f), (i), and (l).

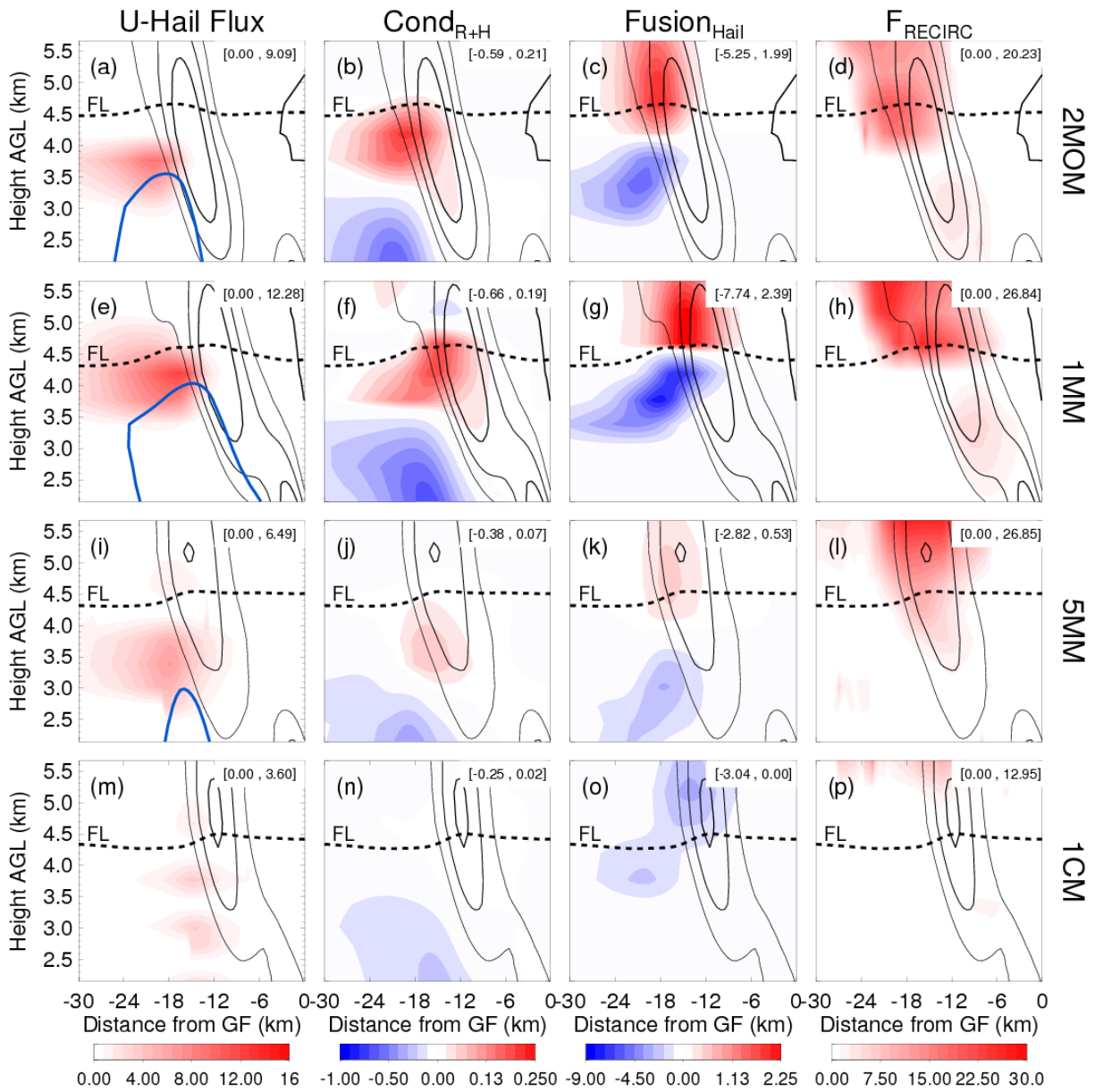

Figure 4.12. Gust front and temporally averaged for 2MOM (a-c), 1MM (d-f), 5MM (g-i), and 1CM (j-l) squall line from simulation hours 3-7. Each vertical cross section is expressed as a horizontal distance (X-axis) from the gust front and a vertical distance AGL (Y-axis). The domain shown is centered over the recirculation mechanism and can be seen relative to the entire squall line in Figure 4.8. The black lines in the center of each image are the 1, 2, and 3 m s^{-1} updraft regions, the dashed line is the freezing level, the thick black contour at the right edge of some images is cloud boundary, and the shaded contours are: (a,e,i,m) rear-to-front flux of hail condensate (g m^{-2} s^{-1}); (b,f,j,n) net condensation of rain and hail averaged as five minute differences (g kg^{-1} $5min^{-1}$); (c,g,k,o) net fusion of hail (g kg^{-1} $5min^{-1}$); and (d,h,l,p) net latent heating due to the recirculation mechanism (Eqn. 2). The blue contours in (a), (e), (i), and (m) is the rear-to-front flux of rain condensate (10 g m^{-2} s^{-1}).

Table 4.1. The microphysical setup for each experiment, where "2" represents the use of two-moment microphysics (prognostic for mass mixing ratio and number concentration) and "1" represents one-moment microphysics (prognostic for mass mixing ratio). The values within the parenthesis refer to the mean diameter (in mm) of the species and are only present when using one-moment microphysics for that species. The shaded cells highlight the sensitivity experiments.

Experiment	Cloud	Drizzle	Rain	Pristine Ice	Snow	Aggregates	Graupel	Hail
CONTROL (2MOM)	2	2	2	2	2	2	2	2
1MM	2	2	1 (3)	2	1 (3)	1 (3)	1 (3)	1 (1)
5MM	2	2	1 (3)	2	1 (3)	1 (3)	1 (3)	1 (5)
1CM	2	2	1 (3)	2	1 (3)	1 (3)	1 (3)	1(10)

Table 4.2. Temporal and meridional average values of C_B, C_D, $C_B/\Delta U$, and $C_D/\Delta U$ between hours 3-7 for each simulation.

Experiment	C_B	C_D	$C_B/\Delta U$	$C_D/\Delta U$
CONTROL (2MOM)	18.36	11.35	1.47	0.91
1MM	18.73	11.95	1.50	0.96
5MM	17.61	11.48	1.41	0.92
1CM	16.31	11.09	1.30	0.89

CHAPTER 5: SIMULATED DENSITY CURRENTS BENEATH EMBEDDED STRATIFIED LAYERS[2]

5.1. Introduction

Cold pools have long been qualitatively compared to density currents, however Charba (1974) was the first to quantitatively relate an observed thunderstorm outflow to a laboratory-produced density current. Since then there have been numerous other studies (Droegemeier and Wilhelmson 1985a,b, 1987; Xu 1992; Liu and Moncrieff 1996a, b, 2000, Simpson 1997; Xue 2002; Engerer et al. 2008), both observational and modeling, which have focused on the generation and complexities of these atmospheric density currents. This study aims to build on previous theoretical density current research to further our knowledge of cold pool characteristics within observed atmospheric environments.

It has been previously demonstrated that in addition to shear (Xu 1992; Liu and Moncrieff 1996a,b; Xu et al. 1996), the stability of the ambient environment plays a large role in the propagation and structure of density currents (Thorpe et al. 1980; Droegemeier and Wilhelmson 1985; Bischoff-Gauss and Gross 1989; Raymond and Rotunno 1989; Hasse and Smith 1989; Jin et al. 1996; Liu and Moncrieff 1996a, 1996b, 2000). Theoretical modeling studies of density currents propagating within complex thermodynamic environments have been performed in order to replicate realistic atmospheric environments. Thorpe et al. (1980) simulated density currents propagating within a neutral environment beneath a deep stably

[2]

stratified environment thus representing a daytime boundary layer. Conversely, Jin et al. (1996) examined density currents within stably stratified environments beneath a neutral layer, representing the nighttime boundary layer. Additionally, Liu and Moncrieff (2000) (herein referred to as LM2000) used a numerical model to analyze how the density current head height and propagation speed are modulated within ambient stratification regimes that represent typical atmospheric environments. In their investigation they simulated three environmental regimes: (i) a stably stratified layer underneath deep, neutrally stratified flow; (ii) a neutrally stratified layer underlying a deep, stably stratified flow; and (iii) a continuously stratified atmosphere. They find that case (i) decreases the height of the density current and increases the propagation speed with increasing stratification; case (ii) reduces density current height and its propagation speed with increasing stratification; case (iii) demonstrates similar responses to case (ii).

This paper focuses on testing a fourth regime in which a neutrally stratified atmosphere contains an embedded, vertically thin, stably stratified layer (Figure 5.1), an environment that is typically associated with severe convection. While the regime examined in this paper is principally different than each experiment of LM2000, this regime is most closely related to the LM2000 case (ii) (herein referred to as LM2000ii) as for both of these experiments the density current propagates within the neutrally stratified layer below the stable layer, and the layer overlying the density current is stably stratified. This provides similar environmental controls on the dynamics of the density current. The sole difference between the regime examined here and LM2000ii is the depth of the overlying stably stratified layer, in that LM2000ii contains a deeply stratified layer from 1 km AGL to model top (15 km) while this research examines the impacts of a vertically thin (1 km) stratified layer. The inclusion of the vertically thin stable layer requires an additional neutral layer above the stable layer. Thus the atmospheric environment

investigated here is one of a neutral layer, overlaid by a thin stably stratified layer, which in turn is overlaid by a neutral layer as shown in Figure 5.1. This setup allows for an investigation of the sensitivity of the density current characteristics on the depth and strength of the stable layer, and therefore extends the LM2000 study to further storm environments.

The environmental regime investigated here is often observed in pre-squall line environments where high convective available potential energy (CAPE) and a convective inhibition (CINH) layer exist (Schmidt and Cotton 1989; Smith and Gall 1989; Bryan and Parker 2010). An example of this can be seen in Figure 5.8b of Bryan and Parker (2010), which was generated using radiosonde data 74 minutes before the passage of a squall line. In Figure 5.8b of Bryan and Parker (2010) three distinct environmental layers are evident that can be characterized by (1) low-level neutral stratification from the surface to ~ 800 hPa; (2) shallow stable stratification from ~ 800 hPa to ~ 700 hPa; and (3) upper level neutral stratification from ~ 700 hPa to ~ 500 hPa. These three environmental layers are synonymous to the environment simulated in this experiment (Figure 5.1). Additionally, supercell tornadogenesis is often observed to occur within environments that contain CINH and high CAPE (Davies 2004). Ziegler et al. (2010) investigated the role that stable layers atop neutrally stratified boundary layers play in supercell tornadogenesis. They modeled a tornadic supercell that propagated within a relatively cold, yet neutrally stratified, boundary layer beneath a vertically thin stable layer. In their modeling experiments it was found that an accelerated retrograding motion of the forward-flank outflow boundary was instrumental in the demise of the supercell. The overlying stable layer could have influenced the propagation speed of the outflow boundary.

As severe weather is often observed within environments containing a thin stably stratified layer, it is important to obtain an understanding of cold pool propagation within such

environments. Therefore, this study examines the role a thin stable layer embedded within a neutrally stratified environment plays on cold pool structure and propagation characteristics by performing sensitivity experiments in which the height and strength of a 1 km deep stable layer are varied. It is hypothesized that altering the depth from a deeply stratified atmosphere (as in LM2000ii) to a vertically thin stratified layer (this experiment) will reverse the trend of the cold pool propagation speed seen in LM2000ii, and that propagation speeds will increase with increasing layer stability. The following section briefly describes the model used for this study and the experiment setup. The third section presents and discusses the results of this study and the fourth section provides a brief summary of the experiment results.

5.2. Methods

5.2.1. The model

The numerical model used for the experiments conducted here includes the same model physics as described by Droegemeier and Wilhelmson (1987), and is thus similar to the model used by LM2000 (Clark 1977). The quasi-compressible, non-hydrostatic, anelastic equations employed are (Droegemeier and Wilhelmson 1987):

$$\frac{\partial u}{\partial t} = -u\frac{\partial u}{\partial x} - w\frac{\partial u}{\partial z} - c_{p_d}\overline{\theta}\frac{\partial \pi'}{\partial x} + \frac{\partial}{\partial x}\left(K_{mx}\frac{\partial u}{\partial x}\right) + \frac{\partial}{\partial z}\left(K_{mz}\frac{\partial u}{\partial z}\right) \qquad (1)$$

$$\frac{\partial w}{\partial t} = -u\frac{\partial w}{\partial x} - w\frac{\partial w}{\partial z} - c_{p_d}\bar{\theta}\frac{\partial \pi'}{\partial x} + g\frac{\theta'}{\bar{\theta}} + \frac{\partial}{\partial x}\left(K_{mx}\frac{\partial w}{\partial x}\right) + \frac{\partial}{\partial z}\left(K_{mz}\frac{\partial w}{\partial z}\right) \quad (2)$$

$$\frac{\partial \theta'}{\partial t} = -u\frac{\partial \theta'}{\partial x} - w\frac{\partial \theta'}{\partial z} - w\frac{\partial \bar{\theta}}{\partial z} + \frac{\partial}{\partial x}\left(K_{hx}\frac{\partial \theta'}{\partial x}\right) + \frac{\partial}{\partial z}\left(K_{hz}\frac{\partial \theta'}{\partial z}\right) \quad (3)$$

$$\frac{\partial \pi'}{\partial t} = -\frac{\bar{c}_s^2}{\bar{\rho}c_{p_d}\bar{\theta}^2}\left(\frac{\partial \bar{\rho}\theta u}{\partial x} + \frac{\partial \bar{\rho}\theta w}{\partial z}\right) + \frac{\partial}{\partial x}\left(K_{hx}\frac{\partial \pi'}{\partial x}\right) + \frac{\partial}{\partial z}\left(K_{hz}\frac{\partial \pi'}{\partial z}\right) \quad (4),$$

where a prime (‘) denotes the perturbation from the base state and a bar ($\bar{}$) denotes the base state variable, which is only a function of height. Equations (1) – (4) are discretized for this limited-domain model to prognose on u (horizontal wind), w (vertical wind), θ (temperature), and π (Exner perturbation function). In Eqn. (4), c_{p_d} is the specific heat capacity for dry air and $\bar{c}_s$ is the speed of sound, which has been set to 100 m s^{-1} following the methodology of Droegemeier and Wilhelmson (1987). The coefficients K_{mx}, and K_{mz}, are the horizontal and vertical computational diffusion coefficients for the momentum equations, and K_{hx}, and K_{hz}, are the horizontal and vertical computational diffusion coefficients for the scalar equations.

The 2-D numerical grid utilizes the Arakawa-C staggering and is 4000 x 160 points in the horizontal and vertical directions, respectively. Grid spacing of 100 m in the horizontal and 50 m in the vertical has been utilized in order to keep the model setup as similar as possible to that of LM2000. This results in a grid domain size of 400 km by 8 km. Sensitivity testing was performed on the vertical depth of the domain and a higher model top did not change the

solution. The time step used is 0.125 seconds and the model is run for 2000 s. The 2nd order leapfrog advection scheme and a Robert-Asselin filter are utilized. Periodic lateral boundary conditions are applied, however the numerical domain used for all of these simulations is sufficiently large such that the density current does not interact with the lateral boundaries during the entire analysis time period. The model top is a rigid lid with no mass transport through the upper boundary and the bottom boundary is a free-slip boundary, similar to LM2000.

This simple model allows for the isolation of key dynamical processes in the analysis of density currents, however the grid spacing employed has been shown to have errors of up to 4% when compared against a reference solution of 25 m grid spacing (Straka et al. 1993), and the slab-symmetric coordinate system used here is known to slightly underperform an axi-symmetric coordinate system when simulating density currents (Straka and Anderson 1993). In spite of the weak, potential errors this may introduce, this grid spacing and coordinate system are utilized in order to maintain model setups as similar to LM2000 as possible, thus reducing the uncertainties in output associated with differences in the models used.

The density current is initialized by allowing a cold bubble to descend within an initially motionless base state environment. The cold bubble, shaped like the top half of an ellipse with the semi-major axis located at the surface, contains a maximum thermal perturbation of -15 K that is sine-smoothed to a horizontal radius of 4 km and a vertical depth of 6 km. Once time integration commences, the negatively buoyant air within the bubble descends and spreads out laterally, generating two identical density currents moving in opposite directions. The density currents exhibit maximum thermal perturbations of -6K, which compare well with observed thunderstorm outflow thermal perturbations (Engerer et al. 2008).

Ten simulations of the cold bubble are performed. The control experiment contains an isentropic atmosphere with no stably stratified layer. In the nine sensitivity experiments the height AGL and strength of the embedded stably stratified layer are varied through modifications to the base state θ-profile (Figure 5.1). All stable layers are 1 km deep, but their base heights vary between 1 km, 2 km, and 3 km. The strength of the stable layer is defined following LM2000 and makes use of a constant Brunt-Väisälä frequency within the layer. Using the same values as LM2000ii, the strength of the stable layers are varied between 0.006 s^{-1}, 0.012 s^{-1}, and 0.018 s^{-1}. As the depth of the initial cold bubble is greater than the height of the stable layer, the stable layer is located 8 km away from the cold bubble to allow for steady density current formation prior to layer interaction. The 8 km distance has been determined to be the spin up distance of the density current based on the control simulation, which took 10 minutes of time integration for the gust front to reach that location. This spin up time period is similar to that found by Wolfson (1983) through numerical simulations of downbursts. Wolfson (1983) found that it takes approximately 9 minutes after downdraft touchdown for downbursts to show differences when simulated within a neutral versus a stable boundary layer. Additionally, the imposed stable layer is linearly smoothed over 8 km in the lateral direction to avoid abrupt impacts to the density current. Supplementary simulations were performed with our model and the setup of LM2000ii, the results (not shown) of which successfully replicated those shown in LM2000, thus ensuring consistency between the models and their setups.

5.3. Results and Discussion

5.3.1 Control experiment

As previously stated, the left and right moving portions of the density current are mirror images of one another and the background environment is initially motionless. Therefore the analysis in this section is performed only with regards to the right-moving density current. Also, as this paper builds on LM2000, analysis similar to theirs is presented here in order to facilitate comparisons.

To illustrate the model's capability in generating a realistic density current from a cold bubble, Figure 5.2 shows the density current for the control experiment (i.e. uniform neutral stratification) after 1500 seconds. This time has been chosen because the density current's location is beneath the embedded stable layers in the sensitivity experiments at this time. In Figure 5.2a the potential temperature perturbation shows the overall shape of the density current. This is characterized by an elevated head region behind the gust front with a shallower wake of cold air. The maximum temperature perturbation, which is defined by the difference between the local temperature and the base state temperature (Figure 5.1), is ~ -6 K and agrees well with observations of continental cold pools (Engerer et al. 2008).

As a result of the hydrostatic forces associated with the cold air within the density current, a positive pressure perturbation (Figure 5.2b), which is defined by the difference between the local pressure and the base state pressure, is seen that is characteristic of classic density current models (Simpson 1969,1997; Goff 1976; Xue 2002). Additionally, a positive

pressure perturbation is seen ahead of the density current that is a result of nonhydrostatic forces from increased convergence near the gust front (LM2000). Within the rotational head and above the density current (Figures 5.2b,c), nonhydrostatic effects are contributing to the negative pressure perturbations, and are also in keeping with classical density current models (Simpson 1969; Goff 1976) and LM2000. In association with the large vertical shear at the top of the density current, Kelvin-Helmholtz instability is often observed and also appears in these experiments (Figure 5.2c). This is evident in both the potential temperature field with the overturning of potential temperature surfaces (Figure 5.2a) and the Richardson number field with values less than 0.25 (Figure 5.2c; Miles 1961; Jin et al. 1996). The following section investigates the effects of an embedded stable layer on the described density current.

5.3.2 Sensitivity experiments

As previously described, the sensitivity experiments are designed to investigate the impacts of an embedded 1 km deep, stably stratified layer within a neutrally stratified environment on the characteristics of a density current. In these experiments, the naming convention of which is given in Table 5.1, the strength of the stable layer is varied between N = 0.006 s^{-1}, 0.012 s^{-1}, and 0.018 s^{-1} and the base height of the stable layer between 1 km, 2 km, and 3 km. The density current propagation speed is calculated by following the surface -0.5 K potential temperature perturbation at the gust front. It is apparent from Table 5.2 that with the exception of two experiments, the stable layer acts to increase propagation speed and decrease the density current head height (Figure 5.3). The two anomalous experiments (18N2km and

18N3km) will be further investigated below. Figure 5.3 shows maximum vertical velocity, head height, and maximum pressure perturbation associated with the density current for each experiment in order to illustrate the dynamical trends resulting from the various stable layers. It can be seen that for all of the experiments the maximum vertical velocity (Figure 5.3a), which is located near the gust front (see Figure 5.4), decreases with the addition of a stable layer, with the most significant reductions occurring in association with the stronger and lower stable layers. As described by LM2000, this trend can be explained by the stabilization effect where a stronger and lower stable layer suppresses the vertical displacement of air lifted by the density current due to negative buoyancy. This increased suppression of vertical motion with stronger and lower stable layers also reduces head heights (Figure 5.3b).

As shown in Figure 5.3c, the maximum pressure perturbations also exhibit a distinct trend, whereby the stronger and lower stable layers increase the maximum pressure perturbation – all of which occur at the surface just behind the outflow boundary. To explain these trends, Figures 5.4a-c show the pressure perturbations, temperature perturbations, and vertical velocity values associated with the density current for all three $N = 0.012\ s^{-1}$ stable layer simulations (12N1km, 12N2km, and 12N3km) after 1500 s. The $N = 0.012\ s^{-1}$ simulations have been chosen to illustrate the process under moderate stability. Also depicted in Figure 5.4d are the surface values of pressure and temperature perturbation for the three simulations. As the height of the stable layer is increased, the suppression of the mechanical lifting ahead of the density current is reduced. As previously stated, this trend is due to the stabilization effect where 12N1km (Figure 5.4a) has the stable layer more closely tied to the vertical motion, hence a more dramatic reduction of vertical velocity. However, as the co-location of stratification and larger vertical velocity values exists in 12N1km (Figure 5.4a) as compared with 12N2km (Figure 5.4b) and

12N3km (Figure 5.4c) in which the stable layer is higher up, stronger adiabatic ascent occurs within the stable layer. This stronger mechanically forced ascent gives rise to the larger temperature perturbation within the stable layer (< -3.5 K) in 12N1km (Figure 5.4a) as compared with 12N3km (< -2 K) (Figure 5.4c). Due to hydrostatic forces, the stronger temperature perturbation for the 1 km stable layer experiment (Figure 5.4a) simultaneously increases the surface pressure and results in a stronger pressure gradient (Figure 5.4d) that forces faster density current propagation (Table 5.2). Similar analyses can be used to explain the trend of a stronger stable layer yielding faster propagation (Table 5.2) and a lower head height (Figure 5.3). The maximum difference in propagation speed found between experiments is ~ 1.67 m s^{-1}, which is substantial when applying this difference to realistic time scales of squall lines. For example, using five hours as an approximate time scale for a squall line, this difference gives rise to ~ 30 km variation in distance traveled by the cold pool.

The reversal in propagation speed between this experiment and LM2000ii can be attributed to gravity waves. In LM2000ii, the authors attribute the decrease in propagation speed with increasing stratification to gravity wave trapping. In their case, as the overlying deep stratification increases, the gravity wave propagation speed increases but remains locked to the density current and results in stronger pressure generation out ahead of the density current. This weakens the surface pressure gradient and therefore reduces the propagation speed with increasing stratification. For the experiments presented here, the gravity waves dissipate too quickly to affect the downstream pressure perturbations. The dissipation can be explained by gravity wave ducting theory (Lindzen and Tung 1976). Because of the three-layer regime examined here (i.e. neutral to stable to neutral stratification), the vertically thin stable layer could potentially act as a gravity wave duct. According to Lindzen and Tung (1976), certain criteria

must be met in order for the stable layer to act as a ducting layer. One such criterion states that the duct must be sufficiently thick to accommodate one-quarter of the vertical wavelength of the wave (Lindzen and Tung 1976). A simple calculation can be made to determine if the stable layer is sufficiently thick to duct gravity wave energy generated by the density current using:

$$D = \frac{(c - \overline{u})\pi}{2N} \tag{5}$$

where c is the horizontal phase speed, $\overline{u}$ is the environmental wind relative to the direction of wave propagation, N is the Brunt Väisälä frequency, and D is the depth of the stably stratified layer. For these experiments, $\overline{u}$ is zero, N ranges between 0.006, 0.012, and 0.018 s^{-1}, and c has been numerically calculated for each simulation (Table 5.2). Using these values, the minimum depth for each experiment that can allow gravity wave ducting is shown in Table 5.3. From this, it can be seen that with the exception of the two anomalous experiments previously mentioned (18N2km and 18N3km) all the experiments require a ducting depth (D) greater than 1 km, the depth of the stable layer investigated here. This indicates that for the experiments that exhibit propagation speed increasing with increasing stability, the gravity wave energy cannot be sufficiently ducted and the gravity wave energy dissipates, thus allowing the surface pressure field to be relatively unaffected by propagating gravity waves. Conversely, as soon as the ducting depth decreases to less than 1 km, gravity wave energy can be more efficiently ducted. This results in the ability of the ducted gravity wave to more significantly impact the below pressure field. Once this occurs, the stable layer begins to affect the density current in a manner similar to LM2000ii where the surface pressure gradient is reduced and the density current propagation slows down. This can be seen in Table 5.3 for 18N2km and 18N3km where both ducting depths are less than 1 km and the propagation speed (Table 5.2) remained constant, rather than

increasing. As such, the trends in propagation speed seen with the other seven sensitivity experiments in this study do not apply to 18N2km and 18N3km because the embedded stable layer acted as a ducting layer.

5.4. Conclusions

In summary, a two-dimensional non-hydrostatic model has been used to perform a theoretical study that examines the impact of an embedded stable layer within a neutrally stratified environment on density current structure and propagation. Such regimes are typical of severe weather environments containing high CAPE and some CINH. Testing this regime extends the previous experiments of LM2000. By systematically varying the height and strength of a 1 km deep embedded stable layer it has been shown that with stronger and lower stable layers the density current propagation increases and the density current head height decreases, provided the depth of the stable layer is too thin to prevent gravity wave ducting.

This experiment setup most closely resembles the second regime of LM2000 in which they investigated density current characteristics in a neutrally stratified layer beneath a deep stably stratified layer. In both this experiment and LM2000ii, the density current propagates within the neutrally stratified layer and below the stable layer, thus making this experiment dynamically comparable to LM2000ii. LM2000ii found that deep upper level stratification reduces both the density current head height and propagation speed. While the thin embedded stable layer in our experiments also reduces the density current head height, the propagation speed *increases* with increasing stratification. LM2000 relates the decrease in density current

propagation speed in their experiment to gravity wave trapping that causes a reduction in the horizontal pressure gradient. However in the simulations described here, it is shown that if the upper level stratification is sufficiently shallow such that it cannot act as a ducting layer, and thus the horizontal pressure gradient behind the cold pool boundary can increase causing faster gust front propagation. These findings are important for the understanding of cold pool driven phenomenon, especially for squall line and supercell propagation into environments containing shallow but strong inversions at the top of the boundary layer.

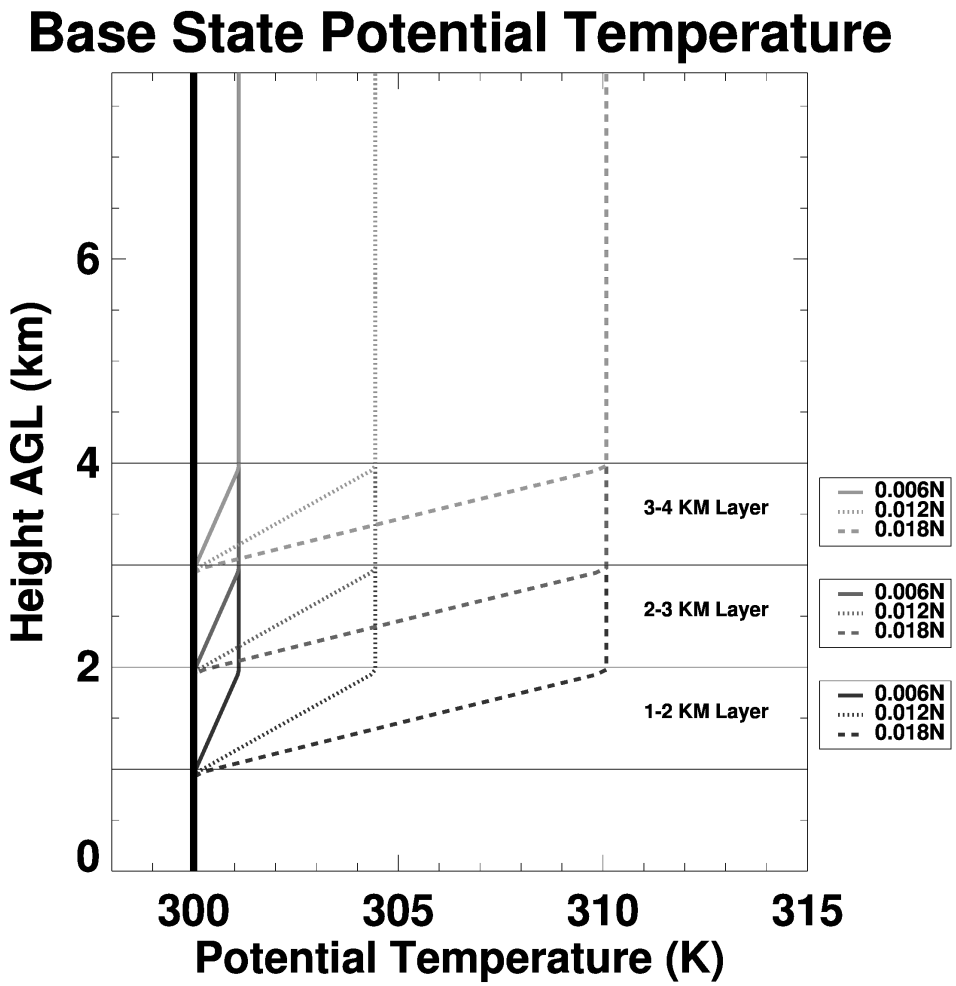

Figure 5.1. Base state potential temperature (θ) profile for each sensitivity simulation. The stable layers vary between 1-2 km (dark grey lines), 2-3 km (grey lines), and 3-4 km (light grey lines) AGL. The strength of the stable layers vary from N = 0.006 s^{-1} (solid lines), N = 0.012 s^{-1} (dotted lines), and N = 0.018 s^{-1} (dashed lines). The control experiment is depicted by the thick black line.

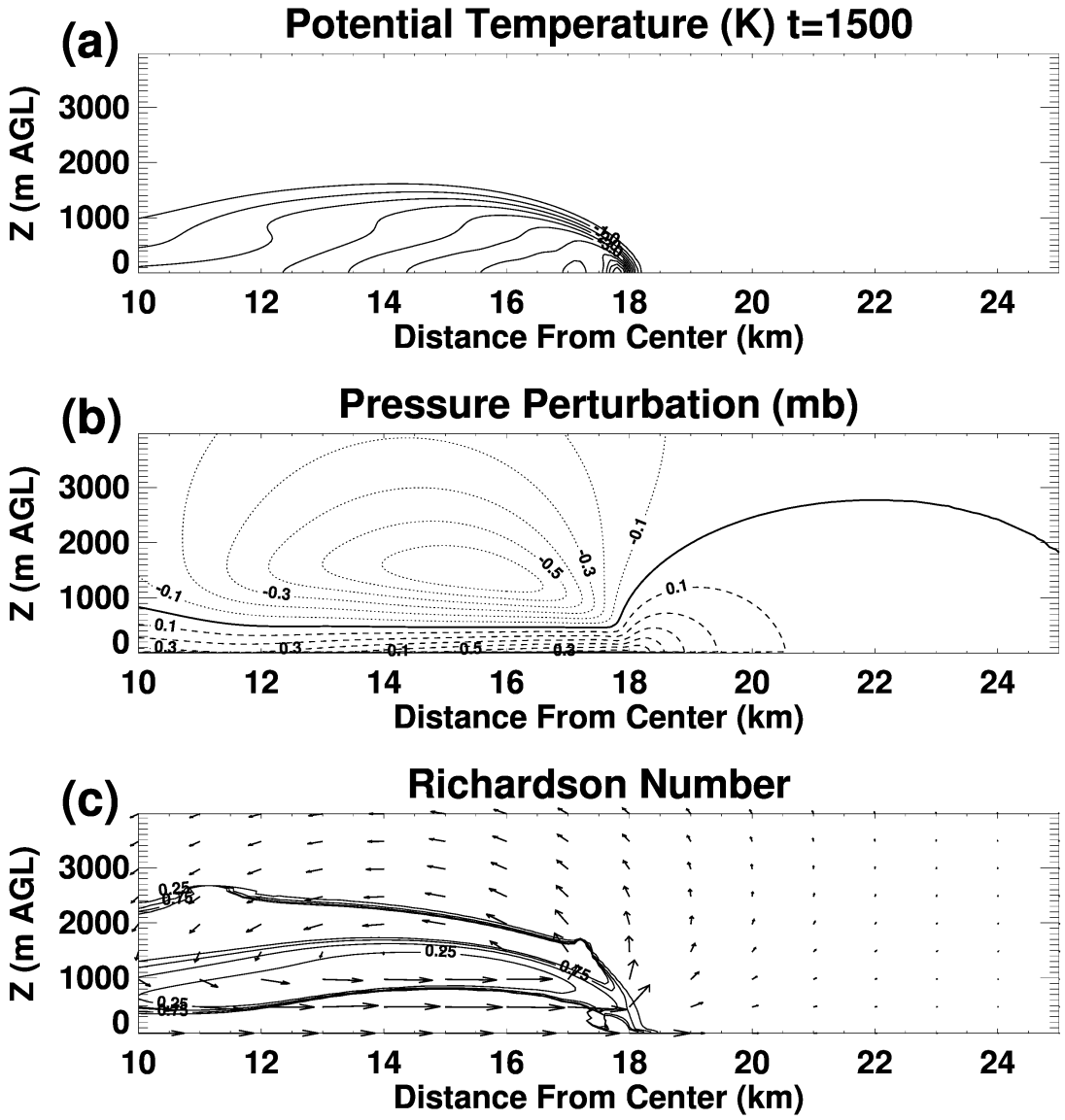

Figure 5.2. Density current generated from cold bubble for the control experiment after 1500 seconds. (a) Potential temperature perturbation contoured in 0.5 K. (b) Pressure perturbation for 0 mb contour (solid), positive perturation (dashed), and negative perturbation (dotted) in 0.1 mb intervals. (c) System relative flow (vectors) and Richardson number in 0.25 intervals.

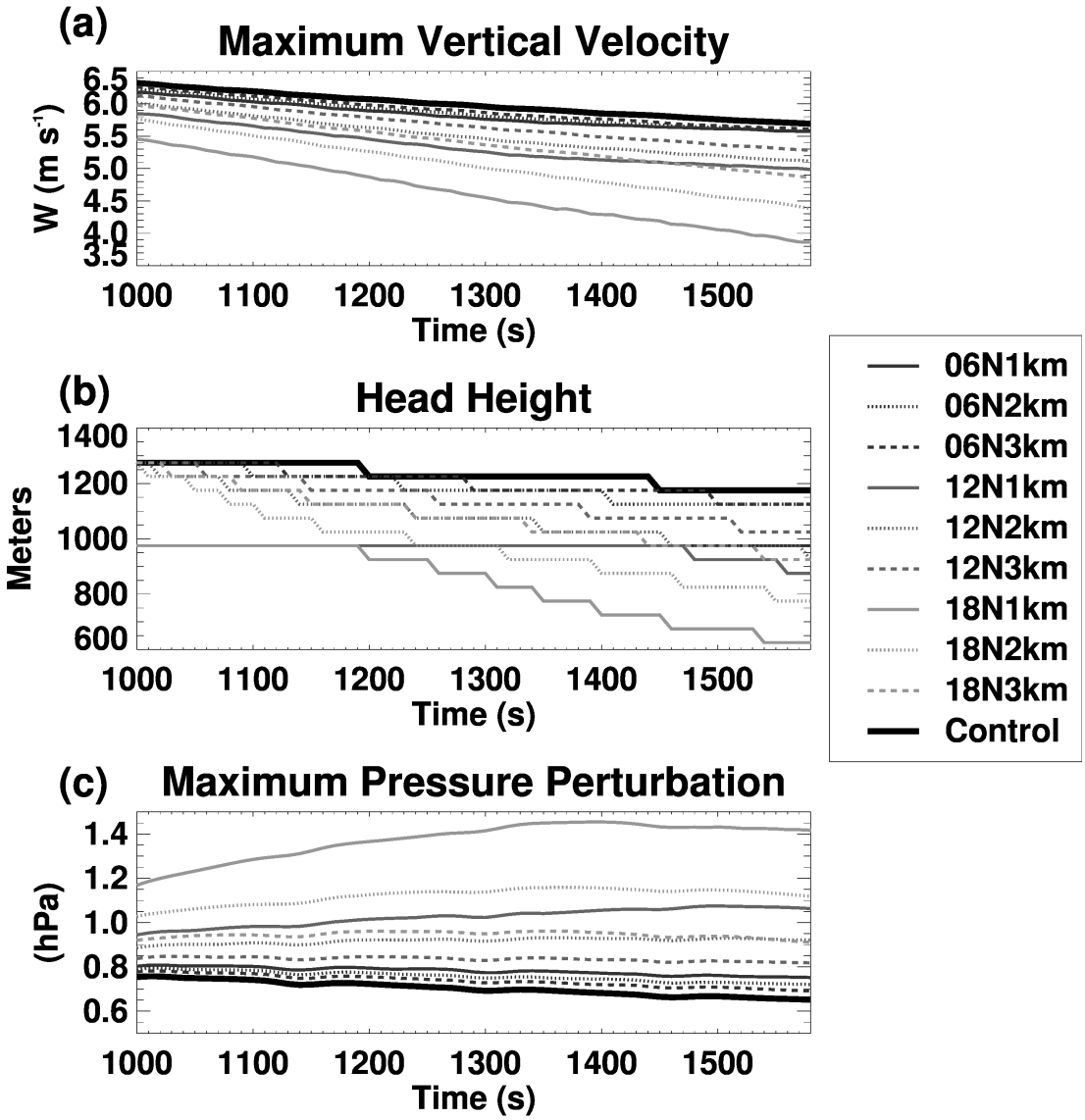

Figure 5.3. Density current trends for the nine sensitivity experiments described in the text and the control experiment. Each experiment consists of a stable layer with depth of 1-2 km (solid lines), 2-3 km (dotted lines), or 3-4 km (dashed lines) AGL and a strength of N = 0.006 s^{-1} (dark grey), 0.012 s^{-1} (grey), and 0.018 s^{-1} (light grey). The control experiment is depicted by the thick black contour. (a) Maximum vertical velocity associated with the gust front; (b) density current head height; and (c) maximum pressure perturbation.

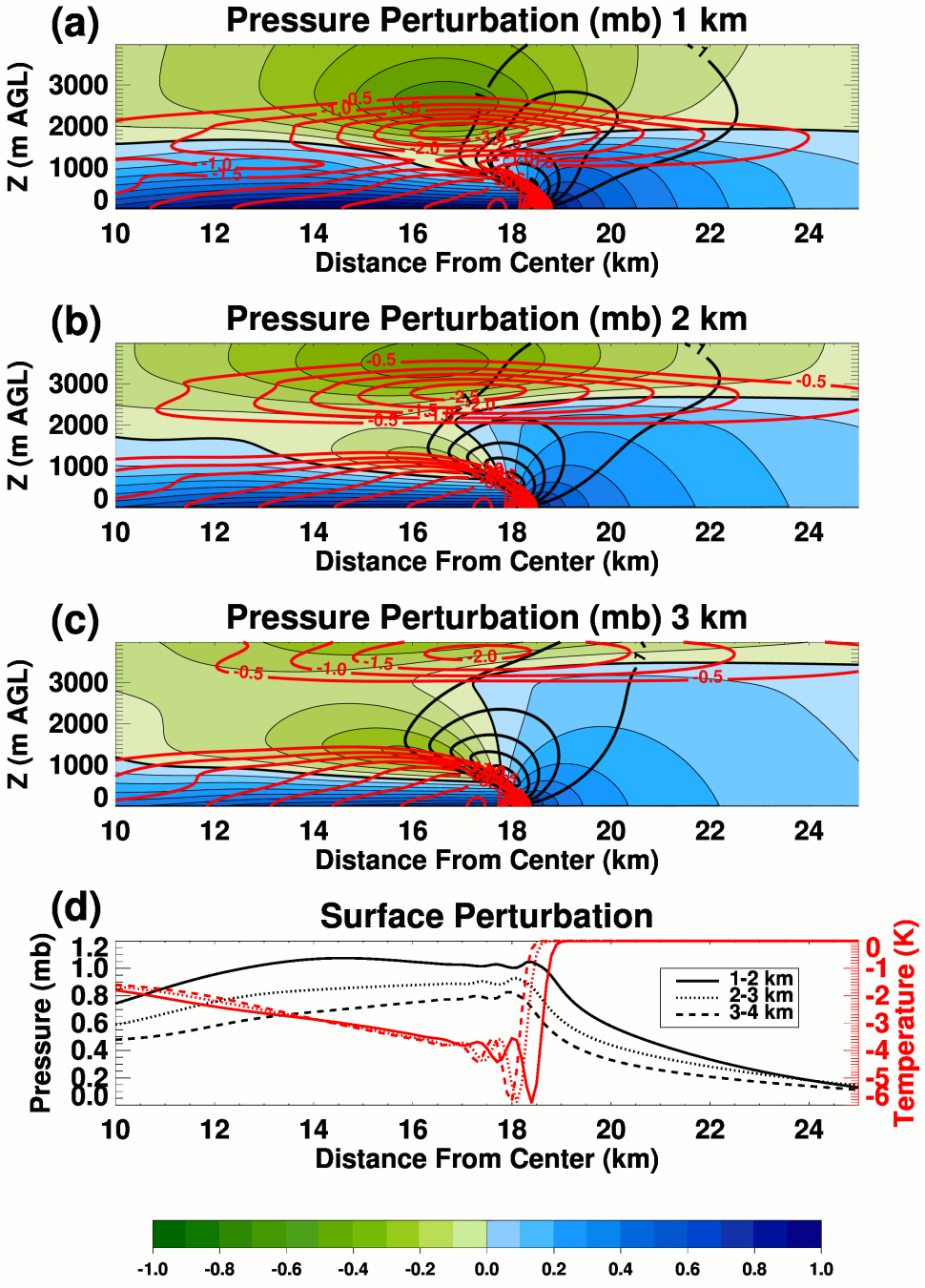

Figure 5.4. Density current after 1500 seconds and associated temperature, pressure, and vertical velocity fields for the three experiements with the N = 0.012 s^{-1} stable layer. Positive pressure perturbation in 0.1 mb (blue shading), negative pressure perturbation in 0.1 mb (green shading), temperature perturbation in 0.5 K intervals (red contours), and vertical velocity in 1 m s^{-1} intervals (black contours) are shown for the (a) 1-2 km AGL, (b) 2-3 km AGL, and (c) 3-4 km AGL experiments. The surface temperature (red contours) and pressure (black lines) perturbations for the three experiments are shown in (d).

Table 5.1. Experiment naming convention.

		Stratification Strength		
		N = 0.006	N = 0.012	N = 0.018
Stable Layer Location	1-2 km AGL	06N1km	12N1km	18N1km
	2-3 km AGL	06N2km	12N2km	18N2km
	3-4 km AGL	06N3km	12N3km	18N3km

Table 5.2. Cold pool propagation speed for each simulation (m s^{-1})

	N = 0.006	N = 0.012	N = 0.018
1-2 km AGL	11.00	11.83	12.33
2-3 km AGL	10.83	11.17	11.17
3-4 km AGL	10.67	11.83	11.83
CONTROL	10.67	10.67	10.67

Table 5.3. Approximate minimum depth (m) for each simulation to allow gravity wave ducting (Lindzen and Tung 1976)

	N = 0.006	N = 0.012	N = 0.018
1-2 km AGL	2880	1548	1076
2-3 km AGL	2836	1462	974
3-4 km AGL	2793	1418	945

CHAPTER 6: OVERALL SUMMARY AND DISCUSSION

Organized mesoscale deep moist convection (DMC) is the global leader in heavy-precipitation, accounting for greater than 90% of total precipitation over land and more than 50% tropics-wide where annual rainfall exceeds 3 mm day^{-1} (Nesbitt et al. 2006). Organized DMC begins with a lifting mechanism (e.g. cold pool or gravity wave) that forces air to rise and condense, thereby releasing latent heat that subsequently leads to positive buoyancy if the ambient thermodynamic environment is conditionally unstable. Ambient wind shear acts to organize the rising column of air through changes in nonhydrostatic pressure perturbations, updraft/downdraft separation, and vorticity (Klemp and Wilhelmson 1978a,b). To a first order approximation, the degree of organization (e.g. supercell, MCS, or squall line) is dictated by the relationship between buoyancy and vertical shear (Klemp and Wilhelmson 1978; Thorpe et al. 1982; Rotunno et al. 1988; Weisman 1992,1993). Following this, modifications to the buoyancy field within DMC can then impact its organization and lifecycle. Numerous past studies have shown that microphysics can be one such impetus (Nicholls 1987; Fovell and Ogura 1988; McCumber et al. 1991; Tao et al. 1995; Liu et al. 1997; van den Heever and Cotton 2004; Adams-Selin et al. 2012a,b; Bryan and Morrison 2012), which is further dictated by the concentration and composition of aerosol particles (Twomey 1974, Albrecht 1989, Petters and Kreidenweis 2007, DeMott et al. 2010). As mineral dust has been found to serve effectively as CCN (Twohy et al. 2009) and IN (DeMott et al. 2003, 2010) and is arguably the most abundant aerosol species in the world (IPCC 2007), its role in the modulation of mesoscale organized DMC is likely to be large. Therefore, four comprehensive studies have been performed that

highlight the various roles mineral dust can play in the mesoscale organization and maintenance of deep moist convection.

Before investigating mineral dust impacts on organized DMC, the manner in which mineral dust is ingested by convective storms was first explored in order to understand the best approach to representing dust in numerical models for future experiments. Three simulations using RAMS as a cloud-resolving model (CRM) were performed that were designed to emulate some of the more common environmental regimes that provide a source of dust for ingestion by supercell storms. The first simulation, EXP-BACKGROUND, investigated a regime in which a supercell develops in an already dusty atmosphere in order to examine dust ingestion by the supercell solely from the environment. Conversely, EXP-STORM explored the regime in which a supercell develops in a dust free environment and the only dust available for ingestion is generated by the supercell itself. Lastly, EXP-BOUNDARY investigated dust ingestion pathways within the regime of a convergence boundary interacting with a supercell whereby both phenomena loft their own dust within an initially clean environment. The three dust regimes simulated in this experiment provide a range of possible dust pathways into convective storms and represent common dust environments observed in reality and utilized in numerical investigations.

The results of the three simulations demonstrate substantial differences in the location and quantity of dust ingested by the supercell. If the only source of dust is within the environmental air (i.e. EXP-BACKGROUND) then relatively large amounts of dust originating from the upper region of the boundary layer ahead of the cold pool is ingested predominantly by the vertical component of the supercell updraft. Conversely, if the atmosphere is originally void of mineral dust and the only dust lofted into the atmosphere is due to the kinematics of the

supercell cold pool (i.e. EXP-STORM), then relatively small concentrations of dust are ingested by the supercell via a very narrow region at the edge of the RFD cold pool. Dusty cold pool air is detrained at the interface between the cold pool and the ambient air and then entrained into the rearward portion of the updraft just ahead of the gust front. When investigating the influence of a convergence boundary on dust ingestion (i.e. EXP-BOUNDARY), it is seen that boundary interactions with supercells can enhance mineral dust ingestion in an initially clean environment by (1) acting as a source of background dust out ahead of the cold pool beneath the updraft, and (2) by enhancing the strength of the updraft and hence vertical advection as a result of the collision.

These experiments show that large differences can arise in the manner in which dust is ingested by supercell storms, as well as in the concentrations of the ingested dust. For example, consider a numerical model investigation of a haboob producing deep convective storm that does not include a dust-lofting scheme. If the goal is to assess storm AIEs by dust, and the storm is occurring within an originally clean environment, then a severe overestimation of ingested dust may result if dust is parameterized as a background aerosol. Takemi (2005), Tulet et al. (2010), and Seigel and van den Heever (2012a) all found that the amount of dust ingested relative to dust lofted is only approximately 10%. Therefore, this first study demonstrates the necessity of an appropriate dust representation in numerical investigations. Furthermore, it illustrates how difficult it is for a storm to ingest dust that has been lofted by its own cold pool.

Given that major changes to organized DMC from aerosol ingestion will likely only occur if the background environment is already dusty, a second study (Seigel and van den Heever 2012b) investigated how background dust could impact a well-organized nocturnal squall line, as nighttime is the peak occurrence time of MCSs (Laing and Fritsch 1997; Anderson and

Arritt 1998; Jirak et al. 2003). For this study, four RAMS CRM simulations of the squall line were performed that systematically altered the inclusions of dust acting microphysically (as CCN, GCCN, and IN) and radiation in order to utilize factor separation. This analysis technique permits the quantification of the contributions to the squall line solely due to microphysically active dust (DUST MICRO), the inclusion of radiation (RADIATION), and the nonlinear interactions between these two forcing mechanisms (SYNERGY).

The analysis showed that the overall role of mineral dust in the squall line simulated here is to weaken the squall line through an enhancement of the warm rain process. This enhancement in warm-rain has also been seen by other studies of warm clouds when both GCCN and CCN are present (Feingold et al., 1999; Cheng et al., 2009). The increase in warm rain near the gust front due to DUST MICRO reduces the liquid water reaching the higher regions of the storm and reduces the contribution to latent heating by riming by up to 30%. This weakens the main updraft of the squall line, which has been shown by past studies to be an important process in the maintenance of squall line updrafts (Adams-Selin et al., 2012; Seigel and van den Heever 2012b). The contribution from DUST MICRO to the mid-level portion of the squall line is also to decrease ice and weaken the mesoscale downdraft. The combination of weaker updrafts and downdrafts from DUST MICRO reduces the convective momentum transport and the overall squall line organization. In association with these processes, the cold pool is weaker, precipitation is reduced, and the total convective mass flux along with net latent heating is suppressed. The substantial weakening of the squall line solely due to mineral dust changing the precipitation process was so large that it overcompensated for the mild squall line invigoration due to SYNERGY. Therefore, mineral dust acts to weaken the simulated squall line.

While Seigel and van den Heever (2012b) was the first to investigate the MCS AIEs solely from mineral dust using a CRM, other studies have investigated the AIE on organized DMC by other aerosol. Similar to Seigel and van den Heever (2012b), Lynn et al. (2005b) also found that increased aerosol for a squall line over Florida produced lower accumulated rainfall. Conversely, Li et al. (2009) simulated a squall line over Texas and found that accumulated precipitation is insensitive to aerosol variations, but increased aerosol led to convective invigoration of updrafts and rain rates. This response was also seen by Wang (2005), however both Li et al. (2009) and Wang (2005) only considered the increase in aerosol as changes to CCN concentrations.

The squall lines in the simulations of Seigel and van den Heever (2012b) showed sensitivity to latent heating near the freezing level, such that with increased latent heating near the freezing level, the squall line was stronger. Numerous other studies have shown a sensitivity of simulated squall lines to the ice phase through feedbacks onto squall line dynamics (Nicholls 1987; Fovell and Ogura 1988; McCumber et al. 1991; Tao et al. 1995; Liu et al. 1997; Adams-Selin et al. 2012a,b; Bryan and Morrison 2012). The commonality in these studies is that the cold pool plays a leading role in squall line intensity. However, this does not explain the sensitivity seen specifically *at* the freezing level. In order to better understand this sensitivity, a second squall line study was performed that shows the importance of a microphysical *recirculation mechanism* and its role in aiding squall line invigoration.

In this study, four simulations of an idealized squall line have been performed using RAMS. First, a control simulation of a squall line using two-moment microphysics for all eight hydrometeor species showed the existence of a recirculation mechanism that begins with hail hydrometeors being ejected upshear from the main convective updraft. As the hail hydrometeors

descend below the freezing level, they encounter the RIJ of the squall line that advects them and melted rainwater back towards the mid-level updraft. The hail and rain become entrained into the upwind side of the updraft *below the freezing level*, where condensation and fusion onto the additional hail and rain hydrometeors promote extra latent heating that in turn enhances buoyancy. The net effect of the recirculation mechanism is to locally enhance latent heating such that it overcompensates the entrainment of negatively buoyant processed air, leading to buoyancy enhancement and subsequent updraft invigoration.

To assess the significance of the recirculation mechanism, three additional sensitivity simulations of a squall line were performed using single-moment microphysics in which the mean diameter of the hail hydrometeor distribution was varied. The results from the sensitivity experiments showed that:

(1) With smaller hail sizes, the vertical structure of the squall lines have a better-defined RIJ, stronger FTR flow, and stronger mesoscale updrafts and downdrafts.
(2) As hail size decreases, precipitation increases along with TWP.
(3) Both convective and total upward mass flux increase with smaller hail sizes.
(4) Net latent heating, especially near the freezing level, increases with smaller hail sizes, leading to greater buoyancy.
(5) The increased buoyancy near the freezing level can be attributed to a positive feedback between the recirculation mechanism and the cold pool, whereby the recirculation mechanism strengthens the mid-level updraft, which promotes increased frozen condensate that enhances the convective downdraft and strengthens the cold pool. The cold pool then enhances the low-level updraft and produces greater supersaturation and subsequent condensation, thereby facilitating the recirculation mechanism.

In reality, a shift in the hail size distribution can occur through increased aerosol concentrations, such as mineral dust. For example, if large concentrations of mineral dust acted as IN within the anvil of the squall line, then ice crystal concentrations would likely be large. Carrio et al. (2007) has shown this response in large-eddy simulations of tropical anvil clouds. Assuming that those ice crystals in our simple example eventually all became hailstones and no significant change in ice mass occurs, then those hail hydrometeors would also be small. While Seigel and van den Heever (2012b) found that increased mineral dust concentrations acted to weaken the squall line, this was due to the enhancement in the warm-rain process from the high dust concentrations ingested at low-levels. If those dust aerosols were present above the freezing level, then changes to the hydrometeor recirculation mechanism may have played a large role in dictating the intensity of the squall line.

In Seigel and van den Heever (2012b,c), the cold pool played an integral role in squall line intensity. When the cold pool was more intense, so was the overlying squall line. This agrees well with numerous past studies of squall line dynamics (Thorpe et al. 1982; Rotunno et al. 1988, 1990; Weisman et al. 1988; Weisman 1992, 1993; Weisman and Rotunno 2004, 2005, 2005; Bryan et al. 2006; Adams-Selin et al. 2012a,b). In addition to this, it has been shown that stability of the ambient environment, which can be altered due to direct aerosol forcing by mineral dust (Tegen et al. 1996; Durant et al. 2009), also plays a large role in the propagation and structure of cold pools (Thorpe et al. 1980; Droegemeier and Wilhelmson 1985; Bischoff-Gauss and Gross 1989; Raymond and Rotunno 1989; Hasse and Smith 1989; Jin et al. 1996; Liu and Moncrieff 1996a, 1996b, 2000). Therefore, another impact that mineral dust can have on organized mesoscale DMC is through the aerosol direct effect that enhances atmospheric stability, which in turn modifies the cold pool.

In order to assess the impact of stable layers on cold pools, a two-dimensional, non-hydrostatic model containing dry physics was developed to most effectively isolate the governing physics and was employed for a fourth study. The study examines the impact of an embedded stable layer within a neutrally stratified environment on density current structure and propagation. Such regimes are typical of environments containing high CAPE and some CINH, and are common for squall lines and other organized mesoscale DMC (Schmidt and Cotton 1989; Smith and Gall 1989; Bryan and Parker 2010). By systematically varying the height and strength of a 1 km deep embedded stable layer it has been shown that with stronger and lower stable layers the density current propagation increases and the density current head height decreases, provided the depth of the stable layer is too thin to prevent gravity wave ducting. If the upper level stratification is sufficiently shallow such that it cannot act as a ducting layer, then the horizontal pressure gradient behind the cold pool boundary can increase causing faster gust front propagation. Given that squall lines and other organized mesoscale DMC are often governed by their cold pool (Rotunno et al. 1988), these results highlight another pathway of mineral dust impacts on deep convection, which is through the ADE altering prefrontal stability.

In summary, four studies have been conducted that highlight a number of ways in which mineral dust can impact the structure and intensity of organized DMC. It has been found that (1) the pathway into DMC is largest when dust is a background aerosol; (2) when dust below the freezing level is ingested by a squall line, an amplification of the warm rain process occurs and causes a weakening of the squall line; (3) a recirculation mechanism centered near the freezing level, which can be affected by mineral dust AIEs, is influential in squall line maintenance; and (4) low-level stable layers that can be created by mineral dust due to the ADE, potentially act to both accelerate and reduce the depth of DMC cold pools. All of these findings have implications

for future modeling studies of aerosol impacts on deep convection. For general circulation models, this highlights the need to represent the mesoscale-microscale interface, as MCSs are the leading contributor to global precipitation and mineral dust has been shown to impact their dynamics, intensity, and precipitation. For regional models that explicitly resolve deep convection, these results highlight the importance of including detailed microphysics and aerosol schemes.

To further our understanding of mineral dust impacts on organized DMC, future work should incorporate observational investigations with the goal of testing the findings of these modeling studies. The use of satellite data and algorithms, such as MODIS, could help isolate cases of dust lofting events near organized mesoscale DMC. These events could then be statistically compared with convective events that were not associated with large dust concentrations. Such investigations would include the use of surface observations, operational model initializations (these contain data assimilated fields), and sensitivity experiments. A region that could be of primary focus is northern Africa, where large MCSs are generated from topographical forcing that sometimes lead to the development of tropical cyclones in the Atlantic (Carlson 1969). It would be beneficial to operational models and forecasters to understand how mineral dust impacts the organization and structure of these westward moving MCSs, as they are often poorly represented in operational models (Zipser et al. 2009).

Additional future work should include a purely observational, statistical study that shows relationships between aerosol concentrations (preferably dust) and the organization/intensity of mesoscale DMC. This could be achieved through statistics on anvil properties such as depth (from CloudSat), size (IR imagery), and microphysical properties (from MODIS). A similar approach to Lensky and Rosenfeld (2003) would be taken by distinguishing continental from

maritime regimes. However, with the recent advances in satellite cloud and microphysics detection (e.g. MODIS, CloudSat, CALIPSO) their study can be significantly improved; and a preliminary study has already been conducted by Storer et al. (2012).

CHAPTER 7: REFERENCES

Adams-Selin, R. D., S. C. van den Heever, and R. H. Johnson, 2012a: Impacts of graupel parameterization schemes on idealized bow echo simulations. *Mon. Wea. Rev.,* accepted.

Adams-Selin, R. D., S. C. van den Heever, and R. H. Johnson, 2012b: Quantitative evaluation of bow echo microphysical sensitivity, *Wea. and Forecasting*, submitted.

Albrecht, B. A., 1989: Aerosols, cloud microphysics, and fractional cloudiness. *Science*, **245**, 1227–1230.

Alpert, P., Tsidulko, M., and U. Stein, 1995: Can sensitivity studies yield absolute comparisons for the effect of several processes? J. Atmos. Sci, 52, 597-601, 1995.

Alpert, P., and Coauthors, 2011: Factor separation in the atmosphere. Cambridge University Press. 352pp.

Anderson, C. J. and R. W. Arritt, 1998: Mesoscale convective complexes and persistent elongated convective systems over the United States during 1992 and 1993. *Mon. Wea. Rev.*, **126,** 578-599.

Andreae, M. O., Rosenfeld, D., Artaxo, P., Costa, A. A., Frank, G. P., Longo, K. M., and Silva-Dias, M. A. F.: Smoking rain clouds over the amazon, Science, 303, 1337, 2004.

Bangert, M., Nenes, A., Vogel, B., Vogel, H., Barahona, D., Karydis, V. A., Kumar, P., Kottmeier, C., and Blahak, U.: Saharan dust event impacts on cloud formation and radiation over western Europe, Atmos. Chem. And Phys., 12, 4045-4063, 2012.

Baron, P. A., and K. Willeke, 2001: Aerosol measurement: Principles, techniques and applications. Second Edition. Wiley-Interscience Inc.

Benjamin, T. B., 1968: Gravity currents and related phenomena. *J. Fluid Mech*., **31**, 209–248.

Berg,W., L'Ecuyer, T., and van den Heever, S. C.: Evidence for the impact of aerosols on the onset and microphysical properties of rainfall from a combination of satellite observations and cloud-resolving model simulations, J. Geophys. Res, 113, D14S23, 2008.

Bischoff-Gauss, I., and G. Gross, 1989: Numerical studies on cold fronts. Part I: gravity flows in a neutral and stratified atmosphere, *Meteorol. Atmos. Phys.,* **40,** 150-158.

Bluestein, H. B., and M. L. Weismann, 2000: The interaction of Numerically simulated supercells initiated along lines, *Mon. Wea. Rev.,* **128,** 3128-3149.

Borys, R. D., Lowenthal, D. H., Wetzel, M. A., Herrera, F., Gonzalez, A., and Harris, J.: Chemical and microphysical properties of marine stratiform cloud in the North Atlantic. J. Geophys. Res., 103, 22 073–22 085, 1998.

Brown, J. M., 1979: Mesoscale unsaturated downdrafts driven by rainfall evaporation: A numerical study. *J. Atmos. Sci.*, **36,** 313-338.

Bryan, G. H., and H. Morrison, 2012: Sensitivity of a simulated squall line to horizontal resolution and parameterization of microphysics. *Mon. Wea. Rev.,* **140,** 202-225, DOI: 10.1175/MWR-D-11-00046.1.

Bryan, G. H., and M. D. Parker, 2010: Observations of a squall line and its near environment using high-frequency rawinsonde launches during VORTEX2. *Mon. Wea. Rev.,* **138,** 4076-4097.

Bryan, G. H., J. C. Knievel, and M. D. Parker, 2006: A multimodel assessment of RKW theory's relevance to squall-line characteristics. *Mon. Wea. Rev*., **134**, 2772–2792.

Bryan, G. H., J. C. Wyngaard, and J. M. Fritsch, 2003: Resolution requirements for the simulation of deep moist convection. *Mon. Wea. Rev*., **131**, 2394–2416.

Bryan, G. H., R. Rotunno, and J. M. Fritsch, 2007: Roll circulations in the convective region of a simulated squall line. *J. Atmos. Sci.,* **64,** 1249–1266.

Carbone, R. E., J. W. Conway, N. A. Crook, and M. W. Moncrieff, 1990: The generation and propagation of a nocturnal squall line. Part I: Observations and implications for mesoscale predictability. *Mon. Wea. Rev.,* **118,** 26-49.

Carlson, T. N., 1969: Synoptic histories of three African disturbances that developed into Atlantic hurricanes. *Mon. Wea. Rev.,* **97,** 256-276.

Carrio, G. G., S. C. van den Heever, and W. R. Cotton, 2007: Impacts of nucleating aerosol on anvil-cirrus clouds: A modeling study, *Atmos. Res.*, **84**, 111-131.

Charba, J., 1974: Application of gravity current model to analysis of squall line gust front. *Mon. Wea. Rev.,* **102,** 140–156.

Chen, S., and Cotton, W. R., 1988: The sensitivity of a simulated extratropical mesoscale convective system to longwave radiation and ice-phase microphysics, *J. Atmos. Sci.,* **45**, 3897-3910.

Chen, W., and D. W. Fryrear, 2002: Sedimentary characteristics of a haboob dust storm, *Atmos. Res*., **61**, 75–85.

Cheng, W. Y. Y., G. G. Carrio, W. R. Cotton, and S. M. Saleeby, 2004: Influence of cloud condensation and giant cloud condensation nuclei on the development of precipitating trade wind cumuli in a large eddy simulation, *J. Geophys. Res*., **114**, D08201.

Chin, H-N S., 1994: The impact of the ice phase and radiation on a midlatitude squall line system, *J. Atmos. Sci*., **51**, 3320-3343.

Churchill, D. D., and R. A. Houze Jr., 1991: Effects of radiation and turbulence on the diabatic heating and water budget of the stratiform region of a tropical cloud cluster, *J. Atmos. Sci*., **48**, 903-922.

Coniglio, M. C., and D. J. Stensrud, 2001: Simulation of a progressive derecho using composite initial conditions. *Mon. Wea. Rev.,* **129,** 1593-1616

Coniglio, M. C., S. F. Corfidi, and J. S. Kain, 2012: Views on applying RKW Theory: An illustration using the 8 May 2009 derecho-producing convective system. *Mon. Wea. Rev.,* **140,** 1023-1043.

Corfidi, S. F., 2003: Cold pools and MCS propagation: Forecasting the motion of downwind-developing MCSs. *Wea. Forecasting*, **18**, 997–1017.

Cotton, W. R., and Coauthors, 2003: RAMS 2001: Current status and future directions. *Meteo and Atmos. Phys., **82,*** 5-29.

Cunningham, P., 2007: Idealized numerical simulations of the interaction between buoyant plumes and density currents, *J. Atmos. Sci.,* **64,** 2105-2115.

Davies, J. M., 2004: Estimations of CIN and LFC associated with tornadic and nontornadic supercells. *Wea. Forecasting,* **19,** 714-726.

Dawson, D. T., M. Xue, J. A. Milbrandt, and M. K. Yau, 2010: Comparison of evaporation and cold pool development between single-moment and multimoment bulk microphysics schemes in idealized simulations of tornadic thunderstorms. *Mon. Wea. Rev.,* **138,** 1152-1171.

De Boer, G., T. Hashino, and G. J. Tripoli, 2010: Ice nucleation through immersion freezing in mixed-phase stratiform clouds: Theory and numerical simulations, *Atmos. Res*., **96**, 315–324.

DeMott, P. J., K. Sassen, M. R. Poellet, D. Baumgardner, D. C. Rogers, S. D. Brooks, A. J. Prenni, and S. M. Kreidenweis, 2003: African dust aerosols as atmospheric ice nuclei, *Geophys. Res. Lett., **30***, 1732, doi:10.1029/2003GL017410.

DeMott, P. J., A. J. Prenni, X. Lui, S. M. Kreidenweis, M. D. Petters, C. H. Twohy, S. Richardson, T. Eidhammer, and D. C. Rogers, 2010: Predicting global atmospheric ice nuclei distributions and their impacts on climate. *PNAS*, 1-6.

Dharssi, I., Kershaw, R., and W. K. Tao, 1997: Sensitivity of a simulated tropical squall line to long-wave radiation*, Q. J. R. Meteorol., Soc*., **123**, 187-206.

Droegemeier, K. K., and R. B. Wilhelmson, 1985: Three-dimensional numerical modeling of convection produced by interacting thunderstorm outflows. Part I: Control simulation and low-level moisture variations, *J. Atmos. Sci.,* **42,** 2381-2403.

Droegemeier, K. K., and R. B. Wilhelmson, 1985: Three-dimensional numerical modeling of convection produced by interacting thunderstorm outflows. Part II: variations in vertical wind shear, *J. Atmos. Sci.,* **42,** 2404-2414.

Dudhia, J., 1989: Numerical study of convection observed during the Winter Monsoon Experiment using a mesoscale two-dimensional model, *J. Afmos. Sci*., **46**,586-601.

Engerer, N. A., and D. J. Stensrud, 2008: Surface characteristics of observed cold pools. *Mon. Wea. Rev.*, **136,** 4839-4849.

Fécan, F., B. Marticorena, and G. Bergametti, 1999: Parametrization of the increase of the Aeolian erosion threshold wind friction velocity due to soil moisture for arid and semi-arid areas, *Ann. Geophys., **17***, 149–157.

Feingold, G., S. Tzivion, and Z. Levin, 1988: Evolution of raindrop spectra. Part I: Solution to the stochastic collection/breakup equation using the method of moments. *J. Atmos. Sci.*, **45**, 3387–3399.

Feingold, G., and A. J. Heymsfield, 1992: Parameterizations of condensational growth of droplets for use in general circulation models. *J. Atmos. Sci*., **49**, 2325–2342.

Feingold, G., R. L. Walko, B. Stevens, and W. R. Cotton, 1998: Simulations of marine stratocumulus using a new microphysical parameterization scheme. *Atmos. Res*., **47–48**, 505–528.

Feingold, G., W. R. Cotton, S. M. Kreidenweis, and J. T. Davis, 1999: The impact of giant cloud condensation nuclei on drizzle formation in stratocumulus: Implications for cloud radiative properties. *J. Atmos. Sci*., **56**, 4100–4117.

Ferek, R. J., and Coauthors, 2000: Drizzle suppression in ship tracks. *J. Atmos. Sci*., **57**, 2707-2728.

Ferrier, B. S., W.-K. Tao, and J. Simpson, 1995: A double-moment multiple-phase four-class bulk ice scheme. Part II: Simulations of convective storms in different large-scale environments and comparisons with other bulk parameterizations. *J. Atmos. Sci*., **52**, 1001-1033.

Field, P. R., et al., 2006: Some ice nucleation characteristics of Asian and Saharan desert dust, *Atmos. Chem. Phys., **6***, 2991–3006.

Fierro, A. O., L. M. Leslie, E. R. Mansell, and J. M. Straka, 2008: Numerical simulations of the microphysics and electrification of the weakly electrified 9 February 1993 TOGA COARE squall line: comparisons with observations. *Mon. Wea. Rev.,* **136,** 364-379.

Fierro, A. O., J. Simpson, M. A. LeMone, J. M. Straka, and B. F. Smull, 2009: On how hot towers fuel the Hadley cell: An observational and modeling study of line-organized convection in the equatorial trough from TOGA COARE. *J. Atmos. Sci.*, **66**, 2730–2746.

Flatau, P. J., G. J. Tripoli, J. Verlinde, and W. R. Cotton, 1989: The CSU-RAMS Cloud Microphysical Module: General Theory and Code Documentation, Dept. of Atmos. Sci., Colorado State Univ., Fort Collins, CO 80523, *Atmos. Sci. Pap*., **451**, 88 pp.

Forster, P., and Coauthors, 2007: Changes in atmospheric constituents and in radiative forcing, in Climate Change 2007: The Physical Science Basis—Contribution of Working Group I to the Fourth Assessment Report of the Intergovernmental Panel on Climate Change, edited by S. Solomon et al., pp. 129–234, Cambridge Univ. Press, Cambridge, U. K.

Fovell, R. G., and Y. Ogura, 1988: Numerical simulation of a midlatitude squall line in two dimensions. *J. Atmos. Sci*., **45**, 3846–3879.

Fovell, R. G., and P.-H. Tan, 1998: The temporal behavior of numerically simulated multicell-type storms. Part II: The convective cell like cycle and cell regeneration. *Mon. Wea. Rev.,* **126,** 551-577.

Fovell, R. G., G. L. Mullendore, and S.-H. Kim, 2006: Discrete propagation in numerically simulated nocturnal squall lines. *J. Atmos. Sci.,* **134,** 3735-3752.

Frame, J., and P. Markowski, 2006: The interaction of simulated squall lines with idealized mountain ridges. *Mon. Wea. Rev.,* **134,** 1919-1941.

Gillette, D. A., and R. Passi, 1988: Modeling dust emission caused by wind erosion, *J. Geoph. Res., **93***, 14,233–14 242.

Gilmore, M. S., J. M. Straka, and E. N. Rasmussen, 2004: Precipitation and evolution sensitivity in simulated deep convective storms: comparison between liquid-only and simple ice and liquid phase microphysics. *Mon. Wea. Rev.,* **132,** 1897-1916.

Ginoux, P., M. Chin, I. Tegen, J. M. Prospero, B. Holden, O. Dubovik, and S.-J. Lin, 2001: Sources and distributions of dust aerosols simulated with the gocart model, *J. Geoph. Res., **106***, 20,255–20,273.

Goff, R. C., 1976: Vertical structure of thunderstorm outflows. *Mon. Wea. Rev.,* **104,** 1429-1440.

Grim, J. A., R. M. Rauber, G. M. McFarquhar, and B. F. Jewett, 2009: Development and forcing of the rear inflow jet in a rapidly developing and decaying squall line during BAMEX. *Mon. Wea. Rev.*, **137,** 1206-1229, DOI: 10.1175/2008MWR2503.1.

Haase, S. P., and R. K. Smith, 1989: The numerical simulation of atmospheric gravity currents. Part II: Environments with stable layers. *Geophys. Astrophys. Fluid Dyn.,* **46,** 35–51.

Haertel, P. T., and R. H. Johnson, 2000: The linear dynamics of squall line mesohighs and wake lows. *J. Atmos. Sci.,* **57,** 93-107.

Hansell, R. A., S. C. Tsay, Q. Ji, N. C. Hsu, M. J. Jeong, S. H. Wang, J. S. Reid, K. N. Liou, and S. C. Ou, 2010: An assessment of the surface longwave direct radiative effect of airborne Saharan dust during the NAMMA field campaign, *J. Atmos. Sci,* ***67,*** 1048-1065.

Harrington, J. Y., 1997: The effects of radiative and microphysical processes on simulated warm and transition season Arctic stratus. Ph.D. dissertation, Atmospheric Science Paper 637, Department of Atmospheric Science, Colorado State University, 289 pp.

Heymsfield, A. J., and G. M. McFarquhar, 2001: Microphysics of INDOEX clean and polluted trade cumulus clouds. *J. Geophys. Res*., **106**, 28 653–28 673.

Hill G. E., 1974: Factors controlling the size and spacing of cumulus clouds as revealed by numerical experiments. *J. Atmos. Sci.*, **31**, 646-673.

Homar, V., R. Romero, D. J. Stensrud, C. Ramis, and S. Alonso, 2003: Numerical diagnosis of a small, quasi-tropical cyclone over the western Mediterranean: dynamical vs. boundary factors, Q. J. R. Meteorol. Soc., 129, 1469-1490.

Houze, R. A., Jr., 1993: Cloud Dynamics. Academic Press, 573 pp.

Houze, R. A., 2004: Mesoscale convective systems. *Rev. of Geophys.,* **42,** 1-43, doi:8755-1209/04/2004RG000150.

Igel, A.L., S. C. van den Heever, C. M. Naud, S. M. Saleeby, and D. J. Posselt, 2012: Sensitivity of warm frontal processes to cloud-nucleating aerosol concentrations. *J. Atmos. Sci.*, Accepted.

IPCC, 2001: "Climate change 2001: the scientific basis", *Intergovernmental Panel on Climate Change*, http://www.grida.no/climate/ipcc_tar/wg1/index.htm.

IPCC, 2007: IPCC AR4 WG1 (2007), Solomon, S.; Qin, D.; Manning, M.; Chen, Z.; Marquis, M.; Averyt, K.B.; Tignor, M.; and Miller, H.L., ed., Climate Change 2007: The Physical Science Basis, Contribution of Working Group I to the Fourth Assessment Report of the Intergovernmental Panel on Climate Change, Cambridge University Press, ISBN 978-0-521-88009-1 (pb: 978-0-521-70596-7).

Isono, K., M. Komabayasi, and A. Ono, 1959: The nature and origin of ice nuclei in the atmosphere. *J. Meteor. Soc. Japan,* ***37***, 211–233.

Jensen, E., D. Starr, and B. Toon, 2004: Mission investigates tropical cirrus clouds. *Eos, Trans. Amer. Geophys. Union*, **84**, 45–50.

Jin, Y., S. E. Koch, Y.-L. Lin, F. M. Ralph, and C. Chen, 1996: Numerical simulations of an observed gravity current and gravity waves in an environment characterized by complex stratification and shear. *J. Atmos. Sci.,* **53,** 3570–3588.

Jirak, I. L., W. R. Cotton, and R. L. McAnelly, 2003: Satellite and radar survey of mesoscale convective system development. *Mon. Wea. Rev.,* **131,** 2428-2449.

Jorgensen, D. P., M. A. LeMone, and S. B. Trier, 1997: Structure and evolution of the 22 February 1993 TOGA COARE squall line: Aircraft observations of precipitation, circulation, and surface energy fluxes. *J. Atmos. Sci.*, **54**, 1961–1985.

Kang, J-Y, S-C Yoon, Y. Shao, and S-W Kim, 2011: Comparison of vertical dust flux by implementing three dust emission schemes in WRF/Chem. *J. Geophys. Res.,* **116,** D09202, doi:10.1029/2010JD014649.

Kaufman, Y. J., and T. Nakajima, 1993: Effect of Amazon smoke on cloud microphysics and albedo—Analysis from satellite imagery. *J. Appl. Meteor*., **32**, 729–744.

Khain, A. P., M. Ovtchinnikov, M. Pinsky, A. Pokrovsky, and H. Krugliak, 2000: Notes on the state-of-the-art numerical modeling of cloud microphysics. *Atmos. Res.,* **55,** 159-224.

Khain, A. P., A. Pokrovsky, and I. Sednev, 1999: Some effects of cloud– aerosol interaction on cloud microphysics structure and pre- cipitation formation: Numerical experiments with a spectral microphysics cloud ensemble model. *Atmos. Res*., **52**, 195–220.

Khain, A. P., D. Rosenfeld, and A. Pokrovsky, 2005: Aerosol impact on the dynamics and microphysics of deep convective clouds. *Quart. J. Roy. Meteor. Soc*., **131**, 2639–2663.

Khain, A. P., N. BenMoshe, and A. Pokrovsky, 2008.: Factors determining the impact of aerosols on surface precipitation from clouds: An attempt at classification. *J. Atmos. Sci*., **65**, 1721–1748.

Klemp, J. B., and R. B. Wilhelmson, 1978a: The simulation of three-dimensional convective storm dynamics, *J. Atmos. Sci.,* **35,** 1070-1096.

Klemp, J. B., and R. B. Wilhelmson, 1978b: Simulations of right- and left-moving storms produced through storm splitting, *J. Atmos. Sci.,* **35,** 1097-1110.

Knippertz, P., C. Deutscher, K. Kandler, T. Muller, O. Schulz, and L. Schultz, 2007: Dust mobilization due to density currents in the Atlas region: Observations from the SAMUM 2006 field campaign*, J. Geophys. Res., **112***, D21109, doi:10.1029/2007JD008774.

Knippertz, P., J. Trentmann, and A. Seifert, 2009: High-resolution simulations of convective pools over the northwestern Sahara, *J. Geophys. Res.,* **114**, D08110, doi:10.1029/2008JD011271.

Lafore, J.-P., and M. W. Moncrieff, 1989: A numerical investigation of the organization and interaction of the convective and stratiform regions of tropical squall lines, *J. Atmos. Sci.,* **46**, 521–544.

Laing, A. G., and J. M. Fritsch, 1997: The global population of mesoscale convective complexes. *Q. J. R. Meteorol. Soc.,* **123,** 389-405.

Lane, P. T., and M. W. Moncrieff, 2010: Characterization of momentum transport associated with organized moist convection and gravity waves, *J. Atmos. Sci*., **67**, 3208-3225.

Lawson, T. J., 1971: Haboob structure at Khartoum, *Weather*, **26**, 105–112.

Lebo, Z., and Seinfeld, J. H., 2011: Theoretical basis for convective invigoration due to increased aerosol concentration. *Atmos. Chem. Phys.,* **11,** 2179-2196

Lee, S. S., L. Donner, and V. T. J. Phillips, 2008a: Examination of aerosol effects on precipitation in deep convective clouds during the 1997 ARM summer experiment. *Q. J. R. Meteorol. Soc.,* **134**, 1201-1220.

Lee, S. S., L. Donner, and V. T. J. Phillips, and Y. Ming, 2008b: The dependence of aerosol effects on clouds and precipitation on cloud-system organization, shear and stability. *J. Geophys. Res.,* **113**, D16 202.

Lee, S. S., L. Donner, and V. T. J. Phillips, 2009: Impacts of aerosol chemical composition on microphysics and precipitation in deep convection, Atmos. Res., 94, 220–237, doi:10.1016/j. atmosres.2009b.05.015, 2009.

Lemon, L. R., and C. A. Doswell, 1979: Severe thunderstorm evolution and mesocyclone structure as related to tornadogenesis. *Mon. Wea. Rev.,* **107,** 1184–1197.

Lensky, I. M., and D. Rosenfeld, 2003: Satellite-based insights into precipitation formation processes in continental and maritime convective clouds at nighttime. *J. Appl. Meteorol.,* **42,** 1227-1233.

Lerach, D. G., B. J. Gaudet, and W. R. Cotton, 2008: Idealized simulations of aerosol influences on tornadogenesis. *Geophys. Res. Lett*., **35**, L23806, doi:10.1029/2008GL035617.

Levin, Z., E. Ganor, and V. Gladstein, 1996: The effects of desert particles coated with sulfate on rain formation in the eastern Mediterranean, *J. Appl. Meteor., **35***, 1511–1523.

Lewis, J. M., M. L. Kaplan, R. Vellore, R. M. Rabin, J. Hallet, and S. A. Cohn, 2010: Dust storm over the Black Rock Desert: larger-scale dynamic signatures, *J. Geophys. Res.,* **116,** D06113, doi:10.1029/2010JD014784

Li, G., Y. Wang, K.-H. Lee, Y. Diao, and R. Zhang, 2009: The impacts of aerosols on development and precipitation of a mesoscale squall line*, J. Geophys. Res*., **114**, D17205, doi:10.1029/2008JD011581.

Lilly D. K.,1962: On the numerical simulation of buoyant convection. *Tellus* **XIV**: 148–172

Lindzen, R. S., and K.-K. Tung, 1976: Banded convective activity and ducted gravity waves. *Mon. Wea. Rev.,* **104,** 1602-1617.

Liu, C.-H., and M. W. Moncrieff, 1996a: A numerical study of the effects of ambient flow and shear on density currents. *Mon. Wea. Rev.,* **124,** 2282–2303.

Liu, C.-H., and M. W. Moncrieff, 1996b: An analytical study of density currents in sheared, stratified fluids including the effects of latent heating. *J. Atmos. Sci.,* **53,** 3303–3312.

Liu, C., M. W. Moncrieff, and E. J. Zipser, 1997: Dynamical influence of microphysics in tropical squall lines: A numerical study. *Mon. Wea. Rev*., **125**, 2193–2210.

Liu, C.-H., and M. W. Moncrieff, 2000: Simulated density currents in idealized stratified environments, *Mon. Wea. Rev.,* **128,** 1420-1437.

Liu, M., D. L. Westphal, A. L. Walker, T. R. Holt, K. A. Richardson, and S. D. Miller, 2007: COAMPS real-time dust storm forecasting during Operation Iraqi Freedom, *Weather and Forecasting, **22**,* 192-206.

Luo, Y., Y. Wang, H. Wang, Y. Zheng, and H. Morrison, 2010: Modeling convective-stratiform precipitation processes on a Mei-Yu front with the Weather Research and Forecasting model: Comparison with observations and sensitivity to cloud microphysics parameterizations. *J. Geophys. Res.,* **115,** D18117.

Lynn, B. H., A. Khain, J. Dudhia, D. Rosenfeld, A. Pokrovsky, and A. Seifert, 2005a: Spectral (bin) microphysics coupled with a mesoscale model (MM5): Part I. Model description and first results, *Mon. Weather Rev*., **133**, 44–58, doi:10.1175/MWR-2840.1.

Lynn, B. H., A. Khain, J. Dudhia, D. Rosenfeld, A. Pokrovsky, and A. Seifert, 2005b: Spectral (bin) microphysics coupled with a mesoscale model (MM5): Part II. Simulation of a CaPE rain event with a squall line, *Mon. Weather Rev*., **133**, 59–71, doi:10.1175/MWR-2841.1.

Markowski, P. M., 2003: Tornadogenesis resulting from the transport circulation by a downdraft: Idealized numerical simulations. *J. Atmos. Sci.,* **60,** 795-823.

Markowski, P. M., J. M. Straka, and E. N. Rasmussen, 2002: Direct surface thermodynamic mea- surements within the rear-flank downdrafts of nontornadic and tornadic supercells. *Mon. Wea. Rev.,* **130,** 1692–1721.

Markowski, P. M., E. Rasmussen, J. Straka, R. Davies-Jones, Y. Richardson, and R. J. Trapp, 2008: Vortex lines within low-level mesocyclones obtained from pseudo-dual-doppler radar observations. *Mon. Wea. Rev.,* **136,** 3513-3535.

Marsham, J. H., D. J. Parker, C. M. Grams, C. M. Taylor, and J. M. Haywood, 2008: Uplift of Saharan dust south of the intertropical discontinuity. *J Geophys. Res.,* **113,** D21102, doi:10.1029/2008JD009844.

Marticorena, B., and G. Bergametti, 1995: Modeling the atmospheric dust cycle: 1. Design of a soil-derived dust emission scheme. *J. Geophys. Res.*, **100,** 16,415-16,430.

Masson, V., J.-L. Champeaux, F. Chauvin, C. Meriguet, and R. Lacaze, 2003: A global database of land surface parameters at 1-km resolution in meteorological and climate models, *J. Climate,* **16**, 1261-1282.

Matrosov, S. Y., 1999: Retrieval of vertical profiles of ice cloud microphysics from radar and IR measurements using tuned regressions between reflectivity and cloud parameters. *J. Geophys. Res.*, **104**, 16 741–16 753

Matsui, T., H. Masunaga, R. A. Pielke Sr., and W.-K. Tao, 2004: Impact of aerosols and atmospheric thermodynamics on cloud properties within the climate system, *Geophys. Res. Lett*., **31**, L06109, doi:10.1029/2003GL019287.

McCumber, M., W.-K. Tao, J. Simpson, R. Penc, and S.-T. Soong, 1991: Comparison of ice-phase microphysical parameterization schemes using numerical simulations of tropical convection. *J. Appl. Meteor*., **30**, 985–1004.

Meng, Z., F. Zhang, P. Markowski, D. Wu, and K. Zhao, 2012: A Modeling Study on the Development of a Bowing Structure and Associated Rear Inflow within a Squall Line over South China. *J. Atmos. Sci*. doi:10.1175/JAS-D-11-0121.1, in press.

Meyers, M. P., R. L. Walko, J. Y. Harrington, and W. R. Cotton, 1997: New RAMS cloud microphysics parameterization. Part II: The two-moment scheme. *Atmos. Res*, **45**, 3–39.

Miles, J. W., 1961: On the stability of heterogeneous shear flows. *J. Fluid. Mech.,* **10,** 496-508.

Miller, S., A. Kuciauskas, M. Liu, Q. Ji, J. Reid, D. Breed, A. Walker, and A. Mandoos, 2008: Haboob dust storms of the southern Arabian Peninsula, *J. Geophys. Res., **113***, D01202, doi:10.1029/2007JD008550.

Mohler, O., P. R. Field, P. Connolly, S. Benz, H. Saathoff, M. Schnaiter, R. Wagner, R. Cotton, M. Kramer, A. Mangold, and A. J. Heymsfield, 2006: Efficiency of the deposition mode ice nucleation on mineral dust particles, *Atmos. Chem. Phys. Discuss., **6**,* 1539-1577.

Moncrieff, M. W., and C.-H. Liu, 1999: Convection initiation by density currents: Role of convergence, shear, and dynamical organization. *Mon. Wea. Rev.,* **127,** 2455–2464.

Morrison, H., 2012: On the robustness of aerosol effects on an idealized supercell storm simulated with a cloud system-resolving model, *Atmos. Chem. Phys. Discuss*., **12**, 10493-10533, doi:10.5194/acpd-12-10493-2012

Morrison, H., and W. W. Grabowski, 2007: Comparison of bulk and bin warm-rain microphysics models using a kinematic framework, *J. Atmos. Sci*., **64**, 2839-2861.

Morrison, H., G. Thompson, and V. Tatarskii, 2009: Impact of cloud microphysics on the development of trailing stratiform precipitation in a simulated squall line: Comparison of one- and two-moment schemes. *Mon. Wea. Rev*., **137**, 991–1007.

Morrison, H., S. Tessendorf, K. Ikeda, and G. Thompson, 2012: Sensitivity of a simulated mid-latitude squall line to parameterization of raindrop breakup. *Mon. Wea. Rev*. doi:10.1175/MWR-D-11-00283.1, in press.

Nesbitt, S. W., R. Cifelli, and S. A. Rutledge, 2006: Storm morphology and rainfall characteristics of TRMM precipitation features, *Mon. Weather Rev*., **134**, 2702–2721, doi:10.1175/MWR3200.1.

Newton, C. W., 1950: Structure and mechanism of the prefrontal squall line. *J. Meteor.,* **7,** 210-222.

Nicholls, M. E., 1987: A comparison of the results of a two-dimensional numerical simulation of a tropical squall line with observations. *Mon. Wea. Rev.,* **115,** 3055-3077.

Noppel, H., U. Blahak, A. Seifert, and K. D. Beheng, 2010: Simulations of a hailstorm and the impact of CCN using an advanced two-moment cloud microphysical scheme, *Atmos. Res*., **96**, 286–301.

Parker, M. D., and R. H. Johnson, 2000: Organizational modes of midlatitude mesoscale convective systems. *Mon. Weather Rev*., **128**, 3413–3436.

Perry, K., T. Cahill, R. Eldred, D. D. Dutcher, and T. E. Gill, 1997: Long-range transport of North African dust to the east- ern United States. *J. Geophys. Res*., **102**, 11 225–11 238.

Petters, M. D., and S. M. Keridenweis, 2007: A single parameter representation of hygroscopic growth and cloud condensation nucleus activity. *Atmos. Chem. Phys.,* **7**, 1961–1971,

Pielke, R. A., W. R. Cotton, R. L. Walko, C. J. Tremback, W. A. Lyons, L. D. Grasso, M. E. Nicholls, M. D. Moran, D. A. Wesley, T. J. Lee, and J. H. Copeland, 1992: A comprehensive meteorological modeling system – RAMS, *Meteor. Atmos. Phys., **49,*** 69-91.

Prospero, J. M., 1996: Saharan dust transport over the North Atlantic Ocean and Mediterranean: An overview. *The Impact of Desert Dust Across the Mediterranean*, S. Guerzoni and R. Chester, Eds., Kluwer Academic, 133–151.

Prospero, J. M., 1999: Long-term measurements of the transport of African mineral dust to the southeastern United States: Implications for regional air quality. *J. Geophys. Res.*, **104,** 15 917–15 927.

Pruppacher, H. R., and J. D. Klett, 1997: Microphysics of Clouds and Precipitation. 2d ed. Kluwer Academic, 954 pp.

Quijano, A. L., I. N. Sokolik, and O. B. Toon, 2000: Radiative heating rates and direct radiative forcing by mineral dust in cloudy atmospheric conditions. *J. Geophys. Res*., **105**, 12 207–12 219.

Ramanathan, V., P. J. Crutzen, J. T. Kiehl, and D. Rosenfeld, 2001: Aerosols, climate, and the hydrologic cycle. *Science,* **294,** 2119-2124.

Raymond, D. J., and R. Rotunno, 1989: Response of a stably stratified flow to cooling. *J. Atmos. Sci.,* **48,** 2830-2837.

Reinfried, F., I. Tegen, B. Heinhold, O. Hellmuth, K. Schepanski, U. Cubash, H. Hubener, and P. Knippertz, 2009: Simulations of convectively driven density currents in the Atlas region using a regional model: Impacts on dust emission and sensitivity to horizontal resolution and convection schemes, *J. Geophys. Res.,* doi:10.1029/2008JD010844.

Roberts, P., and J. Hallett, 1968: A laboratory study of the ice nucleating properties of some mineral particulates, *Quart. J. Roy. Meteor. Soc., **94***, 25–34.

Romero, R., C. Ramis, S. Alonso, C. A. Doswell III, and D. J. Stensrud, 1998: Mesoscale model simulations of three heavy precipitation events in the western Mediterranean region, *Mon. Wea. Rev*., **126**, 1859-1881.

Rosenfeld, D., 2000: Suppression of rain and snow by urban and industrial air pollution, *Science*, **287**, 1793–1796, doi:10.1126/science.287.5459.1793.

Rosenfeld, D., and R. Nirel, 1996: Seeding effectiveness——The interaction of desert dust and the southern margins of rain cloud systems in Israel. *J. Appl. Meteor*., **35**, 1502–1510.

Rosenfeld, D., Y. Rudich, and R. Lahav, 2001: Desert dust suppressing precipitation: A possible desertification feedback loop. *Proc. Natl. Acad. Sci*. USA, **98**, 5975–5980.

Rosenfeld, D., and G. Feingold, 2003: Explanation of the discrepancies among satellite observations of the aerosol indirect effects, *Geophys. Res. Lett*., **30(14),** 1776, doi:10.1029/2003GL017684.

Rosenfeld, D., U. Lohmann, G. Raga, C. O'Dowd, M. Kulmala, S. Fuzzi, A. Reissell, and M. Andreae, 2008: Flood or drought: how do aerosols a_ect precipitation? *Science*, **321** (5894), 1309.

Rotunno, R., J. B. Klemp, and M. L. Weisman, 1988: A theory for strong, long-lived squall lines. *J. Atmos. Sci*., **45**, 463–485.

Rotunno, R., J. B. Klemp, and M. L. Weisman, 1990: Comments on "A numerical investigation of the organization and interaction of the convective and tratiform regions of tropical squall lines." *J. Atmos. Sci,* **47,** 1031-1033.

Rutledge, S. A., and P. V. Hobbs, 1983: The mesoscale and microscale structure and organization of clouds and precipitation in midlatitude cyclones. VIII: A model for the seederfeeder process in warm-frontal rainbands. *J. Atmos. Sci*., **40**, 1185–1206.

Saleeby, S. M., and W. R. Cotton, 2004: A large-droplet mode and prognostic number concentration of cloud droplets in the Colorado State University Regional Atmospheric Modeling System (RAMS). Part I: Module descriptions and supercell test simulations. *J. Appl. Meteor.*, **43**, 182–195.

Saleeby, S.M., and S.C. van den Heever, 2012: Developments in the CSU-RAMS aerosol model: emissions, nucleation, regeneration, deposition and radiation. *J. Appl. Met. Clim*. (in preparation).

Sassen, K., P. J. DeMott, J. M. Prospero, and M. R. Poellet, 2003: Saharan dust storms and indirect aerosol effects on clouds: CRYSTAL-FACE results, *Geophys. Res. Lett., **30***, 1633, doi:10.1029/2003GL017371.

Schmidt, J. M., and W. R. Cotton, 1989: A high plains squall line associated with severe surface winds. *J. Atmos. Sci.,* **46,** 281-302.

Schmidt, J. M., and W. R. Cotton, 1990: Interactions between upper and lower tropospheric gravity waves on squall line structure and maintenance. *J. Atmos. Sci.*, **47**, 1205–1222.

Seigel, R. B., and S. C. van den Heever, 2012a: Dust lofting and ingestion by supercell storms. *J. Atmos. Sci*., **69**, 1453-1473.

Seigel, R. B., S. C. van den Heever, and S. M. Saleeby, 2012b: Assessing the mineral dust indirect effects and radiation impacts on a simulated idealized nocturnal squall line. *Atmos. Chem. and Phys.*, submitted.

Seigel, R. B., and S. C. van den Heever, 2012c: Squall line intensification via hydrometeor recirculation. *J. Atmos. Sci*., submitted.

Seigel, R. B., and S. C. van den Heever, 2012d: Simulated density currents beneath embedded stratified layers. *J. Atmos. Sci.,* **69,** 2192-2200.

Sheffield, A. M., S. C. van den Heever, and S. M. Saleeby, 2012: Growth of cumulus congestus clouds when impacted by aerosols. J. Atmos. Sci., submitted.

Simpson, J., 1969: A comparison between laboratory and atmospheric density currents, *Quart. J. Roy. Meteor. Soc.,* **95,** 758-765.

Simpson, J., 1997: *Gravity Currents in the Environment and the Laboratory*, John Wiley, Halsted, U. K., 244 pp

Slinn, S., and W. G. N. Slinn, 1980: Predictions for particle deposition on natural waters. *Atmos. Env.*, **14**, 1013–1016.

Smagorinsky, J., 1963: General circulation experiments with the primitive equations. I. The basic experiment. *Mon. Wea. Rev*., **91**, 99–164.

Smith, M.A., 2007: Evaluation of mesoscale simulations of dust sources, sinks and transport over the Middle East. M.S. Thesis, Colorado State University, 126 pp. [Available from Department of Atmospheric Science, Colorado State University, Fort Collins, CO 80523.]

Smith, W. P., and R. L. Gall, 1989: Tropical squall lines of the Arizona monsoon. *Mon. Wea. Rev.,* **117,** 1553-1569.

Smull, B. F., and R. A. Houze Jr., 1987: Rear inflow in squall lines with trailing-stratiform precipitation. *Mon. Weather Rev.*, **115**, 2869–2889.

Snook, N., and M. Xue, 2008: Effects of microphysical drop size distribution on tornadogenesis in supercell thunderstorms, *Geophys. Res. Lett.,* **35,** L24803, doi:10.1029/2008GL035866.

Solomos, S., G. Kallos, J. Kushta, M. Astitha, C. Tremback, A. Nenes, and Z. Levin, 2011: An integrated modeling study on the effects of mineral dust and sea salt particles on clouds and precipitation, *Atmos. Chem. Phys*., **11**, 873-892.

Squires, P., and S. Twomey, 1960: The relation between cloud drop spectra and the spectrum of cloud nuclei, in Physics of Precipitation, *Geophys. Monogr. Ser.,* **5**, edited by H. Weickmann, pp. 211–219, AGU, Washington, D. C..

Stein, U., and P. Alpert, 1993: Factor separation in numerical simulations. *J. Atmos. Sci*., **50**, 2107–2115.

Stensrud, D. J., M. C. Coniglio, R. P. Davies-Jones, and J. S. Evans, 2005: Comments on "A theory for strong long-lived squall lines' revisited." *J. Atmos. Sci*., **62**, 2989–2996.

Storer, R. L., S. C. van den Heever, and G. L. Stephens, 2010: Modeling aerosol impacts on convective storms in different environments. *J. Atmos. Sci*., **67**, 3904–3915.

Storer, R. L., and S. C. van den Heever, 2012: Microphysical processes evident in aerosol forcing of tropical deep convection. *J. Atmos. Sci.,* accepted.

Straka, J. M., and J. R. Anderson, 1993: Extension and application of a local, minimum aliasing method to multidimensional problems in limited-area domains. *Mon. Wea. Rev.,* **121,** 2903-2918.

Straka, J. M., R. B. Wilhelmson, L. J. Wicker, J. R. Anderson, and K. K. Droegemeier, 1993: Numerical solutions of a non-linear density current: a benchmark solution and comparisons. *Int. J. Num. Meth. in Fluids,* **17,** 1-22.

Sutton, I. I., 1925: Haboos, Q. J. R. Meteorol. Soc., **51**, 25–50.

Szeto, K. K., and H. Cho, 1994: A numerical investigation of squall lines. Part III: Sensitivity to precipitation processes and the Coriolis force. *J. Atmos. Sci.,* **51,** 1341-1351.

Takemi, T., 2005: Explicit simulations of convective-scale transport of mineral dust in severe convective weather*, J. Meteorol. Soc. Jpn., **83A***, 187 – 203.

Takemi, T., and T. Satomura, 2000: Numerical experiments on the mechanisms for the development and maintenance of long-lived squall lines in dry environments. *J. Atmos. Sci.,* **57,** 1718-1740.

Tao, W., J. Simpson, and S. Soong, 1991: Numerical simulation of a subtropical squall line over the Taiwan Strait. *Mon. Weather Rev*., **119**,2699-2723.

Tao, W., J. Simpson, C. Sui, B. Ferrier, S. Lang, J. Scala, M. Chou, and K. Pickering, 1993: Heating, moisture and water budgets of tropical and mid-latitude squall lines: comparison and sensitivity to long-wave radiation. *J. Atmos. Sci*., **50**,673-890.

Tao, W.-K., J. R. Scala, B. Ferrier, and J. Simpson, 1995: The effect of melting processes on the development of a tropical and a midlatitude squall line. *J. Atmos. Sci.,* **52,** 1934-1948.

Tao, W., J.-P. Chen, Z. Li, C. Wang, and C. Zhang, 2012: Impacts of aerosols on convective clouds and precipitation, *Rev. Geophys*., **50**, RG2001, doi:10.1029/2011RG000369.

Tegen, I., and I. Fung, 1994: Modeling of mineral dust in the atmosphere: Sources, transport and optical thickness, *J. Geoph. Res., **99,*** 22,897–22,914.

Tegen, I., A. A. Lacis, and I. Fung, 1996: The influence on climate forcing of mineral aerosols from disturbed soils. *Nature,* **380,** 419-422.

Thorpe, A. J., M. J. Miller, and M. W. Moncrieff, 1980: Dynamical models of two-dimensional downdraughts, *Quart. J. R. Met. Soc.,* **106,** 463-484.

Thorpe, A. J., M. J. Miller, and M. W. Moncrieff, 1982: Two-dimensional convection in non-constant shear: A model of midlatitude squall lines. *Quart. J. Roy. Meteor. Soc*., **108**, 739–762.

Tompkins, A. M., 2001: Organization of tropical convection in low vertical wind shears: The role of cold pools. *J. Atmos. Sci*., **58**, 1650–1672.

Trier, S. B., W. C. Skamarock, and M. A. LeMone, 1997: Structure and evolution of the 22 February 1993 TOGA COARE squall line: Organization mechanisms inferred from numerical simulations. *J. Atmos. Sci*., **54**, 386–407.

Tulet, P., K. Crahan-Kaku, M. Leriche, B. Aouizerats, and S. Crumeyrolle, 2010: Mixing of dust aerosols into a mesoscale convective system: generation, filtering and possible feedbacks on ice anvils, *Atmos. Res*., **96**, 302-314.

Twohy, C. H., S. M. Kreidenweis, T. Eidhammer, E. V. Browell, A. J. Heymsfield, A. R. Bansemer, B. E. Anderson, G. Chen, S. Ismail, P. J. DeMott, and S C. van den Heever, 2009: Saharan dust particles nucleate droplets in eastern Atlantic clouds, *Geophys. Res. Letters, **36,*** L01807, doi:10.1029/2008GL035846.

Twomey, S., 1977: The influence of pollution on the shortwave albedo of clouds. *J. Atmos. Sci.*, **34**, 1149–1152.

van den Heever, S. C., and W. R. Cotton, 2004: The impact of hail size on simulated supercell storms. *J. Atmos. Sci.*, **61**, 1596–1609.

van den Heever, S. C., G.G. Carrió, W.R. Cotton, P.J. DeMott, and A.J. Prenni, 2006: Impacts of nucleating aerosol on Florida storms. Part I: Mesoscale simulations. *J. Atmos. Sci., **63,*** 1752–1775.

van den Heever, S. C., and W. R. Cotton, 2007: Urban aerosol impacts n downwind convective storms, *J. Appl. Meteorol. Climatol.,* **46**, 828–850, doi:10.1175/JAM2492.1.

van den Heever, S. C., G. L. Stephens, and N. B. Wood, 2011: Aerosol indirect effects on tropical convection characteristics under conditions of radiative-convective equilibrium, *J. Atmos. Sci.,* **68,** 699-718, doi:10.1175/2010JAS3603.1

Van Weverberg, K., A. Vogelmann, H. Morrison, and J. Milbrandt, 2012: Sensitivity of Idealized Squall Line Simulations to the Level of Complexity Used in Two-Moment Bulk Microphysics Schemes. *Mon. Wea. Rev*., **140,** 1883-1907.

Verlinde, J., P. J. Flatau, and W. R. Cotton, 1990: Analytical solutions to the collection growth equation: Comparison with approximate methods and application to cloud microphysics parameterization schemes, *J. Atmos. Sci., **47***, 2871-2880.

Walko, R. L., C. J. Tremback, R. A. Pielke, and W. R. Cotton, 1995: An interactive nesting algorithm for stretched grids and variable nesting ratios, *J. Appl. Meteo., **34***, 994-999.

Wallace, J. M. and P. V. Hobbs, 2006: *Atmospheric Science: An Introductory Survey.* 2d ed. Elsevier, 214-224 pp.

Wang, C., 2005: A model study of the response of tropical deep convection to the increase of CCN concentration: 1. Dynamics and microphysics, *J. Geophys. Res*., **110**, D21211, doi:10.1029/2004JD005720.

Ward, D., and W. R. Cotton, 2011: A method for forecasting cloud condensation nuclei using predictions of aerosol physical and chemical properties from WRF/Chem, *J. Appl. Meteo. Clim.,* **50,** 1601-1615.

Weisman, M. L., 1992: The role of convectively generated rear-inflow jets in the evolution of long-lived mesoconvective systems. *J. Atmos. Sci.,* **49**, 1826–1847.

Weisman, M. L., 1993: The genesis of severe, long-lived bow echoes. *J. Atmos. Sci*., **50**, 645–670.

Weisman, M. L., and J. B. Klemp, 1982: The dependence of numerically simulated convective storms on vertical wind shear and buoyancy. *Mon. Wea. Rev*., **110**, 504–520.

Weisman, M. L., and J. B. Klemp, 1984: The structure and classification of numeri- cally simulated convective storms in directionally varying wind shears. *Mon. Wea. Rev*., **112**, 2479–2498.

Weisman, M. L., Klemp, J. B., and R. Rotunno, 1988: Structure and evolution of numerically simulated squall lines. *J. Atmos. Sci.,* **45,** 1990-2013.

Weisman, M. L., and R. Rotunno, 2004: "A theory for strong long-lived squall lines" revisited. *J. Atmos. Sci.*, **61**, 361–382.

Weisman, M. L., and R. Rotunno, 2005: Reply. *J. Atmos. Sci.,* **62,** 2997-3002.

Wolfson, M. M., 1983: Understanding and predicting microbursts. Ph.D. dissertation, Massachusetts Institute of Technology, 303 pp.

Xiao, Q., and J. Sun, 2007: Multiple-radar data assimilation and short-range quantitative precipitation forecasting of a squall line observed during IHOP_2002. *Mon. Wea. Rev.,* **135,** 3381-3404, DOI: 10.1175/MWR3471.1.

Xu, Q., 1992: Density currents in shear flows—A two-fluid model. *J. Atmos. Sci.,* **49,** 511–524.

Xu, Q., M. Xue, and K. K. Droegemeier, 1996: Numerical simulation of density currents in sheared environments within a vertically confined channel. *J. Atmos. Sci.,* **53,** 770–786.

Xue, M., 2000: Density currents in two-layer shear flows. *Quart. J. Roy. Meteor. Soc.,* **126,** 1301–1320.

Xue, M., 2002: Density currents in shear flows: Effects of rigid lid and cold-pool internal circulation, and application to squall line dynamics. *Quart. J. Roy. Meteor. Soc.,* **128,** 47-73.

Yin, Y., S. Wurzler, Z. Levin, and T. G. Reisin, 2002: Interactions of mineral dust particles and clouds: Effects on precipitation and cloud optical properties, *J. Geophys. Res., **107**(D23:* doi:10.1029/2001JD001522.

Ziegler, C. L., E. R. Mansell, J. M. Straka, D. R. MacGorman, and D. W. Burgess, 2010: The impact of spatial variations of low-level stability on the lifecycle of a simulated supercell storm. *Mon. Wea. Rev.,* **138,** 1738-1766.

Zuberi, B., A. Bertram, C. Cassa, L. Molina, and M. Molina, 2002: Heterogeneous nucleation of ice in (NH4)2SO4-H2O particles with mineral dust immersions, *Geophys. Res. Lett., **29,*** 1504, doi:10.1029/2001GL014289.

Zubler, E. M., D. Folini, U. Lohmann, D. Lüthi, A. Muhlbauer, S. Pousse-Nottelmann, C. Schar, and M. Wild, 2011: Implementation and evaluation of aerosol and cloud microphysics in a regional climate model, *J. Geophys. Res.,* **116,** D0221, doi:10.1029/2010JD014572.